

University of Alberta

Protective/Conductive Coatings for Ferritic Stainless Steel Interconnects
Used in Solid Oxide Fuel Cells

by

Nima Shaigan

A thesis submitted to the Faculty of Graduate Studies and Research
in partial fulfillment of the requirements for the degree of

Doctor of Philosophy

in

Materials Science and Engineering

Chemical and Materials Engineering

©Nima Shaigan

Fall 2009

Edmonton, Alberta

Permission is hereby granted to the University of Alberta Libraries to reproduce single copies of this thesis and to lend or sell such copies for private, scholarly or scientific research purposes only. Where the thesis is converted to, or otherwise made available in digital form, the University of Alberta will advise potential users of the thesis of these terms.

The author reserves all other publication and other rights in association with the copyright in the thesis and, except as herein before provided, neither the thesis nor any substantial portion thereof may be printed or otherwise reproduced in any material form whatsoever without the author's prior written permission.

Examining Committee

Dr. D.G. Ivey, Department of Chemical and Materials Engineering

Dr. W. Chen, Department of Chemical and Materials Engineering

Dr. Qi Liu, Department of Chemical and Materials Engineering

Dr. John Nychka, Department of Chemical and Materials Engineering

Dr. Andre McDonald, Department of Mechanical Engineering

Dr. Anthony Petric, McMaster University

Abstract

Ferritic stainless steels are the most commonly used materials for solid oxide fuel cell interconnect application. Although these alloys may meet the criteria for interconnect application for short periods of service, their application is limited for long-term use (i.e., 40,000 h) due to poor oxidation behaviour that results in a rapid increase in contact resistance. In addition, volatile Cr species migrating from the chromia scale can poison the cathode resulting in a considerable drop in performance of the cell. Coatings and surface modifications have been developed in order to mitigate the abovementioned problems.

In this study, composite electrodeposition of reactive element containing particles in a metal matrix was considered as a solution to the interconnect problems. Nickel and Co were used as the metal matrix and LaCrO_3 particles as the reactive element containing particles. The role of the particles was to improve the oxidation resistance and oxide scale adhesion, while the role of Ni or Co was to provide a matrix for embedding of the particles. Also, oxidation of the Ni or Co matrix led to the formation of conductive oxides. Moreover, as another part of this study, the effect of substrate composition on performance of steel interconnects was investigated.

Numerous experimental techniques were used to study and characterise the oxidation behaviour of the composite coatings, as well as the metal-oxide scale interface properties. Scanning electron microscopy/energy dispersive X-ray

spectroscopy (SEM/EDX), as well as surface analysis techniques including Auger electron spectroscopy (AES), X-ray photoelectron spectroscopy (XPS) and secondary ion mass spectroscopy (SIMS), were used for the purpose of characterization. The substrate used for coating was AISI-SAE 430 stainless steel that is considered as a typical, formerly used interconnect material. Also, for the purpose of the metal-oxide scale interfacial study, ZMG232 stainless steel that is a specially designed interconnect alloy was used.

It is shown that the composite coatings greatly reduce the contact resistance and effectively inhibit Cr outward migration. In addition, it was determined that the presence of impurities in the steel, especially Si, and the absence of reactive elements drastically contribute to interconnect degradation.

Acknowledgments

I am appreciative for the splendid guidance and support received from my supervisors, Dr. D.G. Ivey and Dr. W. Chen. I also am grateful for the individuals who were in control of the laboratory instruments and services at the University of Alberta. In particular, Ms. Tina Barker, Mr. George Braybrook, Dr. Shihong Xu, Dr. Anqiang He and Mr. Shiraz Merali are acknowledged. I am also pleased to thank my colleague, Dr. Weifang Wei, who provided me with useful suggestions and scientific information.

The funding for this research work was provided by National Science and Engineering Research Council of Canada (NSERC) as well as Versa Power Systems (VPS). The author is grateful to these organizations. The author also wishes to thank the Alberta Centre for Surface Engineering and Science (ACSES) for providing SEM, AES, XPS and SIMS analysis.

Above all, I am especially thankful for my wife Sanaz, who has made my life the happiest ever. Without her encouragement and inspiration, I would not be able to accomplish my thesis.

I also appreciate my family members, including my father Aflatoun, my mother Haydeh, my brother Amirhossein and my sister Shima who have invaluable supported me. In particular, I need to thank my father who was the first and only one to encourage me to continue with my studies to higher levels.

Table of contents

1	Introduction and Literature review	1
1.1	Fuel cells	2
1.2	Application of fuel cells	3
1.3	Types of fuel cells	4
1.3.1	Low/medium temperature fuel cells	4
1.3.1.1	Phosphoric acid fuel cells	4
1.3.1.2	Alkaline fuel cells	5
1.3.1.3	Proton exchange membrane fuel cells	5
1.3.1.4	Direct methanol fuel cell	5
1.3.2	High temperature fuel cells	6
1.3.2.1	Molten carbonate fuel cells	6
1.3.2.2	Solid oxide fuel cells	7
1.4	SOFC interconnects	9
1.4.1	Metallic interconnects	11
1.4.1.1	Nickel-based alloys	12
1.4.1.2	Chromium-based alloys	14
1.4.1.3	Stainless steels	15
1.4.2	Coatings for ferritic stainless steel SOFC interconnects	17
1.4.2.1	Reactive element oxide (REO) coatings	18
1.4.2.2	Rare earth perovskite coatings	21
1.4.2.3	Spinel coatings	25
1.4.3	Surface treatments/modifications	35
1.4.4	Alloy developments/modifications	38
1.5	Objectives and motivations	40
1.6	Outline	41

1.7	References.....	45
2	Electrodeposition of Ni/LaCrO ₃ Composite Coatings for Solid Oxide Fuel Cell Stainless Steel Interconnect Applications	56
2.1	Introduction.....	56
2.2	Experimental Methods	57
2.3	Results and Discussion	61
2.3.1	Coating structure and particle distribution.....	61
2.3.2	Effect of particle loading in the bath on coating particle volume fraction.....	62
2.3.3	Effect of bath pH on coating particle volume fraction.....	69
2.3.4	Effect of hydrodynamic parameters on volume fraction of particles embedded in the coatings.....	71
2.4	Conclusions.....	73
2.5	References.....	73
3	Oxidation and Electrical Behavior of Ni/CrO ₃ Coated Stainless Steel Interconnects	75
3.1	Introduction.....	75
3.2	Experimental methods	75
3.3	Results and discussion	78
3.3.1	Scale characterization	78
3.3.2	Effect of LaCrO ₃ particles on oxidation behaviour	85
3.3.3	Area specific resistance (ASR)	93
3.4	Conclusions.....	96
3.5	References.....	97

4	Co/LaCrO ₃ Composite Coatings for AISI 430 Stainless Steel SOFC Interconnects	99
4.1	Introduction.....	99
4.2	Experimental methods	99
4.3	Results and Discussion	101
4.3.1	As-deposited composite Co/LaCrO ₃ coating.....	101
4.3.2	Oxide scale structure and morphology.....	102
4.3.3	SIMS depth profiles	105
4.3.4	Effect of LaCrO ₃ particles.....	107
4.3.5	Area specific resistance.....	110
4.4	Conclusions.....	111
4.5	References.....	112
5	Metal-Oxide Scale Interfacial Imperfections and Performance of Stainless Steel Interconnects Utilized in Solid Oxide Fuel Cells.....	115
5.1	Introduction.....	115
5.2	Experimental Methods.....	116
5.2.1	Specimens and sample preparation	116
5.2.2	Analysis methods	117
5.3	Results and discussion	118
5.3.1	SEM/AES analysis.....	118
5.3.2	XPS analysis	124
5.3.3	SIMS depth profiles	126
5.3.4	Interconnect performance and interfacial defects	131
5.4	Conclusions.....	131

5.5	References.....	132
6	General discussion, conclusions and recommendations	135
6.1	Recommendations for future work	140
7	Appendix- Preliminary proposal and experiments	142
7.1	Introduction.....	142
7.2	Experimental methods	149
7.3	Results and discussion	150
7.4	Conclusions.....	157
7.5	References.....	158

List of tables

Table 1-1 Types of fuel cells, their properties and applications [1, 2]	7
Table 1-2 Nominal composition (wt.%) of nickel-based alloys [33].....	13
Table 1-3 Nominal chemical composition of the steels mentioned in the text*	45
Table 2-1 Composition and operating conditions for Ni/LaCrO ₃ composite electroplating bath.....	60
Table 2-2 Composition and operating conditions of activation/Ni strike plating prior to composite electroplating [9].....	61
Table 3-1 Chemical composition of AISI 430 stainless steel	76
Table 3-2 Compositions (wt.%) determined by EDX point analysis for different regions shown in Figure 3-2	80
Table 3-3 Compositions (wt.%) determined by EDX point analysis for different regions shown in Figure 3-6.	88
Table 4-1 Composition and operating conditions for Co/LaCrO ₃ composite electroplating	100
Table 4-2 Composition and operating conditions of activation/Co strike plating	100
Table 4-3 Chemical composition (wt.%) and phases for the numbered regions in Figure 4-2(b) and (d) as determined by EDX/XRD analysis.	104
Table 4-4 Chemical composition (wt.%) and phases for the numbered regions in Figure 4-6(b) and (d) as determined by EDX/XRD analysis	110
Table 5-1 Nominal compositions of ferritic stainless steels used in this Chapter	118
Table 5-2 XPS analysis results for metal substrate surface of AISI-SAE 430 coupons (oxidized for 500 h in air at 800°C) after scale detachment	125
Table 5-3 XPS analysis results for underside of detached scale formed on AISI-SAE 430 coupons (oxidized for 500 h in air at 800°C).....	126
Table 7-1 Electrical conductivities of some alkali earth doped lanthanum chromites at 1000°C [11]	148

List of figures

Figure 1-1 Schematic representation of a fuel cell [2].	3
Figure 1-2 Representation of the basic operation of a repeating unit of an SOFC [2].	8
Figure 1-3 Schematic representation of (a) tubular and (b) planar SOFCs [3].	9
Figure 1-4 Binary phase diagram for Fe-Cr alloys; α -Fe and δ -Fe are BCC and γ -Fe is FCC [42].	16
Figure 1-5 The effect of different surface treatments on scale adhesion for AISI-SAE 430 samples treated and oxidized at 800C in air for 458 h [154].	37
Figure 2-1 SEM image of LaCrO ₃ powder used for Ni/LaCrO ₃ composite coating	58
Figure 2-2 Particle size distribution for LaCrO ₃ particles.	59
Figure 2-3 SEM images of (a) a plan view sample (secondary electron (SE)) and (b) a cross section sample (backscattered electron (BSE)) of a Ni/LaCrO ₃ composite coating (~30 vol% LaCrO ₃) deposited for 10 minutes. For electrolyte composition and deposition conditions see Table 2-1.	62
Figure 2-4 Volume fraction of particles embedded in the coating (α) as a function of the volume fraction of particles suspended in the plating bath (C) at different current densities.	63
Figure 2-5 $\frac{C(1-\alpha)}{\alpha}$ as a function of volume fraction of particles suspended in the plating bath (C) for particle loadings of 5, 10 and 15 g/L (0.08, 0.17 and 0.25 vol%) at different current densities.	65
Figure 2-6 $\frac{C(1-\alpha)}{\alpha}$ as a function of volume fraction of particles suspended in the plating bath (C) for particle loadings of 20, 30 and 40 g/L (0.34, 0.5 and 0.67 vol%) at different current densities.	66
Figure 2-7 $\log(\tan \varphi)$ as a function of $\log i$ for particle loadings of 5, 10 and 15 g/L (0.08, 0.17 and 0.25 vol%).	69
Figure 2-8 Volume fraction of particles embedded in the coating (α) and cathodic current efficiency for pure Ni deposition as a function of pH at a current density of 40 mA/cm ² and 20 g/L (0.34 vol%) of particle loading in the bath (C).	70

Figure 2-9 Volume fraction of particles embedded in the coatings (α) as a function of bath agitation rate at a current density of 40 mA/cm ² and a 20 g/L (0.34 vol%) particle loading in the bath.....	72
Figure 3-1 Experimental set-up for measuring the electrical contact resistance of oxide scales.....	77
Figure 3-2 SEM images of oxidized Ni/LaCrO ₃ coated AISI 430 stainless steels: (a) and (b) after 170 hours; (c) and (d) after 2040 hours of oxidation in air at 800°C. (a) and (c) are plan view SE images; (b) and (d) are cross sectional BSE images.....	79
Figure 3-3 XRD patterns for Ni/LaCrO ₃ -coated AISI 430 stainless specimens oxidized for 170 and 2040 hours.....	81
Figure 3-4 SIMS depth profiles for oxidized Ni/LaCrO ₃ -coated AISI 430 stainless specimens for (a) 170 and (b) 2040 hours of oxidation.....	83
Figure 3-5 SEM images of oxidized uncoated AISI 430 stainless steels: (a) and (b) after 170 hours; (c) and (d) after 2040 hours of oxidation in air at 800°C. (a) and (c) are cross sectional BSE images; (b) and (d) plan view SE images.....	85
Figure 3-6 SEM images for oxidized Ni-coated AISI 430 stainless steels: (a) and (b) after 170 hours; (c), (d), (e) and (f) after 2040 hours of oxidation in air at 800°C. (e) and (f) show oxide nodules; (a), (c) and (e) are plan view SE images; (b), (d) and (f) are cross sectional BSE images.....	87
Figure 3-7 XRD patterns for Ni-coated AISI 430 stainless specimens oxidized for (a) 170 and (b) 2040 hours.....	89
Figure 3-8 Specific weight gains for oxidized Ni/LaCrO ₃ -coated, Ni-coated and uncoated AISI 430 stainless steels as a function of oxidation time.....	90
Figure 3-9 SE image (a) and corresponding La (b) and S (c) Auger electron maps for Ni/LaCrO ₃ -coated AISI 430 steel, oxidized for 2040 hours in air at 800°C.....	91
Figure 3-10 Measured ASR values for Ni/LaCrO ₃ -coated and uncoated AISI 430 stainless steel at 800°C in air as a function of time.....	93
Figure 3-11 SEM secondary electron (SE) image of a spalled area on an AISI 430 stainless steel oxidized for 170 hours in air at 800°C. The specimen was tilted 40°.....	94
Figure 3-12 Auger electron spectra of (a) cavity and (b) substrate surface shown in Figure 3-11.....	95

Figure 4-1 SEM images of the as-deposited Co/LaCrO ₃ -coating; (a) surface secondary electron (SE) and (b) cross sectional backscattered electron (BSE) image.	102
Figure 4-2 SEM images of oxidized Co/LaCrO ₃ coatings: (a) and (b) after 170 hours; (c) and (d) after 2040 hours of oxidation in air at 800°C. (a) and (c) are surface SE images; (b) and (d) are cross sectional BSE images.....	103
Figure 4-3 XRD patterns for Co/LaCrO ₃ -coated specimens oxidized for 170 and 2040 hours. The peaks labelled spinel are (Fe,Co) ₃ O ₄ spinel.....	105
Figure 4-4 SIMS depth profiles for oxidized Co/LaCrO ₃ -coated specimens for (a) 170 and (b) 2040 hours of oxidation.....	106
Figure 4-5 Specific weight gains for oxidized Co/LaCrO ₃ -coated, Co-coated and uncoated AISI 430 coupons as a function of oxidation time.....	107
Figure 4-6 SEM images of oxidized Co coatings: (a) and (b) after 170 hours; (c) and (d) after 1200 hours of oxidation in air at 800°C. (a) and (c) are surface SE images; (b) and (d) are cross sectional BSE images.....	109
Figure 4-7 ASR values for Co/LaCrO ₃ -coated and uncoated AISI 430 stainless steel at 800°C in air as a function of time.....	111
Figure 5-1 SE images of the spalled areas on AISI-SAE 430 and underside of the detached scale. (a), (b), (c) and (e) show the metallic surface; (d) and (f) represent the related underside of the scale.....	120
Figure 5-2 Auger electron spectra (AES) for the metal surface (a), particles (b), cavity surface (c) the corresponding underside of the scale.....	122
Figure 5-3 SIMS depth profiles for AISI-SAE 430 sample oxidized for 100 h at 800°C in air; (a) for negatively polarized ions and (b) for positively polarized ions.....	129
Figure 5-4 SIMS depth profiles for a ZMG232 sample oxidized for 100 h at 800°C in air; (a) for negatively polarized ions and (b) for positively polarized ions.....	130
Figure 7-1 Al-Cr-Ni isothermal ternary phase diagram at 1150°C [8].	146
Figure 7-2 Schematic representation of an aluminized Ni/LaCrO ₃ coating.	149
Figure 7-3 SEM cross sectional BSE image of a Ni/LaCrO ₃ coating plated in a vertical bath set-up.....	151
Figure 7-4 SEM cross sectional BSE image of a Ni/LaCrO ₃ coating plated in a horizontal bath set-up.....	151

Figure 7-5 SEM cross sectional BSE image of a Ni/LaCrO ₃ coating aluminized via pack-cementation at 1000°C for 5 hours.	152
Figure 7-6 SEM cross sectional BSE image of a Ni/LaCrO ₃ coating aluminized via pack-cementation at 1000°C for 5 hours (absorption of Cl into the LaCrO ₃ particles).....	153
Figure 7-7 SEM plan view images of Ni/LaCrO ₃ coatings heat-treated at 1100°C for various time periods; coalescence of particles and matrix morphology changes are seen for all images.....	154
Figure 7-8 SEM cross section image of a Ni/LaCrO ₃ coating heat-treated at 1000°C for 3 h; the porosity is clearly visible.	154
Figure 7-9 SEM cross section BSE image of the Ni/LaCrO ₃ coating heat-treated at 1000°C for 3 h and oxidized in air at 800°C for 170 h. Breakaway oxidation is clearly observed.	155
Figure 7-10 EDX depth profiles for Ni/LaCrO ₃ coatings annealed at 1000°C for 3 hours.	156
Figure 7-11 Surface Cr concentration versus annealing time for Ni/LaCrO ₃ coatings annealed at 1100°C.	157

1 Introduction and Literature review

In recent years, increased fossil energy use has raised serious environmental concerns particularly in terms of the pollution caused by production of greenhouse gases leading to climate change. Moreover, the natural resources for fossil energy are limited and will be depleted at some point in the future. Clean energies are being considered as a solution to alleviate the issues associated with increased fossil energy use. Solar, wind and water energies are now being used as clean power resources. However, the availability of these energy resources is limited due to natural and geographical restrictions. Hydrogen energy is also an alternative clean energy carrier, which can be used in either stationary or mobile applications. Fuel cells have been invented to exploit the chemical energy of hydrogen (or hydrocarbons) by converting it to electricity with high efficiency and virtually no pollution.

However, commercialization of fuel cells has been facing challenges, most of which are material-related. As a contribution to clean energy, this thesis deals with a material-related hurdle restraining commercialization of the most efficient type of fuel cell, solid oxide fuel cells (SOFCs). In SOFC technology, there is a component named the interconnect which electrically and mechanically connects single cells in order for the SOFC to produce sufficient power. The currently used materials for interconnect applications are ferritic stainless steels which experience conductivity loss due to poor oxidation resistance at elevated service temperatures. Another shortcoming associated with the oxidation of ferritic stainless steel is chromium evaporation, which poisons the electrochemical reactivity of the cell cathode and results in premature cell degradation. Coatings are among a variety of remedies proposed to solve the aforementioned material-related issues.

In this thesis, novel conductive/protective coatings for commercial ferritic steels were developed and examined. Electroplating was used to deposit composite

coatings of LaCrO_3 particles in a Ni or Co matrix. Moreover, during experiments it was found that indigenous impurities in the steel result in poor oxide scale-to-metal adhesion which dramatically increases the interconnect contact resistance. As an original idea, the deleterious effects of impurities and metal-oxide scale interfacial defects were studied for commercially used interconnect alloys.

1.1 Fuel cells

Conversion of the chemical energy of a fuel (hydrogen or hydrocarbon) to electricity is the basic function of fuel cells. Fuel cell is not a new concept and its history dates back to 1839 when William Grove generated electricity from hydrogen and oxygen by reversing the water electrolysis process [1].

Fuel cells, in general, are electrochemical devices consisting of an anode, a cathode and an ion-conducting electrolyte. Such a combination produces electricity when a gaseous fuel and oxygen are continuously fed to the anode and cathode compartments, respectively, provided that the conditions for electrochemical reactions are met [2]. Reduction of oxygen and oxidation of fuel results in a flow of electrons if an external load closes the circuit. If hydrogen is used as the fuel and oxygen as the oxidant, the only byproduct is pure water. The typical structure and operation of a fuel cell is shown schematically in Figure 1-1.

There are some similarities as well as differences between fuel cells and batteries [1]. In a battery, the chemicals required to produce electrical current are pre-stored. Once the pre-stored chemicals are consumed, the battery cannot produce electricity. In rechargeable batteries, the chemicals required for production of electrical current are restored by application of an external current [2]. In fuel cells, the substances required for production of electrical current are provided by an external source.

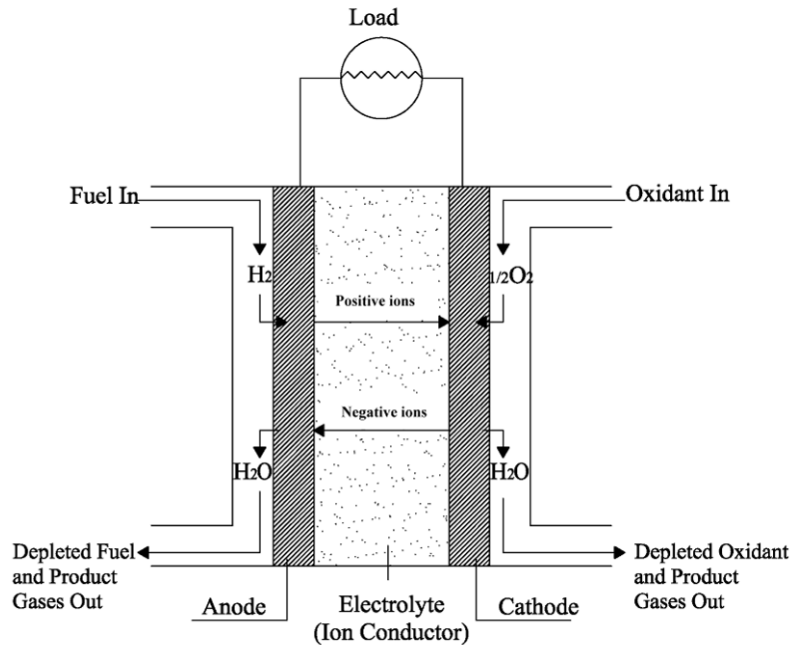


Figure 1-1 Schematic representation of a fuel cell [2].

1.2 Application of fuel cells

Whether fuel cells will achieve extensive commercial application is still controversial. However, fuel cells can be used in transportation, stationary power generation and portable applications [1].

Replacing the internal combustion engines with the purpose of increasing the fuel efficiency and reducing the CO₂ emissions is believed to be the most important reason for application of fuel cells in transportation industry [1]. Fuel cells are theoretically more efficient than internal combustion engines[1].

The main potential application of fuel cells is believed to be in the stationary power generation installations [1]. Fuel cells as stationary power generation systems, especially in the form of combined heat and power generation (CHP), reduce the total CO₂ emissions otherwise produced by conventional power generation systems [1].

Fuel cells with a power capacity of 1 kW are considered as portable power, which can be used as an ancillary supply for vehicles [1]. Also, fuel cells are gaining application in small electronic devices such as cell phones and portable computers as a portable power source for recharging the batteries.

1.3 Types of fuel cells

Fuel cells are classified into low/medium and high temperature types. Phosphoric acid fuel cells (PAFCs), alkaline fuel cells (AFCs), proton exchange membrane fuel cells (PEMFCs), also known as solid polymer fuel cells (SPFCs) or polymer electrolyte fuel cells (PEFCs), and direct methanol fuel cells (DMFC) are regarded as low/medium temperature cells [1]. High temperature fuel cells include molten carbonate fuel cells (MCFCs) as well as solid oxide fuel cells (SOFCs). High temperature fuel cells, particularly SOFCs, are attractive due to their high efficiency and possibility of the direct use of natural gas, thereby avoiding costly hydrogen generation installations [1]. The structure, properties, operating conditions and applications of various types of fuel cells are briefly described in this Chapter and summarized in Table 1-1. Since this thesis concentrates only on SOFCs, this type of fuel cell will be described in more detail.

1.3.1 Low/medium temperature fuel cells

The term low temperature fuel cell is usually referred to a group of fuel cells operating normally below 250°C [2]. This class of fuel cells includes PAFCs, AFCs and PEMFCs, each of which will be briefly introduced here.

1.3.1.1 Phosphoric acid fuel cells

In this type of fuel cell, the electrolyte is concentrated phosphoric acid (100%) [2]. The operating temperature for a typical PAFC ranges from 150 to 220°C [2]. The advantage of the use of phosphoric acid over other conventional acids is its high stability at elevated temperatures [2]. In addition, concentrated phosphoric

acid reduces the pressure of water vapour so that presence of water in the cell is not a problem. A container made of silicon carbide is used to hold the acid and the anode and cathode are made of Pt electrocatalysts [2].

1.3.1.2 Alkaline fuel cells

The electrolyte in AFCs is concentrated potassium hydroxide. The cell operates at relatively high temperatures, around 250°C [2]. Lower concentrations of potassium hydroxide (35-50 wt.%) are used in lower temperature cells which operate at temperatures below 120°C [2]. Generally, asbestos matrixes are used to retain the concentrated alkaline electrolyte [2]. The electrocatalysts used in AFCs can be selected from Ni, Ag, metal oxides, spinels and noble metals [2]. The fuel supply is usually pure hydrogen since CO and CO₂ react with KOH and produce solid carbonates which poison the cell activity [2].

1.3.1.3 Proton exchange membrane fuel cells

A proton conducting, ion exchange polymer membrane is used as the electrolyte in PEMFCs [1-3]. Fluorinated sulphonic acid polymer is an example of the electrolyte material. When the fuel and air are supplied to a PEMFC, electrical power of up to 1 V and power densities of up to about 1 Wcm⁻² can be achieved [2]. The membrane conducts the protons only in the presence of liquid water and the operating temperature must not exceed 100°C even under high operating pressures [2]. Due to low operating temperature, an efficient electrocatalyst system is needed to obtain acceptable performance. Gas-porous, thin electrode layers (several microns to several tens of microns thick) are located on either side of the membrane.

1.3.1.4 Direct methanol fuel cell

Application of liquid fuels in fuel cells is attracting attention mostly for transportation and portable applications [1]. A direct methanol fuel cell (DMFC)

uses methanol, water vapour and air [1]. For this type of fuel cell, one technological challenge is to find a better anode catalyst to reduce the anode overpotentials [1]. In addition, overcoming cathode poisoning and fuel losses caused by migration of methanol from the anode to cathode is the major focus of the current DMFC research and technology [1]. An electrical power density of up to 0.2 Wcm^{-2} can be generated by current prototype DMFCs under ideal conditions [1]. However, this power density is close to what can be achieved with other types of fuel cells [1].

1.3.2 High temperature fuel cells

High temperature fuel cells include MCFCs and SOFCs. The main application of MCFCs and SOFCs is in stationary power generation. In this class of fuel cells, the electrolytes are anion-conducting materials, which are able to transport O^{2-} and CO_3^{-2} as charge carriers [1-3].

The main advantage of this class of fuel cells over low temperature fuel cells is their high efficiency. In addition, in this class of fuel cells, the internal processing of fuels such as natural gas is possible due to the high operating temperatures. Costly and complex hydrogen generation installations, therefore, are not required for this class of fuel cell.

1.3.2.1 Molten carbonate fuel cells

In MCFCs, the electrolyte consists of a combination of alkali carbonates [2]. A ceramic matrix of LiAlO_2 is used to retain the electrolyte [2]. Molten carbonates provide a highly conductive media for ion transpiration at the operating temperature range of 600 to 700°C [2]. Since MCFCs operate at elevated temperatures, Ni can be used as the anode and NiO as the cathode material and precious metals are not necessary [2]. The main disadvantage of MCFC, however, is its short lifetime. The corrosion is the major problem resulting in degradation of

the cell. Dissolution of metal oxides as well as carburization of metallic current collectors are the common corrosion issues in this type of fuel cell [3].

Table 1-1 Types of fuel cells, their properties and applications [1, 2]

Fuel Cell Type	Electrolyte	Charge Carrier	Operating Temperature	Fuel	Electric Efficiency (System)	Power Range/Application
Alkaline AFC	KOH	OH ⁻	60-120°C	Pure H ₂	33-55%	<5kW, niche markets (military, space)
PEMFC	Solid polymer (such as Nafion)	H ⁺	50-100°C	Pure H ₂ (tolerates CO ₂)	35-45%	Automotive, CHP (5–250 kW), portable
PAFC	Phosphoric acid	H ⁺	~220°C	Pure H ₂ (tolerates CO ₂ , approx. 1% CO)	40%	CHP (200 kW)
MCFC	Lithium and potassium carbonate	CO ₃ ²⁻	~650°C	H ₂ , CO, CH ₄ , other hydrocarbons (tolerates CO ₂)	>50%	200 kW–MW range, CHP and standalone
SOFC	Solid oxide electrolyte (yttria, zirconia)	O ²⁻	~1000°C	H ₂ , CO, CH ₄ , other hydrocarbons (tolerates CO ₂)	>50%	2 kW–MW range, CHP and standalone

1.3.2.2 Solid oxide fuel cells

In SOFCs, as the name implies, a solid, ion-conducting ceramic material is used as the electrolyte, in contrast to other types of fuel cells which function with liquid electrolytes. An individual SOFC consists of a solid electrolyte (e.g., yttria stabilized zirconia (YSZ)), a permeable cathode (e.g., lanthanum strontium manganite (LSM)) and a porous anode (e.g., Ni/ZrO₂ cermet) [2, 4]. Oxidation

and reduction reactions take place at the triple-phase boundaries where air or fuel, the electrode and the electrolyte meet [2]. Oxygen or air is fed to the cathode where the oxygen is reduced to oxygen anions. Oxygen anions then migrate through the solid electrolyte and reach the anode where hydrogen or a hydrocarbon oxidizes. Depending on the fuel used, water and carbon dioxide as well as a flow of electrons from the anode to the cathode are produced when an external load closes the circuit. The basic operation of an SOFC unit is schematically represented in Figure 1-2.

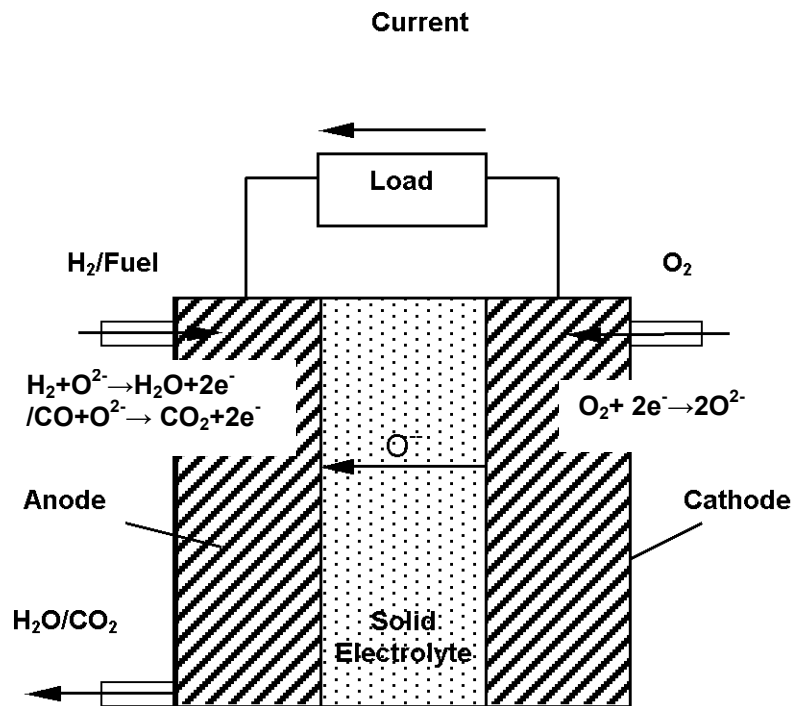


Figure 1-2 Representation of the basic operation of a repeating unit of an SOFC [2].

Two designs, including tubular and planar, have been used for construction of SOFCs. Tubular SOFCs operate at relatively high temperatures (e.g., 900-1000°C [3]) which require advanced, costly materials to maintain the chemical and mechanical stability of the cell. In the planar configuration, however, ultrathin

layers of electrolyte and cathode can be fabricated on a thicker anode, which provides physical stability for the cell. This structure is known as an anode-supported SOFC [5]. In anode-supported SOFCs, high operating temperatures are not necessary to activate the cell components for the ion transport and redox reactions to occur. The operating temperatures for anode-supported SOFCs can be reduced to approximately 600-800°C without significant loss of efficiency [6-10]. Lowering the operating temperatures in planar SOFCs allows the application of more inexpensive, less elaborate materials in comparison with their tubular counterparts. Most recent research endeavours, therefore, have focused on commercialization of planar SOFCs rather than their tubular counterparts. Tubular and planar configurations are schematically represented in Figure 1-3.

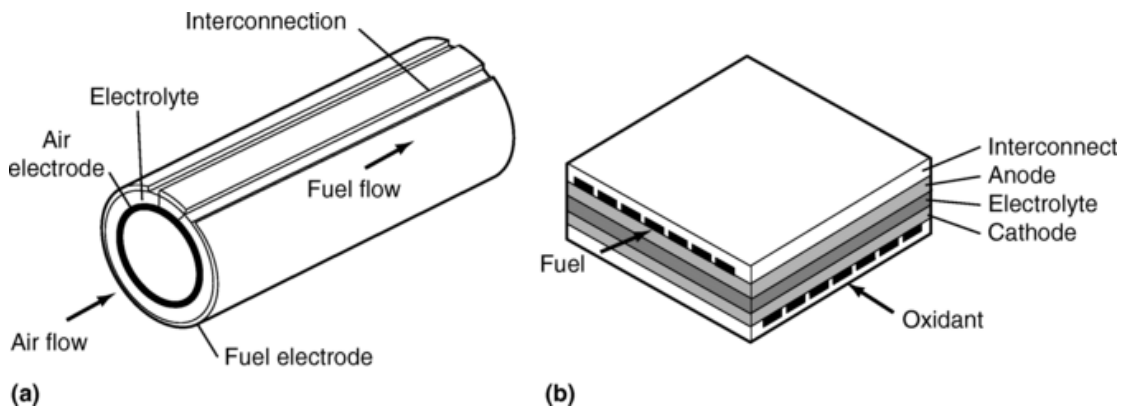


Figure 1-3 Schematic representation of (a) tubular and (b) planar SOFCs [3].

1.4 SOFC interconnects

In planar SOFCs, the maximum obtainable voltage produced by each individual cell does not practically exceed 1 volt, which is not adequate for commercial applications [11]. Consequently, single cells are electrically and mechanically interconnected in series to form stacks which will be capable of producing the required voltage, current and power [2, 11]. Figure 1-3(b) schematically represents a repeating unit of a fuel cell stack. In a stack, individual cells are interconnected by a component termed the interconnect (or bipolar plate). The

interconnect also performs as a feeder and distributor for reacting gases and an exhaust for the depleted reactants and byproducts, water and/or carbon dioxide. Since the interconnect must operate in both oxidizing and reducing atmospheres at high temperatures, the material selected for this purpose must meet some stringent criteria to guarantee the expected cell stability and performance for the target service time of 40,000 hours [12]. The interconnect material must be impermeable to gases and ions, exhibit sufficient chemical and physical stability and provide adequate electronic and thermal conductivity. Furthermore, inasmuch as the interconnect is in direct contact with other ceramic cell components, the candidate material must also be compatible with these parts in terms of exhibiting good thermal coefficient of expansion (CTE) match [7, 10, 13-15]. There are two types of materials used as interconnects, ceramics and metals.

Electronically conductive ceramics with a perovskite type structure, including oxides selected from the (La, Sr, Ca)(Cr, Mn)O₃ or (Y, Ca)(Cr, Mn)O₃ groups, were the first materials of interest to be used as SOFC interconnects [7, 14, 16-20]. In theory, ceramics reasonably meet interconnect criteria including good electronic conduction, low ionic conduction, chemical stability and CTE match with the electrode materials, if they can be fabricated in adequately dense plates [6, 14, 21, 22].

Nonetheless, conductive ceramics have been abandoned for SOFCs due to numerous drawbacks associated with their fabrication and performance. Ceramics are brittle and difficult and costly to fabricate into compact, pore-free forms and complex shapes [8, 15, 21, 23]. In addition, the conductivity of doped lanthanum chromites is greatly dependent on the oxygen partial pressure and temperature, which limits their applicability at lower temperatures (temperature must be above ~900°C for acceptable conductivity) [7].

1.4.1 Metallic interconnects

Metallic interconnects have been recently considered as potential substitutes for ceramic interconnects. In contrast with ceramics, metals are inexpensive and entirely gas tight. Metals are ductile and can be easily formed to complex configurations. They also exhibit excellent thermal and electronic conductivity [8, 15, 21, 23]. The application of metallic interconnects, however, was impracticable before the advent of anode-supported SOFCs which allow operation at lower temperatures (e.g., 600-800°C [7]). Metals are not the appropriate choice for service at temperatures above 900°C as they corrode severely in oxidizing and reducing atmospheres at such high temperatures. Being high-temperature oxidation resistant is then the first criterion for an interconnect alloy to meet. Equally importantly, the alloy selected for interconnect use also must maintain a stable and low area specific resistance (ASR)* (high conductivity) under the service conditions. It is commonly accepted that the upper limit for ASR is 0.1 Ωcm^2 for 40,000 hours of service time [6]. Furthermore, the other critical criterion in selection of an alloy for interconnect application is its CTE match with the ceramic components of the cell in order to prevent any failure during the heating/cooling cycles of the stack.

In order for an alloy to be high-temperature corrosion resistant, the formation of an initial protective oxide scale, which further inhibits oxidation of the substrate, is necessary unless the metal or alloy is noble (e.g., Au and Pt). Alumina, chromia and possibly silica formers are the only known, commercial high temperature/oxidation resistant alloys. However, since the ASR strictly depends on the resistivity of the thermally grown oxide scales, the choice of the interconnect alloy is limited by the type of the protective oxide scale growing on the alloy. The application of alumina (and silica) forming alloys as interconnects is, therefore, not practical due to the electronically insulating nature of these protecting oxides [6]. Chromia, however, shows fair conductivity at high temperatures (the conductivity is 0.01 S cm^{-1} at 800°C for pure chromia [7]).

* ASR is defined as the product of resistance (of the scale) and surface area.

Furthermore, chromia is a p-type semiconductor which can be doped with cations of different size and valences (e.g., cations of Ni, Co, Mg, Y, etc.) for increased conductivity [24, 25]. However, there is an issue associated with chromia scales at elevated temperatures and in the presence of water vapour, that are the normal conditions under which a typical SOFC works. Under such conditions, chromia reacts with water or oxygen molecules and forms volatile chromium oxyhydroxide ($\text{Cr}_2(\text{OH})_2$) and/or Cr(IV) oxide (CrO_3). Volatile Cr species will then migrate through the cathode, dissociate and deposit on the cathode/electrolyte interface as chromia and other unwanted compounds like SrCrO_4 , in the presence of an LSM cathode. The chromium deposition poisons the cathode's electrochemical activity and drastically increases the cell resistance. This is known as cathode Cr poisoning and has been the subject of many research studies [26-32]. Despite the Cr poisoning issue that must be overcome, chromia-forming alloys are seemingly the only choices for interconnect application as alumina is insulating.

In addition to being a chromia former, the candidate interconnect alloy must meet the CTE match criterion. Among chromia formers, Ni -based superalloys and Cr-based alloys as well as various grades of stainless steels have been studied and implemented. Yang et al. [15] have thoroughly reviewed the properties of various heat-resistant alloys and their applicability as SOFCs interconnects.

1.4.1.1 Nickel-based alloys

Nickel-based alloys contain Cr, Fe, Co, Mn and Al. Other elements (e.g., Mo, Nb, Ti and Si) may be added to improve high-temperature strength and oxidation resistance. The well-known examples of Ni-based superalloys, which have been used and studied for interconnect purposes, are Inconel, Hastelloy and the Haynes series [33]. The compositions for some of these alloys are presented in Table 2-1.

Table 1-2 Nominal composition (wt.%) of nickel-based alloys [33]

Alloy	Ni	Cr	Fe	Co	Mn	Mo	Nb	Ti	Si	Al
Inocel 600	Bal	14- 16	6- 9	-	0.4-1	10	-	0.2- 0.4	0.2- 0.5	0.2
Haynes R41 (Rene 14)	Bal	19	5	11	0.1	-	-	3.1	0.5	1.5
Haynes 230	Bal	22- 26	3	5	0.5- 0.7	1-2	-	-	-	0.3
Hastelloy X	Bal	24	19	1.5	1.0	5.3	-	-	-	-
Inocel 625	Bal	25	5.4	5.4	0.6	5.7	-	-	-	-
Hastelloy G-30	Bal	30	1.5	1.5	1.5	0.1	1.5	1.8	1	-
Inocel 718	Bal	22	18	1	0.4	1.9	-	-	-	-

In Ni-based alloys to achieve acceptable oxidation resistance, the Cr concentration must be higher than 15 wt.% ,and 18-19 wt.% of Cr in the alloy composition provides good oxidation resistance [34]. A Small amount of Al is usually added to improve oxidation resistance [34]. Also trace levels of reactive elements such as La, Ce, Y, etc., can be added for a further improved oxidation resistance and scale adhesion [33]. Depending on the composition of the alloy, the oxide scale thermally grown on Ni-based alloys at temperatures around 800°C consists of an inner, dense chromia-rich layer and an outer Cr-Mn spinel [35]. Internal oxidation of Ti occurs when the alloy contains Ti as an alloying element [35]. Both Mn and Ti increase the oxidation specific mass gains. Although Mn increases the oxidation rate of Ni-based alloys, its addition to the alloy composition is beneficial in terms of increasing the scale conductivity and blocking the migrating Cr species. Manganese is able to diffuse through chromia relatively fast and form Mn-Cr spinel on the top of inner chromia scales [35]. The addition of Mo increases the oxidation resistance and reduces the CTE.

Although superalloys show good electrical, mechanical and chemical stability as well as excellent oxidation resistance at elevated temperatures, their application as

interconnects is limited due to the presence of an austenitic matrix phase, which exhibits a large CTE ($18-20 \times 10^{-6}/^{\circ}\text{C}$) that does not match those for the ceramic components of SOFCs ($10-13 \times 10^{-6}/^{\circ}\text{C}$) [6, 8, 21]. However, it has been shown that the addition of Mo and W can decrease the CTE of Ni-based alloys, and research to find low-CTE Ni-based alloys is underway.

1.4.1.2 Chromium-based alloys

Cr-based alloys with body centered cubic (BCC) structure exhibit good CTE compatibility with other cell components. Also, Cr-based alloys show excellent high-temperature mechanical strength. Among the Cr-based alloys, Ducrolloy (from Plansee) has been developed specifically to replace doped lanthanum chromite formerly used as the main interconnect material [34]. Ducrolloy (Cr–5Fe–1Y₂O₃) is an oxide dispersion-strengthened (ODS) alloy containing 5 wt.% Fe and 1 wt.% Y. Other Cr-based alloys with similar compositions as Ducrolloy, but with other reactive oxides (i.e., La₂O₃ and CeO₂) instead of yttria, have been developed and studied. In some of these alloys, ~0.3 wt.% Ti is added to improve oxidation resistance.

Although Cr-based alloys are promising candidates, in terms of oxidation resistance and possibly high-temperature mechanical stability, they are hard and brittle and cannot be easily formed into complex designs [34]. Furthermore, no spinel forms on top of the chromia scales thermally growing on Cr-based alloys and this chromia layer is relatively pure. Thus, the oxide scale's electronic conductivity is not high enough to meet the ASR criteria. Also, volatility of Cr species from relatively pure chromia scales with no outer spinel layer may cause Cr poisoning of the cathode.

1.4.1.3 Stainless steels

In addition to Ni-based superalloys and Cr-based alloys, Fe-based corrosion resistant alloys (stainless steels) have been the subjects for numerous studies in terms of suitability for interconnect applications [10, 23, 36-40].

Stainless steels are Fe-C based alloys, which contain Cr. These alloys are commonly used for their corrosion/oxidation resistance. Stainless steels are classified into four categories including ferritic steels, austenitic steels, martensitic steels and precipitation hardening steels [34]. As can be seen in Fe-Cr phase diagram (Figure 1-4), ferritic stainless steels maintain a ferritic structure up to the solidus temperature unless the Cr content of the alloy is smaller than 13.4 wt.%,. Most commercial grades of ferritic stainless steels contain approximately 18 wt.% Cr to maintain a high-temperature corrosion/oxidation resistance. Addition of small amount of Al can improve the oxidation resistance, but Al content must not exceed 3 wt.% [34]. The martensitic and precipitation-hardening grades are not considered as high-temperature oxidation resistance alloys due to their low Cr concentrations [34]. Also, the application of the austenitic types is not recommended for interconnect purposes due to their high CTE which is not compatible with ceramic parts of the fuel cell [34].

Although a minimum concentration of Cr is required for an optimal oxidation resistance and stabilization of ferritic structure for an acceptable CTE match, Cr concentrations that are too high lead to a phenomenon referred to as sigma phase embrittlement. The sigma phase is an intermetallic compound that precipitates along grain boundaries in the alloy matrix at temperatures in the range of 550-870°C [34, 41]. Some alloying elements such as Mo can promote the formation of a sigma phase [34, 41]. In addition to causing embrittlement, sigma phase reduces the oxidation resistance because its formation locally depletes the Cr by precipitating at grain boundaries in the alloy [34]. The Cr content, therefore, must be kept below 30 wt.% [34].

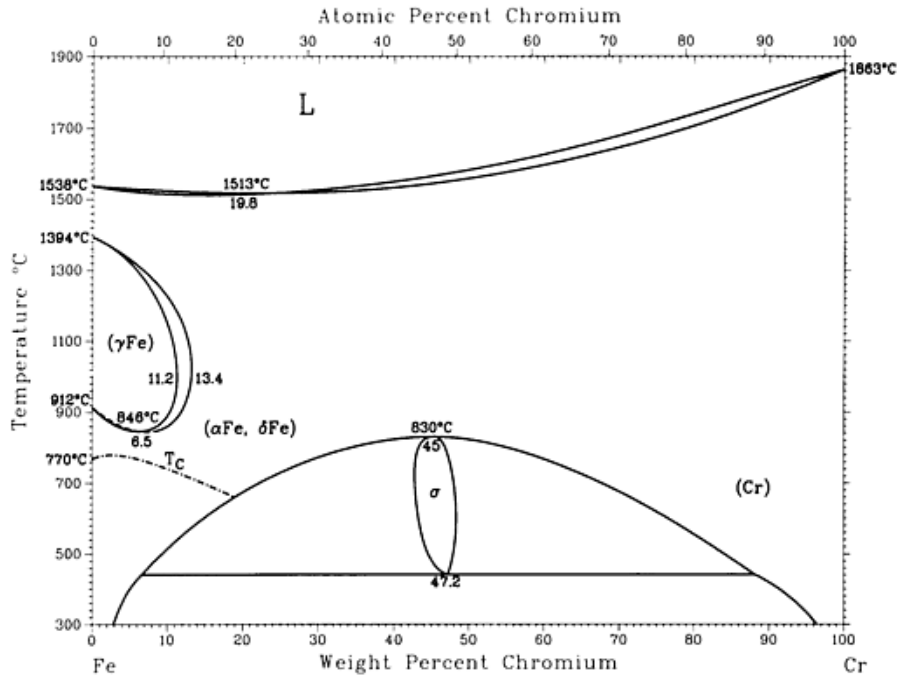


Figure 1-4 Binary phase diagram for Fe-Cr alloys; α -Fe and δ -Fe are BCC and γ -Fe is FCC [42].

Recent interconnect research studies have concentrated almost exclusively on various grades of ferritic stainless steels due to several advantages. The most prominent advantage of ferritic stainless steels over other chromia formers is their excellent CTE match with other ceramic components of the SOFCs. Also, these steels are low-cost and easily fabricated into complex forms. The commercially available grades of ferritic stainless steels, nevertheless, do not meet all the interconnect criteria which will be addressed here.

Commercially available heat-resistant ferritic steels, which are not designed specifically for interconnect applications, suffer from various shortcomings associated with their poor oxidation resistance and oxide scale properties. High-temperature oxidation of ferritic stainless steels containing specific levels of Mn (>0.5 wt.% as an impurity) results in the formation of a double-layer oxide scale. This double-layer oxide scale consists of a protective chromia-rich (containing Fe) subscale and an outer non-protective Cr-Mn spinel layer (containing trace

levels of Fe) [12, 38, 40, 43-45]. Depending on whether the steel contains Si and/or Al, insulating, continuous or network-like layers of silica or alumina can also grow underneath the chromia-rich scale [15, 40, 43, 45]. Chromia-rich layers grow by outward diffusion of Cr cations from the substrate surface through chromia-rich scale grain boundaries [46]. Outward diffusion of Cr results in the formation of voids at the metal/oxide scale interface [47]. The presence of voids at the interface, large CTE differences with the substrate and brittleness of chromia-rich scales result in cracking and spallation of the scale during thermal cycling inducing thermal stresses. In addition, Cr migration and cathode poisoning are issues associated with chromia-rich oxides. Cr-Mn spinel outer scales, however, are beneficial since spinel layers are capable of absorbing the migrating Cr species and retarding Cr poisoning [9, 31]. Also, spinel scales are good electronic conductors in comparison with chromia [48]. The formation of silica and/or alumina layers is detrimental for conductivity for alloys where Si and Al concentrations are high enough to form continuous, insulating layers.

Coatings, surface treatments and alloy bulk composition modifications and developments have been regarded as potential remedies in order to overcome the issues originating from the poor high temperature oxidation properties of ferritic stainless steels.

1.4.2 Coatings for ferritic stainless steel SOFC interconnects

Various coating techniques and materials have been used in an effort to decrease the oxide growth rate, increase the scale conductivity, improve oxide scale-to-metal adhesion and inhibit Cr migration to the scale surface and Cr poisoning of the cathode material. Sol-gel coating [24, 25, 49, 50], pulsed laser deposition [51], plasma spraying [52-61], slurry coating [62-65], RF-magnetron sputtering [66-75], large area filtered arc deposition [76-78] and electrodeposition [79-83] have been used for coating of ferritic stainless steels. The materials used for coating purposes include reactive element oxides (REOs) [24, 25, 49, 84], conductive

perovskites [13, 54, 57, 66-69, 71, 72, 74, 75, 79, 83], conductive spinels [65, 79-83, 85-98], conductive/composite spinels and MAICrYO (M represents Fe, Co or Ni) heat-resistant systems [76, 77]. Some of the selected functional coating systems for stainless steel interconnects will be discussed here.

1.4.2.1 Reactive element oxide (REO) coatings

Ample experimental observations show that the addition of small amounts of reactive elements (e.g., Y, La, Ce, Hf, etc.) or their oxides in the form of dispersed particles effectively decelerate the high-temperature oxidation rate and greatly improve oxide scale-to-metal adhesion for alumina and chromia formers [99-111]. The mechanisms through which reactive elements improve the oxidation resistance of high-temperature alloys are yet not fully understood. Various mechanisms have been suggested and reviewed in the literature [103]. Coatings containing REOs can efficiently increase oxide scale-to-metal adhesion and reduce oxide scale thickness; thereby decreasing the ASR of steel interconnects which is directly proportional to oxide thickness, oxide conductivity and the surface area of metal/oxide scale contact.

The most popular techniques used for application of REO coatings include sol-gel and metal-organic chemical vapour deposition (MOCVD) [112-114] although other methods like ion implantation may be used. Almost all REO films are thin (less than a micron) and can form perovskites when reacting with Cr diffusing from the chromia-rich scales forming underneath the coating layers.

In a sol-gel technique, an aqueous, concentrated solution containing reactive element salts, particularly nitrates, is applied on the surface of the substrate. Following the application of the precursor, the coated substrates undergo drying and heat-treatment in order for the nitrates to dissociate and form oxides. A nano-scale thick REO layer then remains on the surface. The process is simple and does not require sophisticated instruments. Qu et al. [49] used two types of sol-gel

coatings, Y/Co and Ce/Co, for AISI-SAE 430* stainless steel substrates with the purpose of reducing the oxidation rate of the steel and increasing the conductivity of the chromia-rich scales. The so-gel solution used in their study for the Y/Co coatings contained yttrium nitrate and cobalt chloride, while the solution used for the Ce/Co coatings consisted of cerium chloride and cobalt chloride. Yttrium and Ce are reactive elements that can improve the oxide scale-to-metal adhesion and reduce the oxidation rate. Cobalt is regarded as a p-type dopant that can increase the conductivity of the chromia-rich scale. Oxidation test results, performed at 750°C in air for 1000 hours, showed that the oxide scale thickness using the Y/Co coating was less than 1 μm and the oxide thickness with application of the Ce/Co coating was between 1 and 1.5 μm . The uncoated samples had an oxide scale thickness of around 3 μm . This shows that the Y-containing coating is more effective in reducing the oxidation rate of the substrate compared to the Ce-containing coating. It was found that Y accumulates mostly in the chromia-rich grain boundaries where it may inhibit Cr cation outward diffusion leading to slower oxidation kinetics. Cerium appears as ceria particles at the chromia-rich/Mn-Cr spinel interface in Ce/Co coated, oxidized samples. The ceria particles also acted as markers, and their presence at the boundary indicated that oxygen anions were the dominant diffusing species. In the absence of reactive elements, Cr outward diffusion is the predominant mechanism for oxidation. Cobalt was mostly distributed in the spinel phase in both cases.

Qu et al. [24] in another study examined the effect of sol-gel coatings containing Y, Co or both Y and Co on the oxidation kinetics and ASR of AISI-SAE 430 substrates. It was found that Y coatings reduced the oxidation rate by at least a factor of two and the ASR by at least a factor of four in comparison with uncoated, identically oxidized steels. Cobalt coatings increased the oxidation rate, the amount of spinel phase and scale thickness. No spallation occurred with Y and Y/Co coatings, but occurred for uncoated and Co coated specimens. Cross sectional scanning electron microscopy (SEM) images in their work showed

* For composition, see Table 1-3

excellent oxide scale-to-metal adhesion for the Y and Y/Co coated steels. The ASR results for Y and Y/Co coated samples showed virtually the same values, indicating that Y plays the key role in enhancement of conductivity. Although sol-gel coatings of REOs have been shown to significantly enhance scale adhesion and electronic conductivity, their application as Cr migration barriers has not been studied. These coatings, however, are normally thin (e.g., $>0.2\mu\text{m}$) and may not be effective at inhibiting Cr diffusion to the oxide surface and preventing Cr poisoning.

The alternative technique for deposition of REO is the MOCVD process that was originally introduced by Eisentrant and Sievers [115-119]. In this process, volatile rare earth chelates (usually β -diketonates) are used as precursors. The precursor is heated to evaporation. The vapour along with carrier gases (N_2 and/or O_2) is then injected into a controlled atmosphere furnace, which heats the substrate. The precursor vapour is then dissociated on the hot substrate surface and deposits a layer of reactive oxides. The byproduct gases are removed from the reaction chamber by the gas flow. This technique has been widely used in the semiconductor industry and to a lesser extent for SOFC applications [112-114]. The following paragraphs summarize some examples for REO coatings.

Cabouro et al. [120] have studied Y_2O_3 coatings for Fe-30Cr alloys, applied by means of MOCVD. The precursor used in the study was an organic compound of Y (tris-2,2,6,6-tetramethyl-3,5-heptanedionato yttrium ($\text{Y}(\text{tmhd})_3$)). The precursor was applied at 170°C on the hot substrates (600°C) while O_2 and N_2 were fed along with the precursor gas into the reactor. The coating thickness obtained with this technique was 100 nm. The application of Y_2O_3 via this technique resulted in significant improvements in terms of oxidation resistance, chromia scale grain refinement and ASR. Spallation and cavity formation under the scale were also eliminated. However, Cr migration and poisoning were not addressed in this work.

Another example of REO coatings by MOCVD is the study conducted by Fontana et al. [112]. In this study, Crofer 22 APU, AL453 and Haynes 230 substrates were coated with La_2O_3 , Y_2O_3 and Nd_2O_3 . The thickness of the scale was 100-200 nm. The aim of this work was to form a conductive perovskite layer via reaction between the coated binary oxide and Cr from oxide scale. Among various combination of REO coatings and substrates, La_2O_3 -coated Crofer APU showed superior improvement particularly in terms of ASR. Other coating/substrate combinations also proved effective in reducing the oxidation rate and contact resistance, as well as elimination of the oxide scale spallation. Regardless of the improvements achieved, the coatings investigated in the research were not aimed to surpass Cr migration. The coatings may not be effective in blocking Cr diffusion.

1.4.2.2 Rare earth perovskite coatings

Rare earth perovskites have the general formula of ABO_3 where A is a large rare earth cation (e.g., La) and B is usually a transition metal cation (e.g., Cr). The ideal crystal structure is cubic. Rare earth perovskites exhibit p-type electronic conduction in oxidizing environments and are stable in low oxygen partial pressures [16]. The electronic conductivity drops when the partial pressure of oxygen is low [16]. Low oxygen partial pressure leads to the formation of oxygen vacancies leaving electrons behind and, thus, consuming electron holes [16]. Large earth alkali cations with large ionic radii (e.g., Sr and Ca) can replace the rare earth cations on A sites. Also, perovskites can be doped with electron acceptors (e.g., Ni, Fe and Cu) at B sites. Doping can greatly increase the conductivity by up to two orders of magnitude [7]. Appropriate doping can also modify the CTE of conductive perovskites [7]. In addition to the advantages of being conductive and exhibiting compatible CTE, rare earth perovskites can supply reactive elements (e.g., La) to the underlying, growing oxide scale. Application of their coatings may decrease the oxidation rate and improve scale adhesion and, thus, reduce the ASR.

The most commonly used perovskites for conductive coating purposes are lanthanum strontium chromite (LSC) [71, 121], undoped lanthanum chromite (LC) [50, 69, 72], lanthanum strontium manganite (LSM) [54, 67, 68, 122], lanthanum strontium cobaltite [57, 71] and lanthanum strontium ferrite (LSF) [74, 83], even though other perovskites may give similar results. Perovskite coatings may be applied on stainless steel substrates by a variety of techniques including sol-gel [13], radio-frequency (RF) magnetron sputtering [66-69, 71, 72, 74] and plasma spraying [53, 57-60].

In rf magnetron sputtering, coatings with insulating materials are possible due to the existence of a resonating circuit which couples the insulating electrode and maintains the discharge [123]. An oscillating power source with a frequency higher than 50Hz is required for RF sputtering [123]. Usually for this purpose, an RF generator is connected to grounded chamber walls or the specimen holder [123]. Due to the ability of the technique to coat with ceramic materials, this method has been used for perovskite coatings. However, thick coatings (thicker than 1 μ m) are impractical to deposit utilizing RF magnetron sputtering.

Yang et al. [74] studied two types of perovskite coatings including LSF and LSC for application as protective/conductive coatings for different grades of ferritic steel substrates including E-brite*, Crofer 22 APU* and AL453*. The perovskite films were applied on the steel substrates via radio frequency (RF) magnetron sputtering. The coating thickness attainable with this method was 3-4 μ m. The coatings obtained were not fully dense and contained porosity and cracks. Both coatings proved to be effective at reducing the ASR of the substrates for relatively short test periods (~250 hours at 800°C). Superior results were achieved with the application of LSF relative to LSC coatings in terms of protection against oxidation and electrical properties. This was attributed to the lower ionic conductivity of LSF, reduced oxygen anion inward transport and, thus, better

* For composition, see Table 1-3

protection against oxidation. Among different substrates used in their study, E-brite exhibited the highest oxidation resistance with the application of coatings. These coatings, however, did not prevent oxidation of the substrate and the formation of a chromia-rich subscale. The ionic conductivity, porosity, cracking and non-protective nature of these films resulted in easy inward transport of oxygen. Also, such coatings are not known to be capable of inhibiting or reducing Cr outward migration from the chromia-rich subscale growing underneath.

Johnson et al. [69] studied lanthanum chromite coatings applied by RF magnetron sputtering on AISI-SAE 446* steels. The as-deposited film was amorphous and transformed to a dendritic, porous crystalline state upon a two-step heat-treatment at 300°C and 500°C for 15 minutes followed by 1 hour at 700°C. The coated steels, however, were not tested in terms of oxidation resistance, the ability to block Cr migration or conductivity improvement. Belogolovsky et al. [121], from the same research group, studied lanthanum chromite-based nanocrystalline coatings of $\text{La}_{0.8}\text{Sr}_{0.2}\text{CrO}_3$ and $\text{LaCr}_{0.9}\text{Zn}_{0.1}\text{O}_3$ synthesized with polymeric solutions containing La, Cr, Sr and Zn nitrates for E-brite substrates. The coatings were reported to reduce the oxidation growth rate considerably at 750°C. Chromia overgrowth and grain coarsening of the coating, however, occurred at 850°C. The coatings were also capable of blocking 70% of the Cr evaporation that happened for uncoated substrates at 900°C. The conductivity and oxide scale adhesion were also improved by application of these films.

Plasma spray coating is an alternative technique that can apply ceramic coatings with a thickness range of 0.05-0.5 mm on various substrate materials. The plasma torch consists of a water-cooled Cu anode and a W cathode [124]. The gas used for plasma generation is normally Ar or N_2 and H_2 or He. An oscillating voltage generates the arc and a direct current maintains it. Once plasma is produced, the coating powder can be fed into the torch where it melts and is accelerated in the plasma jet. The gas temperature exiting the nozzle can reach 10,000°C with high velocity at the nozzle position. Once the gas exits the nozzle, it expands and cools

on the substrate resulting in rapid solidification of the injected coating material on the cold surface of the substrate [124]. With this technique, relatively thick coatings of high melting point ceramics can be deposited on metallic or ceramic substrates. However, due to rapid solidification and thermal stresses, cracks and internal porosity are common in the coating layers. The other limitation associated with this technique is that uniform coverage of coating depends on the line-of-sight between the torch and substrate. As a result, coating of complex-shape interconnects is not practical via this technique. To achieve the desired layer properties, numerous parameters including torch design, power size distribution, carrier gas and atmosphere must be carefully selected [124].

Fu et al. [125] have studied a LSF coating by an atmospheric plasma spray technique for AISI-SAE 430 steel. The objective of their work was to reduce the oxidation rate and mitigate the Cr poisoning issue. The coating layer achieved with this technique was porous. In order to reduce the porosity of the coating, a densification process referred to as nitrate impregnation was used after spraying. In this process, the coated samples were immersed in an aqueous solution of La, Fe and Sr nitrates and then sintered at 800°C for 2 hours. The final coating thickness was 120 µm. The coated specimens showed a much smaller oxidation parabolic rate constant in comparison with uncoated steels ($k_p = 0.15$ vs. $8.5 \cdot 10^{-14} \text{ g}^2 \text{ cm}^{-4} \text{ s}^{-1}$). The ASR for the coated substrate was 0.001 $\Omega \text{ cm}^2$ after 1000 hours of oxidation in air at 800°C. The coatings were also effective in Cr retention due to the large coating thickness.

Despite the limited improvements achieved with the application of perovskite films, such coatings do not substantially inhibit Cr migration or they adsorb migrating Cr species resulting in Cr poisoning. These films are not successful oxidation protection layers, since they are ionically conductive and are not fully dense. In addition, the application techniques for such coatings are practically difficult and expensive.

1.4.2.3 Spinel coatings

Cubic spinel has the general formula of AB_2O_4 with A and B as divalent, trivalent and quadrivalent cations in octahedral and tetrahedral sites and oxygen anions on the face centred cubic (FCC) lattice points. Spinel coatings have been attracting considerable attention recently. Depending on the choice of A and B cations and their ratio, spinels can be good electronic conductors and show excellent CTE match with the ferritic stainless substrate and other cell components, including the anode and cathode. Spinel coatings have shown excellent capability for absorbing Cr species that can migrate from the chromia-rich scale to the scale surface and cause Cr poisoning [85, 87, 89]. Several research studies have been conducted to evaluate the suitability of different spinel compositions for application as potential conductive/protective coatings for stainless steel interconnects.

Electronic conductivity and CTE of various spinel compositions, including Ni-Cr, Co-Cr and Mn-Cr spinels, have been studied by Qu et al. [48]. Spinel powders in their study were synthesized from metal oxide powders by solid-state reaction followed by ball milling. The powders were then pressed and sintered at elevated temperatures to produce pellets and bars for electrical and microstructure examination. All spinel systems tested, including $NiCr_2O_4$, $CoCr_2O_4$ and $MnCr_2O_4$, showed similar CTE values in the range of $7.2-7.6 \times 10^{-6}/^{\circ}C$ that are close to that for chromia ($CTE = 9.6 \times 10^{-6}/^{\circ}C$) at $25-900^{\circ}C$. It was also found that only $MnCr_2O_4$ and $NiCr_2O_4$ showed lower resistivities than chromia.

Petric and Ling [126] reviewed and studied the thermal and electrical properties of a vast variety of binary spinels containing Mg, Al, Cr, Mn, Fe, Co, Ni, Cu and Zn. It was found that spinels containing Fe exhibited the closest CTE values to ferritic stainless steels. CTEs for other spinels tested were between $7-9 \times 10^{-6}/^{\circ}C$, but the Cu-Mn and Co-Mn systems behaved anomalously. The highest conductivities were achieved with $MnCo_2O_4$ (60 Scm^{-1} at $800^{\circ}C$) and $Cu_{1.3}Mn_{1.7}O_4$ (225 Scm^{-1} at $750^{\circ}C$). The authors stated that $Mn_xCo_{3-x}O_4$, Cu_xMn_{3-x}

$x\text{O}_4$ ($1 < x < 1.5$), Co_3O_4 and CuFe_2O_4 were the best candidates for the purpose of interconnect coatings, although there was no ideal composition.

Slurry coating methods including spraying [86, 95] or screen printing [85, 89] and plasma spraying [93] have been the main application techniques for spinel coatings in past years. Recently, electrodeposition of metals followed by heat-treatment/oxidation has been considered as a new technique for spinel coating [79, 83, 90, 92]. Also, anodic electrodeposition of oxides from aqueous solutions containing metal salts followed by heat-treatment has been reported as a method for spinel coating [80, 98].

Mixing spinel powders with an organic binder to make pastes and slurries have also been used for coating. A spinel powder with the desired properties is usually synthesized by high-temperature, solid state reactions between oxides and/or carbonates of the spinel forming metals. A glycine-nitrate process [127] (known as GNP), followed by an optional milling process is an alternative way of producing quality spinel powders. In ceramic powder synthesis with GNP, glycine and metal nitrates of interest are dissolved in water to form an aqueous solution. The resultant precursor is then heated until the excess water evaporates leaving a viscous liquid behind. Further heating of this viscous liquid results in auto-ignition and production of a flame, heat, H_2O , CO_2 , N_2 and mixed metal oxide powders. GNP can yield fine (nano-scale), homogenous ceramic powders if the precursor stoichiometric ratios and reaction conditions are carefully adjusted. Dry milling is optionally subsequently utilized to further reduce the powder size and improve its homogeneity. GNP is widely employed for synthesizing ceramic powders used in fabricating SOFC materials including the cathode, anode and interconnect [127-151].

Chen et al. [95] have studied Mn-Co spinel coatings on AISI-304 stainless steel. In their work, a slurry spraying technique was used. The powders were synthesized using GNP. The coatings were subsequently mechanically

compressed to improve the green density prior to heating. The authors pointed out that the coating, which was dense and highly adherent to the substrate, significantly reduced the oxidation rate of the substrate. However, the ability of the coating to reduce Cr migration was not evaluated in their study.

Yang et al. [85] have investigated a Mn-Co spinel coating with nominal composition $\text{Mn}_{1.5}\text{Co}_{1.5}\text{O}_4$ applied by means of screen printing on Crofer 22 APU substrates. The powder used for screen-printing was synthesized by solid-state reaction of Co_3O_4 and MnCO_3 . The coating improved the electronic conductivity of the substrate and acted as an effective barrier against Cr migration. The ASR value for the spinel coated substrates was approximately $0.01 \text{ } \Omega\text{cm}^2$ after 1000 hours of oxidation in air at 800°C , while the ASR value for uncoated substrates under identical conditions but after 400 hours was $0.04 \text{ } \Omega\text{cm}^2$. Yang et al., in another study [65], used two different methods of spinel powder preparation including solid state reaction between Co_3O_4 and MnCO_3 and GNP. Powders prepared via GNP had finer and more homogenous particles which improved the coating density and performance compared to those synthesized by solid-state reaction. Spray or screen printing techniques were used to coat steel substrates such as Crofer 22 APU, E-Brite and AISI-SAE 430. Coated specimens were heat treated in a reducing atmosphere (i.e., $\text{Ar}/3\text{H}_2\text{O}/4\text{H}_2$) at 800°C for at least 2 hours. Annealing in air subsequently developed the spinel phase. This procedure was conducted to achieve high-density spinel coatings. Significant improvements in terms of contact resistance and oxidation protection were achieved only for high-Cr substrates, i.e., Crofer 22 APU and E-Brite.

A $\text{MnCo}_{1.9}\text{Fe}_{0.1}\text{O}_4$ spinel coating for Crofer 22 APU, F18TNb*, IT-11* and E-brite steel substrates was developed and studied by Montero et al. [91]. The specimens in their study were coated by screen-printing with $\text{MnCo}_{1.9}\text{Fe}_{0.1}\text{O}_4$ spinel paste. The coating thickness was approximately $60 \text{ } \mu\text{m}$. Reactive sintering was used for densification of the coated paste. This procedure included a reduction step, which

* For composition, see Table 1-3

was performed at 800°C in a reducing, low oxygen partial pressure gas mixture consisting of Ar/3H₂O/4H₂. The reduction step was followed by an oxidation stage in air at 800°C to reform the spinel. The authors pointed out that such a coating can effectively reduce the contact resistance between the cathode (LSF) and the steel. This coating also inhibited Cr outward diffusion and, thus, Cr poisoning. The presence of Mn in the alloy composition determined the effectiveness of the spinel coating. For Crofer 22 APU and F18TNb substrates, which contain small amounts of Mn, a decrease in ASR was noticeable, while the coating exhibited no significant improvement for IT-11 and E-brite, which contain negligible or trace amounts of Mn.

In Garcia-Vargas et al.'s [93] work, atmospheric plasma spraying (APS) of MnCo₂O₄ spinel followed by wet powder spraying of the same material was employed. APS produces a dense, protective spinel layer while the wet powder spray forms a porous layer on the top of the dense, protective layer. The purpose of the top porous spinel layer is to increase contact with the cathode and re-heal the stresses possibly caused by differences in CTE of the cell and interconnect. The substrate used in their work was F17TNb* ferritic stainless steel. A relatively low, stable ASR of 0.05 Ωcm² was obtained after 600 hours of oxidation at 800°C in air. The dense, protective spinel layer effectively reduced Cr outward migration.

The adhesion of the coating to the substrates, the difficulty of the synthesizing fine, homogenous spinel powders and the porosity of the coatings applied are issues when employing slurry and plasma spray techniques.

Recently, electroplating of metals or alloys followed by air annealing/oxidizing to form spinel layers directly on the steel substrates has been considered as an advantageous technique for spinel coating. The advantages of electrodeposition techniques over slurry and plasma spray methods include better coating-to-substrate adhesion, denser, less porous spinel layers and good coverage of the

electrodeposited coating on all substrate surfaces especially for complex-shaped interconnects. The thickness of the final spinel layer can be easily controlled by adjusting the deposition parameters (i.e., current density and time).

Electrodeposition or electroplating refers to a range of processes in which a metal or alloy is deposited on conductive substrates from an electrolyte. The electrolyte is usually an aqueous solution containing simple metal salts or complexes. Molten salt electrolytes can also be used where deposition from aqueous solutions is not possible (e.g., Al). Electrodeposition is based on reduction and oxidation reactions occurring on the cathode and anode respectively by application of an external, direct or pulsed-direct current source. Upon application of the external current source, the hydrated positively charged metal ions in the electrolyte are reduced on the negatively charged, conductive cathode. Depending on the electrolyte composition and condition, the overpotential and the metal being deposited, hydrogen reduction and evolution can also take place at the cathode. The cathode surface must be conductive, clean and chemically active (free of native oxides and passivating layers) in order for a continuous, adherent coating layer to grow uniformly on the surface. The anode is where oxidation reactions take place. The anode may be used to replenish the consumed metal ions in the solution. In this case, the anode is consumable. In some cases where the dissolution of the anode in the electrolyte does not occur or is spontaneous, non-consumable, low polarization materials (e.g., Pt) are used as the anode. For non-consumable anodes, instead of metal dissolution, oxidation of water, the formation of protons and evolution of oxygen occur. The electrolyte used in electroplating can be acidic, basic, neutral or chelated. The choice of electrolyte depends on the stability and solubility of the metal compounds used and the desired coating characteristics such as mechanical properties, corrosion resistance and appearance. Also, a variety of organic or inorganic additives may be added to obtain some desired coating properties. These additives are sometimes an essential part of the electrolyte solutions. Wetting, levelling, brightening and residual stress reducing agents are among the additives normally used in aqueous

electroplating solutions. The electroplating process continues as long as the external current source is connected to the anode and cathode and there is adequate metal ion supply in the electrolyte. Thus, coating thickness can range widely (a few nano-meters to hundreds of microns) using this technique. The amount of material reduced on the cathode surface depends on the total charge consumed according to Faraday's law. However, the efficiency is not 100% due to contributions from several overpotentials including activation and concentration overpotentials.

The coating layer forms on the cathode surface through a sequence of steps. The first step after application of the current source is migration by diffusion and/or convection of hydrated metal ions or complexes toward the negatively charged cathode. The second step is diffusion through Nernst boundary layer formed as the result of concentration gradient across the cathode surface and the electrolyte bulk. The third step is reduction of metal ions at the cathode surface. Once the metallic ions are reduced on the surface, free metal ions start to diffuse on the surface to reach suitable sites to be adsorbed. The suitable sites can be surface defects such as dislocations. The coating layer may grow through nucleation and two-dimensional, lateral growth.

Spinel coating via electrodeposition is performed basically by plating sequential layers of the desired transition metals (e.g., Mn, Co, Cu, Fe, Ni, etc.) or alloys on the stainless steel substrates followed by a subsequent heat treatment in air. Annealing in air results in oxidation of the electrodeposited metallic layers. Upon oxidation, an adherent surface layer of an oxide mixture and/or a spinel structure forms.

As mentioned previously, it has been found that Mn-Co and Cu-Mn spinels exhibit good conductivity and CTE match with ferritic substrates. Most research efforts have focused on these spinel systems for application as conductive/protective coatings. Wei et al. [90] were the first to develop and study

Mn-Co and Cu-Mn spinel layers obtained by sequential electrodeposition of Mn and Co, as well as Cu and Mn, on AISI-SAE 430 stainless steel substrates. In their work, electroplating of Mn was conducted in a double compartment cell including a cathode compartment filled with manganese and ammonium sulphate as a catholyte (electrolyte in the cathode compartment) and an anode compartment using ammonium sulphate as an anolyte (electrolyte in the anode compartment). Glass frit tubes separated the two compartments. Cobalt chloride and sulphuric acid/copper sulphate plating baths were employed to deposit Co and Cu, respectively. Annealing of the coated steel was performed in argon for two hours at 800°C in order for interdiffusion of the sequentially deposited layers to occur. This also enhanced coating-to-substrate bonding. Oxidation tests and electronic conductivity measurements for the coated/annealed samples were done at 750°C in air. It was shown that oxidizing of the sequentially plated metallic layers led to the formation of cubic spinel phases. The coatings obtained via this technique were shown to effectively protect the substrate and totally eliminate Cr outward diffusion. The ASR for both coatings was reported to be 0.003 Ωcm^2 at 750°C after 1500 hours of oxidation, which is markedly small compared to uncoated AISI-SAE 430 steel. In another study [79], the authors characterized the same Mn-Co and Cu-Mn spinel coatings in terms of microstructure. After 7 days of oxidation at 750°C, a relatively thick layer (~5-10 μm) of chromium-rich oxide formed under the spinel layer. Formation of this thick chromia-rich layer may have been due to interdiffusion of the coated metals into the substrate, which diluted the adjacent substrate surface in Cr. If the Cr content of the substrate is less than critical the Cr concentration threshold (i.e., 11 wt.%), the chromia layer will not be dense and pure enough to be protective. Localized breakdown of the thick, non-protective chromia-rich scales may happen at higher temperatures resulting in so-called breakaway oxidation and the formation of surface Fe-rich oxide nodules. The authors did not address this issue. The ASR, however, will not be adversely affected due to the high concentration of substrate elements (e.g., Fe) which can act as dopants in the chromia-rich scale and significantly increase the conductivity. The structure of the inner oxide layers was not identified by XRD

since the thermally grown oxide was too thick for the incident X-ray beam to penetrate deep enough. In addition to the Cu-Mn spinel, copper oxides were present in the scale, depending on the Cu:Mn ratio in the as-deposited coating. Outward diffusion of Fe into the coating layers and inward diffusion of Co into the substrate were also detected. Both spinel coatings showed effective inhibition of outward Cr migration.

Cobalt-Mn spinel coatings on AISI-SAE 430 stainless steels, fabricated by electrodeposition/annealing, were also studied by Wu et al. [94, 97]. In one study [94], the authors used direct current (DC) alloy electroplating of Co and Mn. The electrolyte used for alloy plating in their study was a solution of Co and Mn sulphates buffered/complexed by boric, gluconate and ammonium sulphate. The Co:Mn sulphate ratio in the electrolyte was 0.02-0.2. There are a number of deficiencies with DC alloy plating of Mn-Co via this technique. Since there is a large difference between the standard electrode potentials for Co (-0.277 vs. standard hydrogen electrode (SHE)) and Mn (-0.180 vs. SHE), electrolyte composition and electrodeposition parameters must be carefully adjusted to achieve the desired deposit composition. Although increasing the current density increases the Mn content of the deposit, Mn hydroxide may co-deposit on the cathode as the local pH in the vicinity of the cathode surface rises dramatically due to hydrogen gas evolution. The addition of buffers (i.e., ammonium sulphate) reduces this effect. Also, chelating agents (i.e., sodium gluconate), when used in sufficient amounts to fully chelate all free metal ions, can eliminate hydroxide formation. The excess amount of chelating agents inhibits the reduction and deposition of metal ions, particularly Mn in this case. If the maximum chelating agent concentration is used, to obtain the target deposit composition (Mn:Co=1), high current densities are needed. The use of high current densities results in spongy, porous deposits. Although oxidation of such porous coatings reduces the porosity, outward diffusion of Mn from the substrate occurs due to the very small thickness of the porous electrodeposited layer. This leads to compositional changes in the coating from the substrate to Mn-rich, Mn-Co spinel. Moreover,

although keeping the concentration of the nobler metal in the electrolyte (i.e., Co) quite small allows the desired deposit composition to be achieved, continuous consumption of the nobler metal in the electrolyte (i.e., Co) results in its rapid depletion. The electrodeposition rate is also very slow and the deposits achieved are too thin (1.5 μm) due to the low cathodic current efficiency achieved with this electroplating technique. The same authors, in another study [97], used pulsed plating instead of DC plating in order to control the Mn:Co ratio more effectively and achieved a denser and more uniform coating morphology. No significant improvement, however, was achieved with pulse plating as Mn dissolves instantly during off-time periods. Coating porosity decreases as the coating oxidizes and expands to form spinel crystals, which have lower densities than the metallic layer. Outward diffusion of Mn still happens changing the composition of the spinel from that of the target value (Co:Mn=1). Outward Cr diffusion, however, is essentially inhibited even after 1200 hours of oxidation at 800°C. ASR values remain almost stable and approach 0.024 Ωcm^2 after 1200 hours period of oxidation.

Electrodeposition/annealing of pure Co on AISI-SAE 430 stainless steel was studied by Deng et al. [92]. The electrolyte used in their study was a sulphate/chloride Co plating bath containing boric acid as the buffer. The coating thickness was 20-40 μm . In order to improve coating-to-substrate bonding, the coated steels were annealed in forming gas at 1000°C for 2 hours. Diffusion of Cr and Fe from the substrate into the coating and Co diffusion from the coating into the substrate occurred during annealing. As the annealed, coated samples were subsequently oxidized in air, a top layer of Co_3O_4 formed with a spinel solid solution containing Co, Cr and Fe underneath. Also, a relatively thick chromium-rich oxide (~5-7 μm) formed under the spinel layers as the innermost scale. The coating exhibited a very stable, low ASR of 0.025 Ωcm^2 after 1900 hours of oxidation at 800°C in air. Chromium outward migration was effectively retarded by applying the coating. The spinel layer, however, appeared porous in cross-sectional SEM images.

Alternatively, a mixture of metal oxides can be anodically deposited on the steel surfaces from aqueous solutions containing metal salts and complexing agents. The as-deposited oxide layers are usually nano-crystalline or amorphous [80]. Subsequent heat treatment of the as-deposited oxides results in crystallization and transformation of the mixed oxides to crystalline spinel structures [81, 82]. In this method, the thickness of the coating is limited as the anode surface becomes covered with non-conducting oxides during anodic deposition. This procedure was developed by Wei et al. [98] who were the first to use anodic electrodeposition for Co-rich, Co-Mn spinel coatings on a ferritic stainless steel for the purpose of high-temperature oxidation protection. The electrolyte used in this work contained Co and Mn sulphates and ethylenediaminetetraacetic acid (EDTA) as the complexing agent [80]. The cathode used was a Pt mesh [80]. It was found that increasing the solution temperature to higher than 70°C and the use of small current densities ($\sim 5 \text{ mA/cm}^2$) yield crack-free oxide layers [80]. Lower temperatures and higher current density led to crack formation, the mechanism of which is not clear to the authors [80]. The composition of the coating was easily controlled by adjusting the deposition temperature, the ratio of the metal salts in the electrolyte and current density. Increasing the solution temperature, the Co/Mn ratio in the solution and current density (up to 30 mA/cm^2) increased the Co content of the deposits [80]. The target Co:Mn ratio in the deposit was around 1:1 in order to achieve a more conductive spinel. The structure of the as-deposited oxide was a nano-crystalline, metastable and defective sodium chloride-type structure, which was independent of the deposition conditions and coating composition [80]. Annealing of the as-deposited oxide, which has a defective rock salt structure, led to its transformation to FCC spinel or a distorted tetragonal spinel depending on the Co content of the oxide [82]. Co-rich oxides transformed to cubic spinel while their Mn-rich counterparts transformed to a tetragonal spinel structure [82]. The phase transformation happened at temperatures above 500°C and is associated with reduction of Co and Mn cations to lower valences, migration of these cations from

octahedral interstices to tetrahedral ones and the loss of oxygen [82]. In another work, Wei et al. [98] studied the protective and electrical properties of Co-Mn spinel coatings obtained by anodic electrodeposition. Two types of atmospheres were used to transform the as-deposited, defective NaCl structure to the cubic spinel structure. The environments selected for this purpose included air and forming gas (5% H_2 - N_2), both at 800°C for 10 hours. Annealing in a reducing atmosphere led to formation of a structure consisting of small metallic Co particles in an Mn_3O_4 matrix. A very thin layer of chromia and Si-rich oxides also formed beneath the coating. Pre-treating in air, however, resulted in spallation and formation of micro-cracks in the coating. Chromium from the substrate and the chromia-rich subscale diffused through the air pre-treated coating and formed a spinel solution layer containing Mn, Co and Cr. It was also found that only the coatings pre-treated in forming gas showed protective properties, good adhesion to the substrate and an effectiveness in reducing the ASR values relative to the uncoated substrates.

1.4.3 Surface treatments/modifications

Mechanical, thermal, thermo-mechanical, electrochemical and chemical surface treatments can profoundly affect the oxidation kinetics and oxide scale properties of high-temperature alloys [152]. Mechanical surface deformation (cold work) increases the number of defects, particularly dislocations, in the alloy surface layers. The defects induced by cold working provide rapid diffusion pathways for the oxide forming elements (i.e., Cr) to diffuse through the alloy surface region and to replenish those supplying the growing oxide scale [153]. During the initial stages of oxidation, the abundance of such fast diffusion paths leads to the accelerated nucleation and lateral growth of chromia to form a continuous, protective layer [153]. Since the temperature at which an interconnect alloy must operate is higher than the recrystallization temperature, after formation of the protective oxide film, the deformed surface grains undergo recrystallization resulting in a higher number of grain boundaries. These grain boundaries further

supply the oxide forming element from the bulk to the surface region of the alloy and prevent the dilution of the surface in Cr [43]. Therefore, it is expected that upon surface deformation, a more protective, denser scale will grow on the alloy surface.

Cooper et al. [43, 152] studied the effect of sandblasting and cold rolling on oxidation kinetics of three different types of ferritic stainless steels including AISI-SAE 430/434* and Hitachi ZMG232*. The authors found that deformation increased the parabolic rate constant for oxidation of all three steels. Also, the proportion of spinel-to-chromia decreased or remained unchanged with surface deformation. No information on the effect of surface deformation on electrical properties and scale-to-metal adhesion, however, was reported in the authors' work.

Belogolovsky et al. [154] have studied the effect of various surface treatments on chromia scale adhesion for AISI-SAE 430 steels. The surface treatments included polishing with 240 and 600 grit sandpapers, electropolishing in phosphoric/sulphuric acid solution, pickling in hydrofluoric/nitric acid, sand blasting, heat-treating in a reducing atmosphere and applying Y nitrate coatings on both reduced and untreated samples. They measured the oxide scale-to-metal adhesion via a tensile pull tester for both treated and untreated samples which were oxidized in air at 800°C for 458 hours and cooled rapidly to room temperature. The results of the pull tests are shown in Figure 1-5. The lowest force required for failure was for the sample ground with 600 grit sandpaper. Images from the spalled area (not shown here) indicate that voids formed along the polishing marks. The samples ground with rougher sandpaper (240 grit) showed higher resistance to pull testing. This was attributed to a smaller density of polishing marks which can increase void initiation during oxidation. Surface treatment using 240 grit sandpaper still decreases adhesion of the scale in comparison with untreated samples. It was observed that the samples treated with

* For composition, see Table 1-3

electrochemical polishing developed voids at the metal surface grain boundaries. Acid pickling, however, did not change the force needed for failure. Sandblasting and heat-treating in a reducing atmosphere showed the greatest improvement in terms of scale adhesion. The improvement achieved with sandblasting was attributed to the difficulty for crack propagation along the interface as a result of a tortuous alloy surface shape. Heat-treating in reducing atmospheres is known to remove surface impurities, especially sulphur which reduces adhesion through segregation to the metal/oxide scale interface.

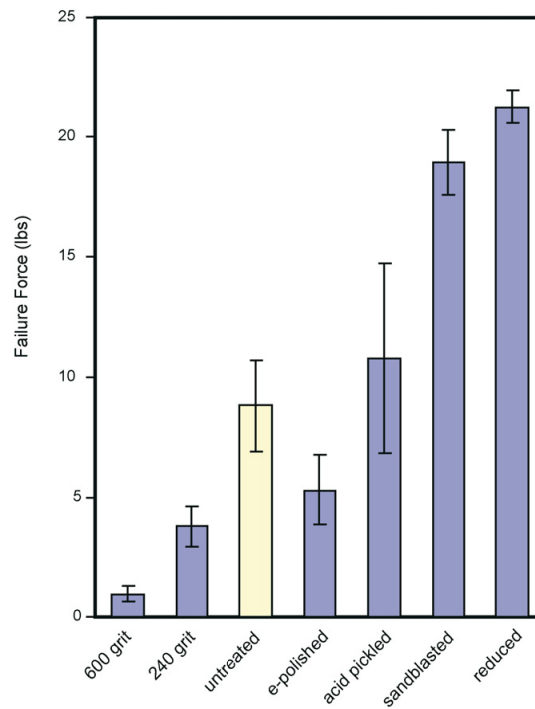


Figure 1-5 The effect of different surface treatments on scale adhesion for AISI-SAE 430 samples treated and oxidized at 800C in air for 458 h [154].

Coating with Y has a similar effect as heat-treating in reducing atmospheres. A combination of a Y-coating and a reducing atmosphere is expected to have the greatest effect on scale adhesion improvement for long oxidation times. Belogolovsky et al. [154] believe that anything that can reduce metal/oxide scale

contact area results in poor adhesion and will also increase the ASR of steel interconnects.

Mechanical and thermo-chemical surface treatments can give rise to promising results in terms of reduced ASR. Nonetheless, the Cr poisoning issue is still a problem and has to be overcome by application of effective coatings such as spinels.

1.4.4 Alloy developments/modifications

Among the numerous types of high-temperature alloys tested in terms of suitability for application as interconnect materials, ferritic stainless steels appear to be the most appropriate choice. In the past, inexpensive commercial grades such as the AISI-SAE 400 series (e.g., 430, 434, 444, etc.) were the mostly utilized steels for SOFC interconnect applications. The ASR of such steels, however, increases rapidly with oxidation and this is attributed to poor scale-to-metal adhesion, segregation of insulating oxides (i.e., silica) at the metal/oxide scale interface and spallation of the scale as the result of interfacial defects combined with thermal stresses. In addition to Si and Al, which may form continuous insulating layers, indigenous impurities such as S and possibly P can dramatically deteriorate oxide scale-to-metal adhesion as these impurities also accumulate at the metal/oxide scale interface. Spallation of alumina and chromia scales is directly related to the presence of trace amounts of S (e.g., ~50 ppm) and its segregation to the metal/oxide scale interface [155-157]. On the other hand, the addition of trace amounts of reactive elements (e.g., La, Y, Ce, Hf, Zr, Ti, etc.) to the alloy can greatly enhance oxide scale-to-metal adhesion [99, 103, 104]. The effect of reactive elements was discussed earlier in this chapter.

To overcome the drawbacks associated with the use of common ferritic stainless steel grades with non-optimal compositions, some specialty alloys have been developed specifically for the purpose of interconnect application. Examples of

newly developed ferritic stainless steels include E-brite, Crofer 22 APU, ZMG232 and ZMG232L*. All these steels contain lower levels of C, S, P, Mn and Si and higher concentrations of Cr in comparison with the typical formerly used steels.

E-brite (UNS 44627, ASTM Type XM-27), which is manufactured by Allegheny Ludlum, contains up to 27 wt.% Cr, 0.025 wt.% Si, 0.02 wt.% S (max.), 0.020 wt.% P (max.) and 0.01 wt.% C (max.) [158]. This alloy does not contain any reactive elements. E-brite is highly oxidation resistant; its specific mass gain is 0.4 mgcm⁻² after 2000 hours of cyclic oxidation (twenty 100-hours) in air at 800°C [159]. The ASR for E-brite is approximately 0.015 Ωcm² at 800°C after 250 hours of oxidation in air [74].

Crofer 22 APU is a specially designed interconnect alloy by ThyssenKrupp [160]. This alloy contains 20-24 wt.% Cr, 0.5 wt.% Si, 0.02 wt.% S (max.), 0.05 wt.% P (max.), 0.03 wt.% C, 0.03-0.2 wt.% Ti and 0.04-0.2 wt.% La. In addition to its relatively low levels of impurities, this alloy contains Ti and La as reactive elements. The manufacturer [160] claims that this steel exhibits a contact resistance an order of magnitude smaller than a traditional AISI-SAE 446 steel at 800°C. The ASR of Crofer 22 APU is approximately 0.01 Ωcm² at 800°C and remains stable for the test period of 600 hours [160]. The specific mass gain of this alloy is 1.25 mgcm⁻² for cyclic oxidation in air at 800°C for 2000 hours (twenty 100-h cycles) [159].

ZMG232 and ZMG232L have been developed for SOFC interconnect purposes by Hitachi Metals. ZMG232 contains 22 wt.% Cr, 0.4 wt.% Si, 0.02 wt.% C, 0.22 wt.% Zr and 0.03-0.08 wt.% La [161]. Indigenous impurities, such as S and P levels, are not reported by the manufacturer. Zirconium and La, as reactive elements, are incorporated into the steel composition. ZMG232L has virtually the same composition as ZMG232 except that this alloy contains lower levels of Si (i.e., 0.1 wt.%). This small Si content difference has a marked effect on oxidation

* For composition, see Table 1-3

resistance of ZMG232(L) steels [161]. The specific mass gain obtained with oxidation in air at 750°C for 2000 hours for ZMG232 is 0.5 mg cm⁻², while that for ZMG232L is approximately 0.35 mg cm⁻² [161]. This difference becomes more notable at higher temperatures (2.5 vs. 1 mg.cm⁻² for oxidation at 1000°C for 100 hours) [161]. For both alloys, the level of Si content, however, does not seem to greatly affect the contact resistance. The ASR value for ZMG232 at 750°C in air after 1000 hours was 0.025 Ωcm², while that for ZMG232L was approximately 0.022 Ωcm² [161]. These values are virtually the same. The ASR for ZMG232 at 800°C after 1500 h of oxidation was 0.05 Ω.cm², while that for AISI-SAE 430 was 0.26 Ωcm² at 800°C after 650 hours. This difference signifies that by properly adjusting the alloy composition, a marked improvement in the electrical conductivity of the steel interconnects can be achieved.

Although improvements are achieved with surface treatment, alloy developments and modifications, coatings still seem to be required due to Cr vaporization and Cr poisoning issues, as all the newly developed alloys are chromia formers. A smart combination of alloy development, surface treatment and coatings can offer a thorough solution to the interconnect problems mentioned above.

1.5 Objectives and motivations

The main objective of this research was to develop novel conductive/protective coatings for commercially used ferritic stainless steel interconnects utilized in SOFCs. Such coatings are expected to improve the high-temperature oxidation resistance and electronic conductivity of the steel substrates. Moreover, coatings must be capable of inhibiting Cr migration to the oxide surface and Cr poisoning. As a novel approach, electrodeposition of composite coatings consisting of embedded, reactive element containing particles in a metal matrix were selected for this research. As explained in previous sections, addition of reactive oxide particles can greatly improve the oxidation resistance and oxide scale-to-metal adhesion of chromia formers. It was also described that electroplating of metals followed by oxidizing in air can successfully form conductive spinel layers which

are also able to inhibit Cr migration to the oxide surface. It is expected that the application of an electrodeposited composite consisting of reactive element containing particles in a metal matrix can exploit the benefits of spinels and reactive element additions. Electrolytes with dispersed particles can be used for composite electrodeposition. Nickel and Co were chosen as the metal matrix due to several rationales. Electrodeposition of Ni and Co is technically easy and inexpensive. Dense, adherent, fine-grained and uniform coatings of Ni or Co on various grades of stainless steels can be achieved. Co-deposition of inert particles with Co and particularly Ni is straightforwardly practical and has been widely studied. Nickel and Co, especially Co, can form conductive oxides and spinel phases upon oxidation in air. Lanthanum chromite was selected as the reactive element containing particle due to its superior stability in acidic electrolytes used for deposition of Ni or Co in comparison with simple reactive oxides. Plain reactive oxides are soluble in acidic electrolytes to some extent and increase the solution pH. This makes the electrodeposition process impractical. The application of such composite coatings for steel interconnects has not been reported in previous literature and is an original approach to solve the interconnect problems.

The second objective of this research work was to investigate the effect of metal-oxide scale interfacial imperfections contributing to degradation of uncoated stainless steels in terms of oxide scale adhesion and conductivity of the steel interconnects. Impurity content and improper steel composition may lead to poor oxidation behavior and oxide scale properties. This issue has not yet been comprehensively addressed in the literature concerning steel interconnects.

1.6 Outline

In addition to the current chapter (Chapter 1), which contains the introduction and literature review and explains the research aims, Chapters 2, 3, 4 and 5 are dedicated to the various portions of the research work and the combination of these compose a unified thesis. The individual chapters are in a journal paper

format comprising an introduction, experimental methods, results and discussion and conclusions. The chapters are combined in a sequence according to the progress of the integrated research.

Chapter 2, which is entitled “Electrodeposition of Ni/LaCrO₃ Composite Coatings for Solid Oxide Fuel Cell Stainless Steel Interconnect Applications”, evaluates the effect of deposition parameters on the volume fraction of particles embedded in the Ni matrix. The material in this chapter has been published in the Journal of the Electrochemical Society (N. Shaigan, D. G. Ivey and W. X. Chen, *Journal of the Electrochemical Society*, **155**, D278 (2008)). In summary, it was found that by adjusting the deposition parameters, up to 35 vol.% of particles can be co-deposited with Ni from a Watts Ni plating bath with a horizontally placed cathode. The optimum conditions to maximize the particle volume fraction in the coating are a current density of 40–50 mAcm⁻², 20 g/L particle loading in the bath, pH 4 and suspension of particles in the plating bath by means of an overhead impeller.

Continuing the study presented in Chapter 2, Chapter 3 of this thesis deals with long-term oxidation behavior, oxide scale characterization and electronic properties of Ni/LaCrO₃ coatings. The chapter title is “Oxidation and Electrical Behavior of Nickel/Lanthanum Chromite-coated Stainless Steel Interconnects”. A version of this work has been published in the Journal of Power Sources (N. Shaigan, D. G. Ivey and W. X. Chen, *Journal of Power Sources*, **183**, 651 (2008)). The substrate used in this study was AISI-SAE 430 stainless steel. The oxidation tests were performed at 800 °C in air for up to 2040 h. It was observed that the scale is a double layer consisting of a particle filled chromia-rich subscale and an outer Ni/Fe-rich spinel together with NiO particles. The addition of LaCrO₃ particles greatly enhances the high-temperature oxidation resistance of Ni-coated ferritic stainless steels. An excellent, stable ASR values (0.005 Ω cm² after 400 h) was achieved with the application of

Ni/LaCrO₃ coatings. The coatings proved highly effective in adsorbing the migrating Cr species to the oxide scale surface.

In the work presented in Chapter 4, Ni was replaced with Co in the metal-matrix composite coating due to the high conductivity of Co containing spinels. The title for this chapter is “Co/LaCrO₃ Composite Coatings for AISI 430 Stainless Steel Solid Oxide Fuel Cell Interconnects”. An alternative version of this study has been published in the Journal of Power Sources (N. Shaigan, D. G. Ivey and W. X. Chen, *Journal of Power Sources*, **185**, 331 (2008)). The results obtained from this work showed that the Co/LaCrO₃ coating forms a triple-layer scale consisting of a chromia-rich subscale, a Co–Fe spinel mid-layer and a Co₃O₄ spinel top layer after annealing at 800°C in air. This scale is protective, acts as an effective barrier against chromium migration into the outer oxide layer and exhibits a low, stable ASR of approximately 0.02 Ω cm² after 900 h at 800 °C in air. The presence of La containing LaCrO₃ particles leads to improvement of high temperature oxidation resistance and prevents spallation and breakaway oxidation behaviour.

During implementation of the oxidation tests described earlier, it was found that AISI-SAE 430 steels used as substrates in all studies included in this thesis undergo severe spallation upon air-cooling from the furnace temperature. In order to investigate the reasons resulting in oxide spallation for uncoated substrates, part of this thesis was devoted to study of metal-oxide scale interfacial imperfections. The title of Chapter 5 is “Metal-Oxide Scale Interfacial Imperfections and Performance of Stainless Steel Interconnects Utilized in Solid Oxide Fuel Cells”. This work has been published in the Journal of the Electrochemical Society (N. Shaigan, D. G. Ivey and W. X. Chen, *Journal of the Electrochemical Society*, **156**, B765-B770 (2009)). In brief, two types of stainless steels, AISI-SAE 430 and Hitachi ZMG232, were selected for experiments. AISI-SAE 430 is a low-cost commercial grade containing non-metallic impurities, such as S and P; while ZMG232 is a specialty grade, developed specifically for interconnect applications. This steel contains small amounts of Zr and La as reactive elements. Electron

microscopy as well as surface science analysis techniques were used to study the metal-oxide scale interface. Interfacial void formation and segregation of S, Cl, N, Pb, V and Al were observed for AISI-SAE 430 steel samples. No pronounced segregation of impurities or spallation of the oxide scale occurred for ZMG232, which contains reactive elements and lower amounts of impurities.

The Chapter 6 provides general conclusions and recommendations for future research. The Appendix provided at the end of the thesis explains the preliminary proposal and experiments. Some of those early works were unsuccessful and abandoned. However, the original ideas and results were the basis of the subsequent successful, published work in this thesis and, therefore, are discussed in the Appendix.

Table 1-3 Nominal chemical composition of the steels mentioned in the text*.

Steel	Cr	Mn	Si	Al	Ni	Mo	La	Zr	Cu	Ti	Nb	C	S	P
AISI-SAE 430	16-18	1	1	-	-	-	-	-	-	-	-	0.12	0.03	0.04
AISI-SAE 434	19	1	1	-	-	2	-	-	-	-	0.35	0.12	0.03	0.04
AISI-SAE 446	23-27	1.5	1	-	-	-	-	-	-	-	-	0.2	0.03	0.04
E-brite ^a	26- 27.5	0.4	0.4	-	0.5	0.75	-	-	0.2	-	0.2	0.01	0.02	0.02
Crofer 22	20-24	0.3-	0.5	0.5	-	-	0.04-	-	0.5	0.03-	-	0.03	0.02	0.05
APU ^b		0.8					0.2			0.2				
AL453 ^a	22.0	0.3	0.08	0.6	-	-	0.1	-	-	0.02	-	0.03	0.03	0.02
ZMG232 ^c	22.0	0.5	0.4	0.22	0.26	-	0.04	0.22	-	-	-	0.02	-	-
ZMG232L ^c	22.04	0.45	0.1	0.03	0.33	-	0.08	0.2	-	-	-	-	-	-
F18TNb ^d	17.8	0.5	0.5	-	-	-	-	-	-	0.3	0.4	0.02		
F17TNb ^d	17.5	0.5	0.5	-	-	-	-	-	-			0.02	-	-
IT-11 ^e	26.4	-	0.01	0.02	-	-	-	-	-	-	-	0.009	-	-

* The balance is Fe; steels may also contain trace amounts of N

^a A trade mark of Allegheny Ludlum

^b A trade mark of ThyssenKrupp

^c A trade mark of Hitachi Metals

^d A trade mark of Ugine Arcelor, Isbergues, France

^e A trade mark of Plansee AG, Reutte, Austria

1.7 References

1. E. Chen, Fuel Cell Technology Handbook, in, G. Hoogers Editor, CRC Press, Boca Raton, London, New York, Washington, D.C (2003).
2. M. C. Williams, Fuel Cell Handbook, in, 5 ed., EG&G Services, Parsons, Inc., Morgantow (2000).
3. M. C. Williams, in *ASM Handbook, Corrosion: Fundamentals, Testing, and Protection*, J. Stephen D. Cramer and Bernard S. Covino Editor, ASM International, Materials Park, OH (2003).
4. N. Q. Minh, *Journal of the American Ceramic Society*, **76**, 563 (1993).
5. N. Q. Minh, *Solid State Ionics*, **174**, 271 (2004).
6. W. Z. Zhu and S. C. Deevi, *Materials Research Bulletin*, **38**, 957 (2003).
7. W. Z. Zhu and S. C. Deevi, *Materials Science and Engineering*, **A348**, 227 (2003).
8. Z. Yang, *International Materials Review*, **53**, 39 (2008).

9. K. Huang, P. Y. Hou and J. B. Goodenough, *Solid States Ionics*, **129**, 237 (2000).
10. Z. Yang, M. S. Walker, P. Singh, J. W. Stevenson and T. Norby, *Journal of The Electrochemical Society*, **151**, B669 (2004).
11. J. Brouwer in *Distributed Generation: The Power Paradigm for the New Millennium, Fuel Cells*, A.-M. Borbely and J. F. Kreider Editors, CRC Press LLC, Boca Raton, London, New York, Washington, D.C. (2001).
12. P. Singh and N. Q. Minh, *International Journal of Applied Ceramic Technology*, **1**, 5 (2004).
13. J. H. Zhu, Y. Zhang, A. Basu, Z. G. Lu, M. Paranthaman, D. F. Lee and E. A. Payzant, *Surface and Coatings Technology*, **177-178**, 65 (2004).
14. K. Kendall, *International Materials Reviews*, **50**, 257 (2005).
15. Z. Yang, K. S. Weil, D. M. Paxton and J. W. Stevenson, *Journal of The Electrochemical Society*, **150**, A1188 (2003).
16. J. W. Fergus, *Solid State Ionics*, **171**, 1 (2004).
17. S. W. Paulik, S. Baskaran and T. R. Armstrong, *Journal of Materials Science*, **33**, 2397 (1998).
18. R. E. Williford, T. R. Armstrong and J. D. Gale, *Journal of Solid State Chemistry*, **149**, 320 (2000).
19. L. Mikkelsen, N. Pryds and P. V. Hendriksen, *Thin Solid Films*, **515**, 6537 (2007).
20. G. Y. Lee, R. H. Song, J. H. Kim, D. H. Peck, T. H. Lim, Y. G. Shul and D. R. Shin, *Journal of Electroceramics*, **17**, 723 (2006).
21. W. J. Quadackers, J. Piron-Abellan, V. Shemet and L. Singheiser, *Materials at High Temperatures*, **20**, 115 (2003).
22. Z. G. Yang, *International Materials Reviews*, **53**, 39 (2008).
23. Z. G. Yang, M. S. Walker, P. Singh, J. W. Stevenson and T. Norby, *Journal of The Electrochemical Society*, **151**, B669 (2004).
24. W. Qu, L. Jian, D. G. Ivey and J. M. Hill, *Journal of Power Sources*, **157**, 335 (2006).

25. K. Huang, P. Y. Hou and J. B. Goodenough, *Materials Research Bulletin*, **36**, 81 (2001).
26. S. C. Paulson and V. I. Birss, *Journal of The Electrochemical Society*, **151**, A1961 (2004).
27. Y. Matsuzaki and I. Yasuda, *Solid State Ionics*, **132**, 271 (2000).
28. Y. Matsuzaki and I. Yasuda, *Journal of The Electrochemical Society*, **148**, A126 (2001).
29. E. Konyshева, H. Penkalla, E. Wessel, J. Mertens, U. Seeling, L. Singheiser and K. Hilpert, *Journal of The Electrochemical Society*, **153**, A765 (2006).
30. H. Yokokawa, T. Horita, N. Sakai, K. Yamaji, M. E. Brito, Y. P. Xiong and H. Kishimoto, *Solid State Ionics*, **177**, 3193 (2006).
31. J. W. Fergus, *International Journal of Hydrogen Energy*, **32**, 3664 (2007).
32. X. B. Chen, L. Zhang and S. P. Jiang, *Journal of The Electrochemical Society*, **155**, B1093 (2008).
33. J. W. Fergus, *Materials Science and Engineering a-Structural Materials Properties Microstructure and Processing*, **397**, 271 (2005).
34. Z. G. Yang, K. S. Weil, D. M. Paxton and J. W. Stevenson, *Journal of The Electrochemical Society*, **150**, A1188 (2003).
35. B. Hua, J. Pu, J. F. Zhang, F. S. Lu, B. Chi and L. Jian, *Journal of the Electrochemical Society*, **156**, B93 (2009).
36. S. Elangovan, S. Balagopal, U. Timper, L. Bay, D. Larsen and J. Hartvigsen, *Journal of Materials Engineering and Performance*, **13**, 265 (2004).
37. S. Elangovan, J. Hartvigsen, R. Lashway, S. Balagopal and I. Bay, *Transactions of the Indian Institute of Metals*, **57**, 311 (2004).
38. I. Saeki, H. Konno and R. Furuichi, *Corrosion Science*, **38**, 19 (1996).
39. Z. G. Yang, M. S. Walker, P. Singh and J. W. Stevenson, *Electrochemical and Solid State Letters*, **6**, B35 (2003).
40. Z. G. Yang, G. G. Xia, C. M. Wang, Z. M. Nie, J. Templeton, J. W. Stevenson and P. Singh, *Journal of Power Sources*, **183**, 660 (2008).

41. R. A. Lula in *Stainless Steels*, American Society for Metals, Metals Park, Ohio (1986).
42. H. Okamoto in *Alloy Phase Diagrams*, ASM International, Metals Park, Ohio (1990).
43. L. Cooper, S. Benhaddad, A. Wood and D. G. Ivey, *Journal of Power Sources*, **184**, 220 (2008).
44. I. Saeki, H. Konno and R. Furuichi, *Corrosion Science*, **38**, 1595 (1996).
45. P. Huczowski, N. Christiansen, V. Shemet, L. Niewolak, J. Piron-Abellan, L. Singheiser and W. J. Quadackers, *Fuel Cells*, **6**, 93 (2006).
46. Atkinson and R. I. Taylor, in *Transport in Non-Stoichiometric Compounds*, V.S. Stubican and G. Simkovich, Plenum, New York (1985)
47. Y. Saito and B. Onay, *Surface & Coatings Technology*, **43-4**, 336 (1990).
48. W. Qu, L. Jian, J. M. Hill and D. G. Ivey, *Journal of Power Sources*, **153**, 114 (2006).
49. W. Qu, H. Li and D. G. Ivey, *Journal of Power Sources*, **138**, 162 (2004).
50. J. H. Zhu, Y. Zhang, A. Basu, Z. G. Lu, M. Paranthaman, D. F. Lee and E. A. Payzant, *Surface & Coatings Technology*, **177**, 65 (2004).
51. L. Mikkelsen, N. Pryds and P. V. Hendriksen, *Thin Solid Films*, **515**, 6537 (2007).
52. C. J. Fu, K. N. Sun, X. B. Chen, N. Q. Zhang and D. R. Zhou, *Corrosion Science*, **50**, 1926 (2008).
53. C. J. Fu, K. N. Sun, N. Q. Zhang, X. B. Chen and D. R. Zhou, *Thin Solid Films*, **516**, 1857 (2008).
54. C. J. Fu, K. N. Sun, N. Q. Zhang and D. R. Zhou, *Rare Metal Materials and Engineering*, **35**, 1117 (2006).
55. C. J. Li, C. X. Li, H. G. Long, Y. Z. Xing and G. J. Yang, *Solid State Ionics*, **179**, 1575 (2008).
56. C. J. Li, C. X. Li, Y. Z. Xing, M. Gao and G. J. Yang, *Solid State Ionics*, **177**, 2065 (2006).
57. C. X. Li, M. Gao, C. J. Li, W. Zhou, G. J. Yang and Y. Y. Wang, *Materials Transactions*, **47**, 1654 (2006).

58. C. X. Li, Y. X. Xie, C. J. Li and G. J. Yang, *Journal of Power Sources*, **184**, 370 (2008).
59. D. P. Lim, D. S. Lim, J. S. Oh and I. W. Lyo, *Surface and coatings Technology*, **200**, 1248 (2005).
60. H. W. Nie, T. Wen and H. Y. Tu, *Materials Research Bulletin*, **38**, 1531 (2003).
61. Y. Z. Xing, C. J. Li, C. X. Li and G. J. Yang, *Journal of Power Sources*, **176**, 31 (2008).
62. J. H. Kim, R. H. Song and S. H. Hyun, *Solid State Ionics*, **174**, 185 (2004).
63. J. S. Kim, H. K. Yang, T. W. Eom, H. H. Yoon and S. J. Park, *Molecular Crystals and Liquid Crystals*, **472**, 669 (2007).
64. F. Smeacetto, M. Salvo, A. Ferraris, V. Casalegno, P. Asinari and A. Chrysanthou, *Journal of the European Ceramic Society*, **28**, 2521 (2008).
65. Z. G. Yang, G. G. Xia, X. H. Li and J. W. Stevenson, *International Journal of Hydrogen Energy*, **32**, 3648 (2007).
66. M. F. Chi, N. Browning and N. Orlovskaya, *Journal of Solid State Electrochemistry*, **10**, 659 (2006).
67. C. L. Chu, J. Y. Wang and S. Y. Lee, *International Journal of Hydrogen Energy*, **33**, 2536 (2008).
68. D. J. Jan, C. T. Lin and C. F. Ai, *Thin Solid Films*, **516**, 6300 (2008).
69. C. Johnson, R. Gemmen and N. Orlovskaya, *Composites Part B-Engineering*, **35**, 167 (2004).
70. A. Kayani, T. L. Buchanan, M. Kopczyk, C. Collins, J. Lucas, K. Lund, R. Hutchison, P. E. Gannon, M. C. Deibert, R. J. Smith, D. S. Choi and V. I. Gorokhovskiy, *Surface & Coatings Technology*, **201**, 4460 (2006).
71. C. Lee and J. Bae, *Thin Solid Films*, **516**, 6432 (2008).
72. N. Orlovskaya, A. Coratolo, C. Johnson and R. Gemmen, *Journal of the American Ceramic Society*, **87**, 1981 (2004).
73. J. W. Wu, C. M. Li, C. Johnson and X. B. Liu, *Journal of Power Sources*, **175**, 833 (2008).

74. Z. G. Yang, G. G. Xia, G. D. Maupin and J. W. Stevenson, *Journal of The Electrochemical Society*, **153**, A1852 (2006).
75. M. Stanislawski, J. Froitzheim, L. Niewolak, W. J. Quadackers, K. Hilpert, T. Markus and L. Singheiser, *Journal of Power Sources*, **164**, 578 (2007).
76. P. E. Gannon, V. I. Gorokhovsky, M. C. Deibert, R. J. Smith, A. Kayani, P. T. White, S. Sofie, Z. Yang, D. McCready, S. Visco, C. Jacobson and H. Kurokawa, *International Journal of Hydrogen Energy*, **32**, 3672 (2007).
77. V. I. Gorokhovsky, P. E. Gannon, M. C. Deibert, R. J. Smith, A. Kayani, M. Kopczyk, D. VanVorous, Z. G. Yang, J. W. Stevenson, S. Visco, C. Jacobson, H. Kurokawa and S. W. Sofie, *Journal of the Electrochemical Society*, **153**, A1886 (2006).
78. A. Kayani, R. J. Smith, S. Teintze, M. Kopczyk, P. E. Gannon, M. C. Deibert, V. I. Gorokhovsky and V. Shutthanandan, *Surface & Coatings Technology*, **201**, 1685 (2006).
79. M. R. Bateni, P. Wei, X. H. Deng and A. Petric, *Surface & Coatings Technology*, **201**, 4677 (2007).
80. W. F. Wei, W. Chen and D. G. Ivey, *Chemistry of Materials*, **19**, 2816 (2007).
81. W. F. Wei, W. X. Chen and D. G. Ivey, *Journal of Physical Chemistry C*, **111**, 10398 (2007).
82. W. F. Wei, W. X. Chen and D. G. Ivey, *Chemistry of Materials*, **20**, 1941 (2008).
83. X. Montero, N. Jordan, J. Piron-Abellan, F. Tietz, D. Stover, M. Cassir and I. Villarreal, *Journal of The Electrochemical Society*, **156**, B188 (2009).
84. N. Oishi, T. Namikawa and Y. Yamazaki, *Surface & Coatings Technology*, **132**, 58 (2000).
85. Z. G. Yang, G. G. Xia, S. P. Simner and J. W. Stevenson, *Journal of The Electrochemical Society*, **152**, A1896 (2005).

86. M. Bertoldi, T. Zandonella, D. Montinaro, V. M. Sglavo, A. Fossati, A. Lavacchi, C. Giolli and U. Bardi, *Journal of Fuel Cell Science and Technology*, **5** (2008).
87. Z. G. Yang, G. G. Xia, G. D. Maupin and J. W. Stevenson, *Surface & Coatings Technology*, **201**, 4476 (2006).
88. Z. G. Yang, G. G. Xia, Z. M. Nie, J. Templeton and J. W. Stevenson, *Electrochemical and Solid State Letters*, **11**, B140 (2008).
89. Z. G. Yang, G. G. Xia and J. W. Stevenson, *Electrochemical and Solid State Letters*, **8**, A168 (2005).
90. P. Wei, X. Deng, M. R. Bateni and A. Petric, *Corrosion*, **63**, 529 (2007).
91. X. Montero, F. Tietz, D. Sebold, H. R. Buchkremer, A. Ringuede, M. Cassir, A. Laresgoiti and I. Villarreal, *Journal of Power Sources*, **184**, 172 (2008).
92. X. H. Deng, P. Wei, M. R. Bateni and A. Petric, *Journal of Power Sources*, **160**, 1225 (2006).
93. M. J. Garcia-Vargas, M. Zahid, F. Tietz and A. Aslanides, in *10th International Symposium on Solid Oxide Fuel Cells, SOFC-X*, p. 2399, ECS Transactions, Japan (2007).
94. J. W. Wu, Y. L. Jiang, C. Johnson and X. B. Liu, *Journal of Power Sources*, **177**, 376 (2008).
95. X. Chen, P. Y. Hou, C. P. Jacobson, S. J. Visco and L. C. De Jonghe, *Solid State Ionics*, **176**, 425 (2005).
96. Z. G. Yang, J. S. Hardy, M. S. Walker, G. G. Xia, S. P. Simner and J. W. Stevenson, *Journal of the Electrochemical Society*, **151**, A1825 (2004).
97. J. Wu, C. D. Johnsona, Y. Jianga, R. S. Gemmena and X. Liu, *Electrochimica Acta*, **54**, 793 (2008).
98. W. Wei, W. Chen and D. G. Ivey, *Journal of Power Sources*, **In press** (2008).
99. I. M. Allam, D. P. Whittle and J. Stringer, *Oxidation of Metals*, **12**, 35 (1978).

100. O. T. Goncel, D. P. Whittle and J. Stringer, *Oxidation of Metals*, **15**, 287 (1981).
101. B. A. Pint, *Materials Science Forum*, **251-4**, 397 (1997).
102. J. Stringer, I. M. Allam and D. P. Whittle, *Thin Solid Films*, **45**, 377 (1977).
103. D. P. Whittle and J. Stringer, *Philosophical Transactions of the Royal Society of London Series a-Mathematical Physical and Engineering Sciences*, **295**, 309 (1980).
104. B. A. Pint, *Oxidation of Metals*, **45**, 1 (1996).
105. B. A. Pint, *Journal of the American Ceramic Society*, **86**, 686 (2003).
106. B. A. Pint and L. W. Hobbs, *Oxidation of Metals*, **61**, 273 (2004).
107. B. A. Pint, K. L. More and I. G. Wright, *Materials at High Temperatures*, **20**, 375 (2003).
108. B. A. Pint and J. H. Schneibel, *Scripta Materialia*, **53**, 379 (2005).
109. B. A. Pint and I. G. Wright, *Oxidation of Metals*, **63**, 193 (2005).
110. H. B. Qi and D. G. Lees, *Oxidation of Metals*, **53**, 507 (2000).
111. H. S. Seo, G. X. Jin, J. H. Jun, D. H. Kim and K. Y. Kim, *Journal of Power Sources*, **178**, 1 (2008).
112. S. Fontana, R. Amendola, S. Chevalier, P. Piccardo, G. Caboche, M. Viviani, R. Molins and M. Sennour, *Journal of Power Sources*, **171**, 652 (2007).
113. E. Martinez, J. Esteve, G. Garcia, A. Figueras and J. Llibre, *Surface & Coatings Technology*, **101**, 164 (1998).
114. P. Piccardo, P. Gannon, S. Chevalier, M. Viviani, A. Barbucci, G. Caboche, R. Amendola and S. Fontana, *Surface & Coatings Technology*, **200**, 1221 (2007).
115. Eisentra.Kj and R. E. Sievers, *Journal of the American Chemical Society*, **87**, 5254 (1965).
116. Eisentra.Kj and R. E. Sievers, *Journal of Inorganic & Nuclear Chemistry*, **29**, 1931 (1967).

117. Schwarbe, D. R. Gere, R. E. Sievers and Eisentra.Kj, *Inorganic Chemistry*, **6**, 1933 (1967).
118. J. E. Sicre, J. T. Dubois, Eisentra.Kj and R. E. Sievers, *Journal of the American Chemical Society*, **91**, 3476 (1969).
119. R. E. Sievers, Eisentra.Kj, C. S. Springer and D. W. Meek, *Advances in Chemistry Series*, 141 (1967).
120. G. Cabouro, G. Caboche, S. Chevalier and R. Piccardo, *Journal of Power Sources*, **156**, 39 (2006).
121. I. Belogolovsky, X. D. Zhou, H. Kurokawa, P. Y. Hou, S. Visco and H. U. Anderson, *Journal of the Electrochemical Society*, **154**, B976 (2007).
122. Z. G. Yang, G. G. Xia, P. Singh and J. W. Stevenson, *Journal of Power Sources*, **155**, 246 (2006).
123. S. L. Rohde in *ASM Handbook, Surface Engineering*, ASM International, Metals Park, Ohio (1994).
124. R. C and J. Tucker in *ASM Handbook Surface Engineering*, ASM International, Metals Park, Ohio (1994).
125. C. J. Fu, K. N. Sun and D. R. Zhou, *Journal of Rare Earths*, **24**, 320 (2006).
126. A. Petric and H. Ling, *Journal of the American Ceramic Society*, **90**, 1515 (2007).
127. L. A. Chick, L. R. Pederson, G. D. Maupin, J. L. Bates, L. E. Thomas and G. J. Exarhos, *Materials Letters*, **10**, 6 (1990).
128. X. L. Chen, Q. Xu, D. P. Huang, F. Zhang and W. Chen, *Journal of Wuhan University of Technology-Materials Science Edition*, **21**, 53 (2006).
129. L. G. Cong, T. M. He, Y. A. Ji, P. F. Guan, Y. L. Huang and W. H. Su, *Journal of Alloys and Compounds*, **348**, 325 (2003).
130. W. F. Guo, Q. Xu, W. Chen, D. P. Huang, H. Wang and R. Z. Yuan, *Rare Metal Materials and Engineering*, **34**, 1886 (2005).
131. T. M. He, Q. He and N. Wang, *Journal of Alloys and Compounds*, **396**, 309 (2005).

132. D. P. Huang, Q. Xu, W. Chen, H. Wang and R. Z. Yuan, *Journal of Inorganic Materials*, **18**, 1039 (2003).
133. S. G. Huang, C. R. Xia, X. B. Zhang and G. Y. Meng, *Rare Metal Materials and Engineering*, **34**, 1650 (2005).
134. Y. Ji, J. Liu, T. M. He, L. G. Cong, J. X. Wang and W. H. Su, *Journal of Alloys and Compounds*, **353**, 257 (2003).
135. Z. Lei, Q. S. Zhu and S. C. Zhang, *Journal of the European Ceramic Society*, **26**, 397 (2006).
136. B. W. Liu and Y. Zhang, *Journal of Alloys and Compounds*, **453**, 418 (2008).
137. R. H. Liu, Q. S. Du, W. H. Ma, H. Wang, B. Yang, Y. N. Dai and X. J. Ma, *Journal of Rare Earths*, **24**, 98 (2006).
138. Z. H. Liu, X. F. Guan, J. Zhan and H. P. Zhou, *Rare Metal Materials and Engineering*, **36**, 616 (2007).
139. D. Markovic, V. Kusigerski, M. Tadic, J. Blanusa, M. V. Antisari and V. Spasojevic, *Scripta Materialia*, **59**, 35 (2008).
140. I. S. Park, S. J. Kim, B. H. Lee and S. Park, *Japanese Journal of Applied Physics Part 1-Regular Papers Short Notes & Review Papers*, **36**, 6426 (1997).
141. R. Peng, X. Fan, Z. Jiang and C. Xia, *Fuel Cells*, **6**, 455 (2006).
142. M. Shi, N. Liu, Y. D. Xu, Y. P. Yuan, P. Majewski and F. Aldinger, *Journal of Alloys and Compounds*, **425**, 348 (2006).
143. H. C. Shin, K. R. Lee, S. Park, C. H. Jung and S. J. Kim, *Japanese Journal of Applied Physics Part 2-Letters*, **35**, L996 (1996).
144. M. Valefi, C. Falamaki, T. Ebadzadeh and M. S. Hashjin, *Journal of the American Ceramic Society*, **90**, 2008 (2007).
145. Q. G. Wang, R. R. Peng, C. R. Xia, W. Zhu and H. T. Wang, *Ceramics International*, **34**, 1773 (2008).
146. S. Yang, T. M. He and Q. He, *Journal of Alloys and Compounds*, **450**, 400 (2008).

147. Y. J. Yang, T. L. Wen, H. Y. Tu, D. Q. Wang and J. H. Yang, *Solid State Ionics*, **135**, 475 (2000).
148. S. B. Boskovic, B. Z. Matovic, M. D. Vljajic and V. D. Kristic, *Ceramics International*, **33**, 89 (2007).
149. H. Kurokawa, C. P. Jacobson, L. C. DeJonghe and S. J. Visco, *Solid State Ionics*, **178**, 287 (2007).
150. D. Lee, I. Lee, Y. Jeon and R. Song, *Solid State Ionics*, **176**, 1021 (2005).
151. G. Y. Zhu, X. H. Fang, C. R. Xia and X. Q. Liu, *Ceramics International*, **31**, 115 (2005).
152. L. Cooper, MSc Thesis, University of Alberta, Edmonton (2007).
153. C. Ostwald and H. J. Grabke, *Corrosion Science*, **46**, 1113 (2004).
154. I. Belogolovsky, P. Y. Hou, C. P. Jacobson and S. J. Visco, *Journal of Power Sources*, **182**, 259 (2008).
155. B. A. Pint, *Oxidation of Metals*, **48**, 303 (1997).
156. D. G. Lees, *Proceedings of the Royal Society of London Series a-Mathematical Physical and Engineering Sciences*, **459**, 1459 (2003).
157. P. Fox, D. G. Lees and G. W. Lorimer, *Oxidation of Metals*, **36**, 491 (1991).
158. Z. G. Yang, G. G. Xia, X. H. Li and J. W. Stevenson, *International Journal of Hydrogen Energy*, **32**, 3648 (2007).
159. S. J. Geng and J. H. Zhu, *Journal of Power Sources*, **160**, 1009 (2006).
160. Crofer 22 APU Material Data Sheet No. 4046, in, ThyssenKrupp VDM GmbH (2005).
161. A. Toji and T. Uehara, Stability of Oxidation Resistance of Ferritic Fe-Cr Alloy for SOFC Interconnects, in *10th International Symposium on Solid Oxide Fuel Cells (SOFC-X)*, K. Eguchi, J. Mizusaki, S. Singhal and H. Yokokawa Editors, p. 2117, The Electrochemical Society, Nara, Japan (2007).

2 Electrodeposition of Ni/LaCrO₃ Composite Coatings for Solid Oxide Fuel Cell Stainless Steel Interconnect Applications

2.1 Introduction

As previously discussed in Chapter 1, in intermediate temperature solid oxide fuel cells (SOFCs), ferritic stainless steels are being considered for use as interconnects. The main advantage of ferritic stainless steels is their compatibility with other cell components in terms of the coefficient of thermal expansion (CTE) [1-4]. However, due to the relatively high operating temperatures (e.g., 750-850°C) of SOFCs and the presence of oxygen on the cathode side, a double layer oxide consisting of chromia and Cr-Mn spinel forms on the surface of the stainless steel interconnects. Such an oxide layer, which has a relatively poor area specific resistance (ASR), grows quite rapidly. Thus, the lifetime of the cell stack is reduced.

Numerous coating systems have been developed to decrease the oxide growth rate and/or increase the scale conductivity. The coating systems are described in detail in Chapter 1. Among various coatings, conductive spinels exhibit superior conductivity/protection properties. It was also discussed in Chapter 1 that electrodeposition of metal and alloys followed by heat-treatment/oxidation is advantageous over other spinel coating techniques in terms of adhesion to the substrate and less porosity in the spinel layer. It was also discussed that addition of reactive oxide particles significantly enhances the oxidation resistance and oxide scale-to-metal adhesion of chromia forming alloys. It is anticipated that the application of an electrodeposited composite consisting of reactive element containing particles in a metal matrix improves the conductivity/protection properties of spinels obtained via conventional electrodeposition of metals followed by high-temperature oxidation.

For this purpose, a method for electrodeposition of composite coatings consisting of reactive element ceramic particles, LaCrO_3 , embedded in a Ni matrix has been successfully developed, studied and optimized. LaCrO_3 was chosen for the particles, due to its good chemical stability in acidic/neutral electrolytes. Also, LaCrO_3 particles are reasonably conductive (the resistivity is $\sim 10 \text{ } \Omega\text{cm}$ for undoped LaCrO_3 [5, 6] and $\sim 0.01 \text{ } \Omega\text{cm}$ for LaCrO_3 doped with 16 at% Sr at 800°C [6]). Therefore, Inclusion of such conductive particles in the coating may increase the conductivity of the scale which forms upon oxidation of the composite coating. In other words, a portion of the oxide scale volume will consist of conductive particles acting as small conductors with negligible resistivity. Nickel was selected owing to its ease of electrodeposition, relatively good oxidation resistance of Ni alloys [7, 8], relative good conductivity for NiO (its resistivity is $\sim 7 \text{ } \Omega\text{cm}$ at 800°C [2]), ability of Ni to form conductive spinels when combined with substrate elements and compatibility with the stainless steel substrate, i.e., Ni forms solid solutions with the steel components (no intermetallic form at high temperatures).

The objective of this portion of the study was to evaluate the effect of critical co-deposition parameters, such as particle loading in the bath, deposition current density, solution pH and electrolyte hydrodynamics, on the volume fraction of particles embedded in the coatings. The oxidation behavior and electrical properties of Ni/ LaCrO_3 coatings will be discussed in Chapter 3.

2.2 Experimental Methods

A conventional Watts nickel plating bath, containing suspended LaCrO_3 particles was used to electroplate the composite layer. An SEM image of the original particles is presented in Figure 2-1 and the particle size distribution is shown in Figure 2-2. Particle size distribution was analyzed with a Mastersizer 2000 from Malvern Instruments Inc. There is a bimodal distribution with average sizes of $\sim 120 \text{ nm}$ and $650\text{-}700 \text{ nm}$. Particles were dispersed in the electrolyte using 60

minutes of ultrasonic agitation followed by 24 hours of magnetic stirring. This procedure was performed to achieve the optimal dispersion degree for particles in the electrolyte and avoid formation of agglomerates. The composition and operating conditions of this bath are listed in Table 2-1. The cathode and anode were placed horizontally in a 300 mL beaker. Coupons of AISI-SAE 430 (UNS 43000) stainless steel, measuring 10mm × 20mm × 1mm, were used as the cathode substrates. Ultrasonic, alkaline cleaning in a 5 g/L NaOH solution containing 1 g/L sodium dodecyl sulfate (SDS), as the wetting agent, was performed and followed by deionized water rinse immediately before activation and electrodeposition. Activation and strike Ni plating were performed for all specimens. Anodic activation, followed by cathodic strike Ni plating, was performed according to ASTM B254-92 (2004) Practice 7.6.1 [9] (Table 2-2), in order to remove and prevent the reformation of the chromium oxide surface passive layer which inhibits electrodeposition. All specimens were cleaned ultrasonically in water for 5 minutes after plating in order to remove loosely adsorbed particles from the surface.

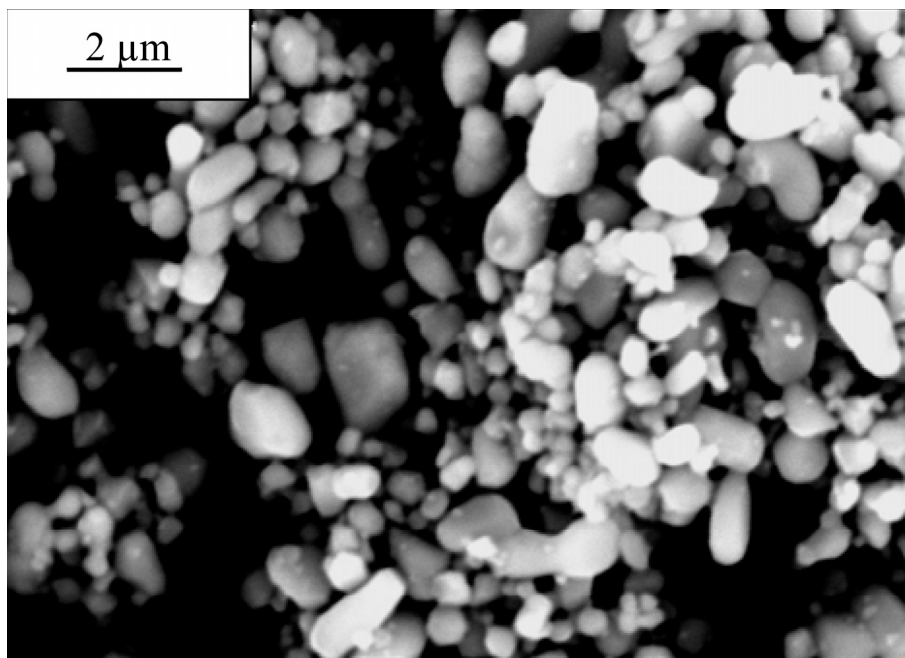


Figure 2-1 SEM image of LaCrO₃ powder used for Ni/LaCrO₃ composite coating

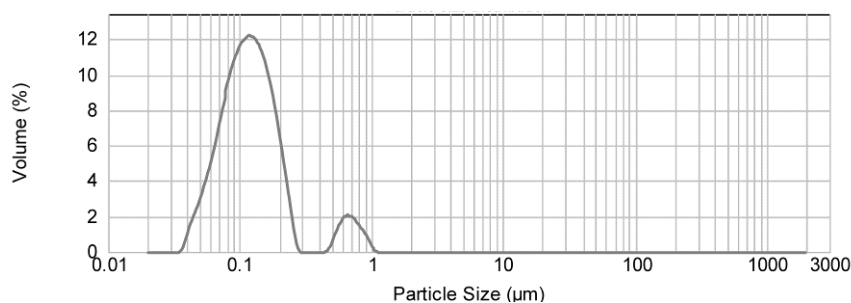


Figure 2-2 Particle size distribution for LaCrO₃ particles.

In order to prepare cross sectional samples for imaging, specimen surfaces were covered with curable epoxy resin and cured in vacuum for 2 hours at 90 °C. Subsequently, the covered samples were mounted in cylindrical Teflon molds with cold, two-part epoxy (resin and hardener). The molds were placed in vacuum for two hours to remove dissolved air and avoid bubbles. Then, they were exposed to air for another 22 hours. Conventional grinding and polishing methods were used for cross sectional sample preparation. Grinding started with 240 grit paper and continued with 320, 400, 600, 800 and 1200 grit abrasive papers. The grinding direction was parallel to the sample length in order to avoid possible damage to coating/oxide-substrate interface. Afterwards, samples were polished with a rotating disc covered with polishing cloths. Diamond pastes with 6 μm and 1 μm particle size were used consecutively for initial polishing. The final polishing was performed with 0.05 μm silica suspension. A Hitachi H2700 SEM equipped with a Princeton Gamma-Tech (Prism IG) ultra thin window (UTW) energy dispersive X-ray (EDX) spectrometer, as well as optical microscopy, were used for imaging and chemical analysis. For imaging the working distance (WD) was 17 mm and the accelerating voltage was 25 kV. The optical microscope used was a DM 2500M Leica. Image analysis software, Image-Pro[®] Version 6, was used to determine the volume fraction of the particles embedded in the coatings. Three separate images for each sample were used for this purpose.

Atomic absorption spectroscopy (AAS) (Varian 220FS Double Beam System) was used to determine the amount of Ni ions adsorbed on LaCrO₃ particles.

Solutions containing 0.01M Ni as sulphate and all other constituents listed in Table 2-1 (except for NiCl₂.6H₂O), at pH values of 2, 2.5, 3, 3.5, 4, 4.5 and 5, were prepared and mixed with 20 g/L of LaCrO₃ particles and stirred for 24 hours. The suspensions were then centrifuged to separate the solution from the particles. The concentration of Ni ions in clear solutions was measured by AAS and subtracted from the initial Ni concentration and divided by the initial Ni concentration to determine the fraction of Ni ions adsorbed on particles. A similar solution containing no particles was used as a reference to determine the initial Ni concentration.

Table 2-1 Composition and operating conditions for Ni/LaCrO₃ composite electroplating bath

Nickel sulfate, hexahydrate (NiSO ₄ .6H ₂ O)	240 g/L (0.9 M)
Nickel chloride, hexahydrate (NiCl ₂ .6H ₂ O)	50 (0.2 M)
Boric acid (H ₃ BO ₄)	40 (0.6 M)
Coumarin (C ₉ H ₆ O ₂)	0.1 (0.7 mM)
Sodium dodecyl sulfate (SDS) (NaC ₁₂ H ₂₅ SO ₄)	0.1 (0.3 mM)
Lanthanum chromite (LaCrO ₃),	20 g/L
Temperature	60±2 °C
pH	~4, (adjusted with NaOH and/or H ₂ SO ₄); unless otherwise specified
Agitation	Magnetic bar from the bottom (400 rpm); unless otherwise specified
Current Density	40 mA/cm ² , DC; unless otherwise specified
Anode	Commercially pure Ni

Table 2-2 Composition and operating conditions of activation/Ni strike plating prior to composite electroplating [9]

Nickel sulfate, hexahydrate (NiSO ₄ .6H ₂ O)	240 g/L (0.9 M)
Hydrochloric acid (HCl, 37 vol%)	85 mL/L (1)
Anodic activation	2 minutes, 22 mA/cm ²
Cathodic nickel strike	6 minutes, 22 mA/cm ²
Temperature	20 °C
Anode	Commercially pure Ni

The zeta potential of the LaCrO₃ particles was measured by means of a Brookhaven (Zeta Plus) zeta potential analyzer. The solutions used for this purpose contained 0.1 g/L of LaCrO₃, 0.01M Ni as sulphate and all other electrolyte constituents listed in Table I (except for NiCl₂.6H₂O), at pH values of 2, 2.5, 3, 3.5, 4, 4.5 and 5.

2.3 Results and Discussion

2.3.1 Coating structure and particle distribution

The structure and morphology of a Ni/LaCrO₃ composite coating, achieved by electroplating for 10 minutes, are shown in Figure 2-3(a) (plan view) and Figure 2-3(b) (cross section). The particles are distributed uniformly throughout the Ni matrix. As seen in Figure 2-3(a), the particles are primarily located at Ni grain boundaries. The surface of the coating appears uniform, smooth and reflective to the naked eye. The dark spots present in Figure 2-3(a) and (b) are not voids, but are pullouts resulting from ultrasonic cleaning and/or polishing of the sample.

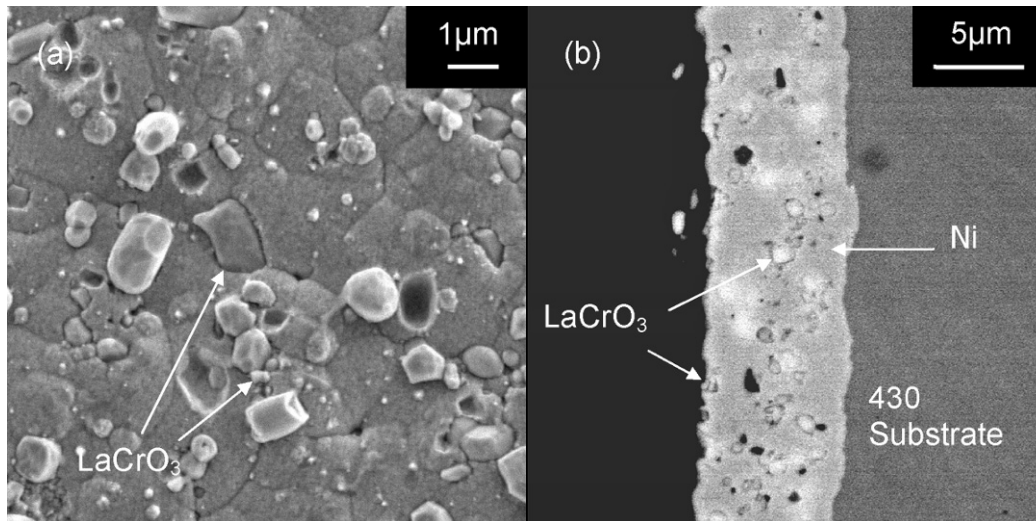


Figure 2-3 SEM images of (a) a plan view sample (secondary electron (SE)) and (b) a cross section sample (backscattered electron (BSE)) of a Ni/LaCrO₃ composite coating (~30 vol% LaCrO₃) deposited for 10 minutes. For electrolyte composition and deposition conditions see **Table 2-1**.

2.3.2 Effect of particle loading in the bath on coating particle volume fraction

Profiles of particle volume fraction in the coating (α) as a function of volume fraction of particles suspended in the plating bath (C) for 5 different current densities are shown in Figure 2-4. The particle volume fraction in the coating increases with increasing particle volume fraction suspended in the plating bath for all current densities. A sudden increase in coating particle volume fraction occurs as the bath particle loading is increased from 15 to 20 g/L (0.25 to 0.34 vol%).

For a particle loading of more than 30 g/L (0.5 vol%) and current densities over 20 mA/cm², the cathode surface was not completely covered with the coating. The impaired coverage of the cathode with the coating results in high current densities exceeding the deposition limiting current density. Since the particle loading in the bath is relatively high, metal ion transport to the cathode can be adversely affected resulting in passivation of some portions of the cathode surface.

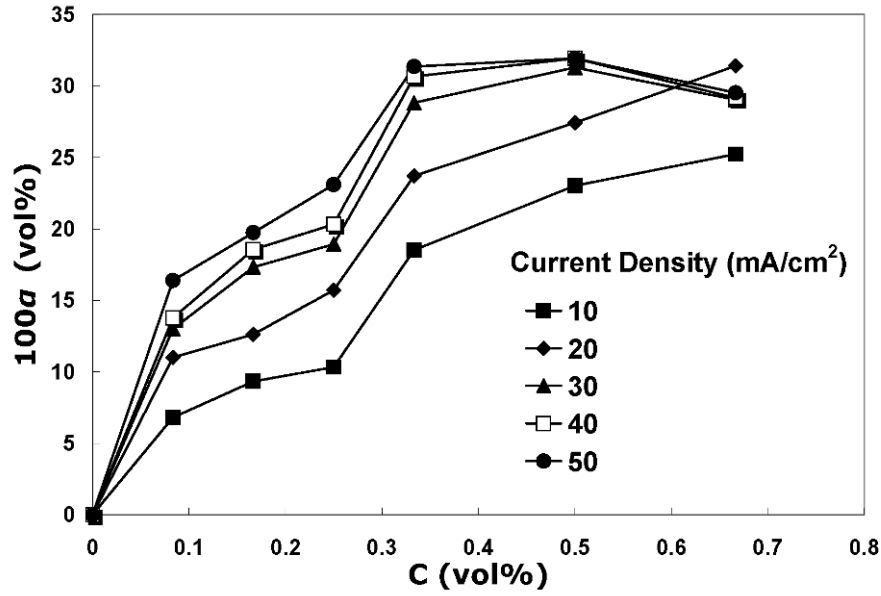


Figure 2-4 Volume fraction of particles embedded in the coating (α) as a function of the volume fraction of particles suspended in the plating bath (C) at different current densities.

Guglielmi [10] has proposed a model describing the mechanism for co-deposition of inert (nonconductive at deposition temperatures) particles in a Ni matrix, which has been reported to be valid for several composite coatings [10-13]. This model is based on a two-step theory, for loose and strong adsorption of particles. According to the proposed model, the relationship between the volume fraction of the particles in the plating bath (C) and particles embedded in the deposited coating (α) can be explained by the following equation:

$$\frac{C(1-\alpha)}{\alpha} = \frac{Wi_0}{nFd\nu_0} e^{(A-B)\eta} \left(\frac{1}{k} + C \right) \quad \text{Eq. 2-1}$$

where W is the atomic weight of the metal being deposited, i_0 is the exchange current density for the metal ions, n is the valence of the metal, d is the density of

the metal, F is the Faraday constant, v_0 is a constant related to the particle co-deposition current density, A and B are constants related to metal and particle co-deposition, respectively, η is the cathodic overpotential and k is the equilibrium constant of the loose particle adsorption reaction and represents the intensity of the interaction of particles with the cathode surface.

Eq. 2-1 also contains a current density term based on the Tafel equation, which considers the real surface area available for deposition:

$$i_0 e^{A\eta} = \frac{i}{(1-\theta)} \quad \text{Eq. 2-2}$$

where θ is the fraction of strongly adsorbed particles which reduce the amount of exposed conductive substrate surface area and is approximately equal to α . Since the Tafel equation is only valid for current densities smaller than the limiting current density for metal deposition, the Guglielmi equation is also valid only for the range of current densities smaller than the limiting current density of the metal being deposited. Therefore, providing that the current density is smaller than the limiting current density for pure Ni deposition and k is a constant for the system plots of $\frac{C(1-\alpha)}{\alpha}$ as a function of C must be intersecting straight lines for different current densities smaller than the Ni deposition limiting current density.

The intersection of such lines will be at $\frac{C(1-\alpha)}{\alpha} = 0$, where $C = -\frac{1}{k}$.

Plots of particle loading, in the range of 5-15 g/L (0.08-0.25 vol%) and for current densities up to 50 mA/cm², are shown in Figure 2-5, the straight lines intersect with the C axis at $-\frac{1}{k} \approx -0.1$ resulting in $k \approx 11$.

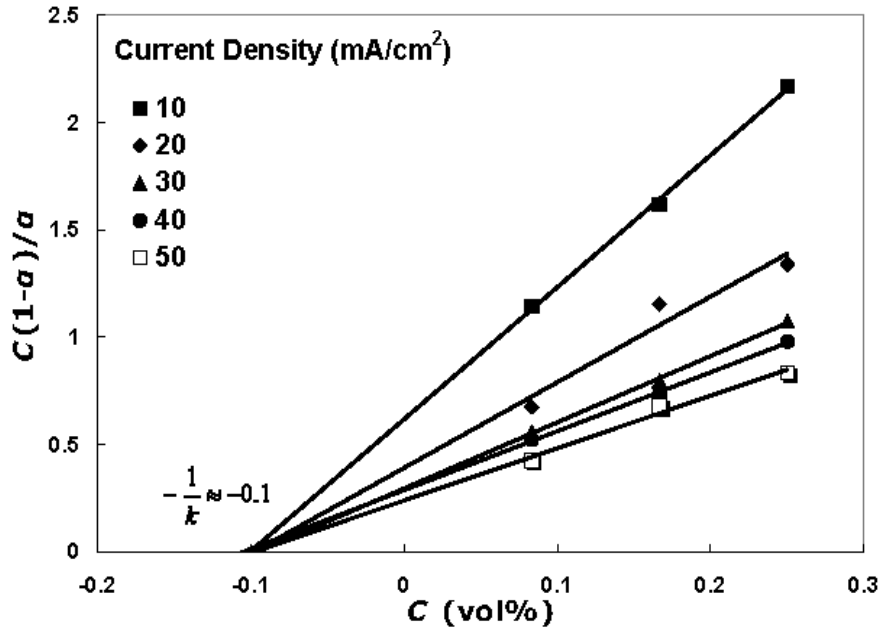


Figure 2-5 $\frac{C(1-\alpha)}{\alpha}$ as a function of volume fraction of particles suspended in the plating bath (C) for particle loadings of 5, 10 and 15 g/L (0.08, 0.17 and 0.25 vol%) at different current densities.

For particle loadings equal to or greater than 20 g/L (0.34 vol%), the slopes of the intersecting straight lines were smaller, as shown in Figure 2-6. The plots were no longer linear for current densities equal to or greater than 30 mA/cm², so only plots for current densities of 10 and 20 mA/cm² are shown. The straight lines intersect the C axis at $-\frac{1}{k} \approx -0.6$, resulting in $k \approx 1.7$. Therefore, the value of k decreased from 11 to 1.7 by increasing the volume fraction of suspended particles in the plating bath (C) from 15 to 20 g/L (0.25 to 0.34 vol%).

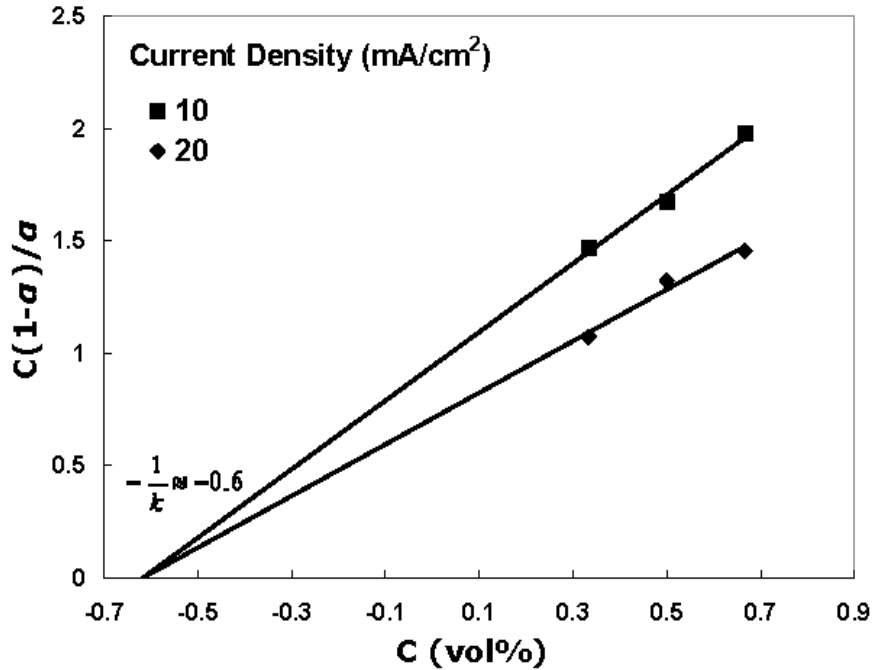


Figure 2-6 $\frac{C(1-\alpha)}{\alpha}$ as a function of volume fraction of particles suspended in the plating bath (C) for particle loadings of 20, 30 and 40 g/L (0.34, 0.5 and 0.67 vol%) at different current densities.

The relation between the fraction of loosely adsorbable particles on the available surface, which has not been previously covered with strongly adsorbed or encapsulated particles, $\frac{\sigma}{(1-\theta)}$, and C is explained in a manner similar to the classical Langmuir adsorption isotherm [10]:

$$\frac{\sigma}{(1-\theta)} = \frac{kC}{1+kC} \quad \text{Eq. 2-3}$$

where k is the adsorption process equilibrium constant at a fixed temperature. k remains constant as long as the mechanism and thus the driving force for the adsorption reaction does not change.

The decrease in the value of constant k after 15 g/L (0.25 vol%) of particle loading in the bath indicates that the mechanism of adsorption has changed. When the volume fraction of particles in the bath is smaller than a certain value (0.25 vol%), adsorption occurs mostly due to electrostatic forces stemming from the charge difference between particles and the cathode surface. Further increasing the particle loading in the bath, however, leads to an increased gravity force exerted by the mass of particles on individual particles, compressing particles onto the cathode surface, and therefore a significant gravity force contribution to the adsorption process. When the electrostatic force is the main driving force for adsorption, the adsorption process reaches an equilibrium state, where increasing C will have no effect on α . Adsorbed particles repel particles of the same charge suspended in the solution and hinder additional adsorption. Under this condition, by increasing particle loading in the bath, the increased total gravity force on individual particles, due to a greater mass of suspended particles, counteracts the repulsive electrostatic force and causes more adsorption of particles. Therefore, a change in the adsorption process mechanism and thus the driving force explains the change in the constant k .

The $\frac{B}{A}$ ratio can be calculated according to the Guglielmi model, Eq. 2-1. The slopes of the lines shown in Figure 2-5 can be determined from the following equation:

$$\tan \varphi = \frac{Wi_0}{nFdv_0} e^{(A-B)\eta} \quad \text{Eq. 2-4}$$

where $\tan \varphi$ is the slope of the lines shown in Figure 2-5. When the values of α are small enough ($(1-\theta) \approx 1$), the approximation $\frac{i}{i_0} \approx e^{A\eta}$ can be made. Therefore:

$$i_0 e^{(A-B)\eta} = i_0 \left(\frac{B}{A}\right)^{\left(1-\frac{B}{A}\right)} \quad \text{Eq. 2-5}$$

$$\tan \varphi = \frac{Wi_0}{nFdv_0} e^{(A-B)\eta} = \frac{Wi_0}{nFdv_0} i^{\left(1-\frac{B}{A}\right)} \quad \text{Eq. 2-6}$$

$$\log(\tan \varphi) = \log\left(\frac{Wi_0}{nFdv_0}\right) + \left(1-\frac{B}{A}\right) \log i \quad \text{Eq. 2-7}$$

According to Eq. 2-7, a plot of $\log(\tan \varphi)$ as a function of $\log i$ is linear with a slope of $\left(1-\frac{B}{A}\right)$. A plot for 5-15 g/L (0.08-0.25 vol%) of particle loading in the bath and current densities of 10, 20, 30, 40 and 50 mA/cm² (which give rise to relatively small values of θ) is shown in Figure 2-7. The graph shows a straight line with a slope of -0.58 giving $B = 1.58A$, which is quite close to the value $B = 1.51A$ achieved for the Ni/SiC system by Guglielmi. The $\frac{B}{A}$ ratio indicates how the current density is affecting α . When $\frac{B}{A} > 1$, increasing the current density increases α and vice versa [10].

Such an approximation cannot be made for a particle loading in the bath equal to or greater than 20 g/L (0.34 vol%), because the values of α and thus θ are not small enough.

It can be concluded that the Ni/LaCrO₃ system fits well to the Guglielmi model for particle loading in the bath (C) smaller or equal to 15 g/L (0.25 vol%).

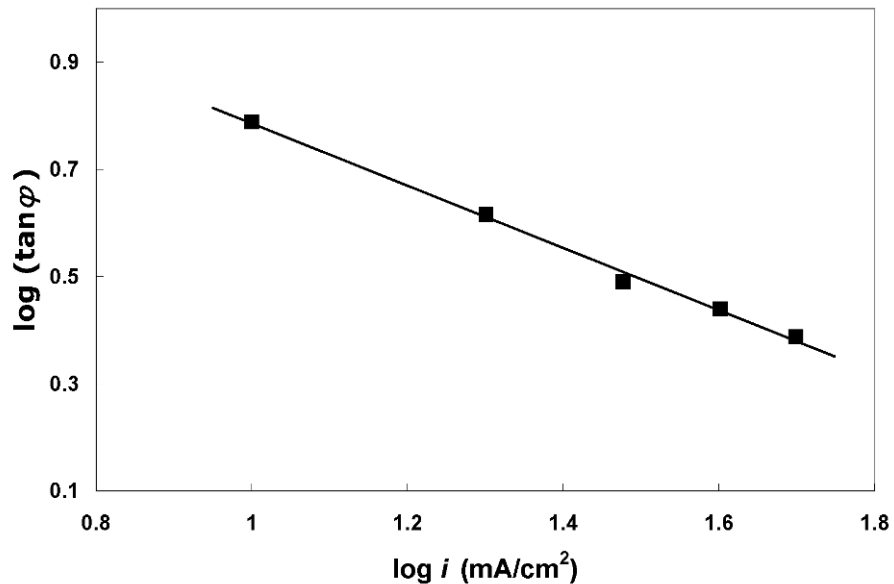


Figure 2-7 $\log(\tan \varphi)$ as a function of $\log i$ for particle loadings of 5, 10 and 15 g/L (0.08, 0.17 and 0.25 vol%).

2.3.3 Effect of bath pH on coating particle volume fraction

Figure 2-8 shows the effect of bath pH on the volume fraction of particles embedded in the coating (α). As seen in Figure 2-8, there is a clear dependency of α on the bath pH. Figure 2-8 also shows the pure Ni cathodic current efficiency, which is calculated based on relating the cathode weight gain over time to Faraday's law, as a function of bath pH. Both graphs depicted in Figure 2-8 were obtained under identical plating conditions, except that particles were not added to the pure Ni plating bath. The cathodic current efficiency for pure Ni and the volume fraction of the particles in the coating (α) show a similar dependency on bath pH values. A maximum is observed for both plots at a pH value of 4. An increase in the cathodic current efficiency results in an increase in the actual current used for deposition of Ni. As stated previously, increasing the current density leads to a greater volume fraction of particles embedded in the coating (α), as shown in Figure 2-4. At low pH values simultaneous hydrogen reduction and

evolution from the cathode surface can also interfere with co-deposition of particles, resulting in a noticeably smaller volume fraction of particles in the coating.

M. Azizi et al. [14] studied the co-deposition of SiO₂ and mica particles in a zinc matrix. According to their observations, Zn ion adsorption on the particles increases with increasing pH value of the bath. The authors also observed that the zeta potential for the particles decreases as the pH value is increased. The larger negative zeta potential for the particles, which represents the surface charge of the particles, achieved with larger pH values resulted in an increasing amount of positively charged Zn ions adsorbed on the surface of the negatively charged particles. Therefore, stronger adsorption of ion covered particles on the cathode and a greater fraction of embedded particles in the coating will occur.

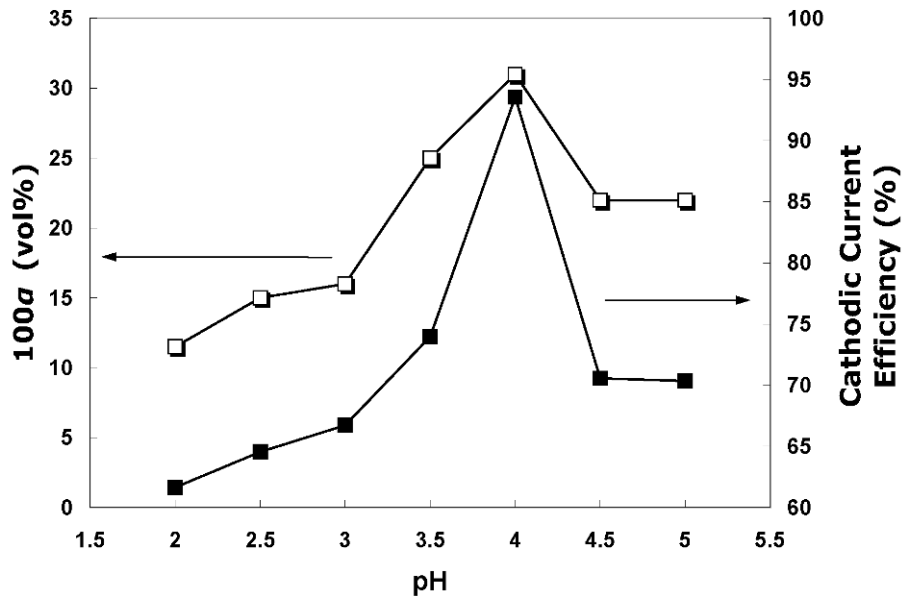


Figure 2-8 Volume fraction of particles embedded in the coating (α) and cathodic current efficiency for pure Ni deposition as a function of pH at a current density of 40 mA/cm² and 20 g/L (0.34 vol%) of particle loading in the bath (C).

For the Ni/LaCrO₃ system, the amount of Ni ion adsorption on the particles was measured, using AAS, for pH values ranging from 2-5. The results were virtually the same and showed about 20% of Ni ion adsorption on the particles in a solution containing 0.01M of Ni as sulphate. Also, particle zeta potentials for the pH range of 2-5 fluctuated near -10 mV. Therefore, in the Ni/LaCrO₃ system, the pH value does not have a significant effect on the surface properties of suspended particles in the electrolyte. The only parameter which is changing with pH, and has a marked effect on the volume fraction of particles embedded in the coating, is the cathodic current efficiency.

2.3.4 Effect of hydrodynamic parameters on volume fraction of particles embedded in the coatings

Figure 2-9 represents the effect of stirring rate on the volume fraction of the particles embedded in the coatings obtained with two different flow patterns: magnetic stirring which forms a spiral flow pattern from bottom-to-top and stirring with an overhead marine-type mixing impeller which produces a spiral fluid pattern from top-to-bottom. For magnetic stirring, the volume fraction of particles embedded in the coating (α) increases from 200 to 300 rpm, remains almost constant up to 400 rpm and then decreases dramatically at agitation rates greater than 400 rpm. The increase in α from 200 to 300 rpm is attributed to insufficient suspension of particles due to low stirring rates. Since the stirring is from the bottom to the top, the decrease in particle volume fraction at high suspension stirring rates (>400 rpm) can be attributed to the suspension flow force on particles. This force is in the opposite direction of the gravity force, due to bottom-to-top stirring, and lifts the particles from the cathode surface. The presence of such a lifting force results in decreased particle adsorption. By changing the flow pattern of the suspension to top-to-bottom with an overhead impeller, a force in the same direction as the particle gravity force will be applied to the particles resulting in enhanced adsorption. This effect is seen in Figure 2-9, where α increases linearly with increasing stirring rate. Application of even higher stirring rates was not possible due to limitations of the process design.

The presence of reasonably conductive LaCrO_3 particles (resistivity is $\sim 10 \Omega\text{cm}$ at 800°C [6]) in poorly conductive chromia ($\sim 100 \Omega\text{cm}$ at 800°C [2]) is expected to increase the electrical conductivity of the oxide scale. In addition, NiO has a resistivity of $\sim 7 \Omega\text{cm}$ at 800°C [2]) which is ~ 15 times lower than that for chromia at the same temperature. Therefore, the entire double layer oxide scale is expected to exhibit superior electrical conductivity over the scale that forms on the surface of uncoated stainless steels. Long-term oxidation behaviour, oxide scale characteristics and electrical properties of Ni/LaCrO_3 coatings will be discussed thoroughly in Chapter 3 of this thesis.

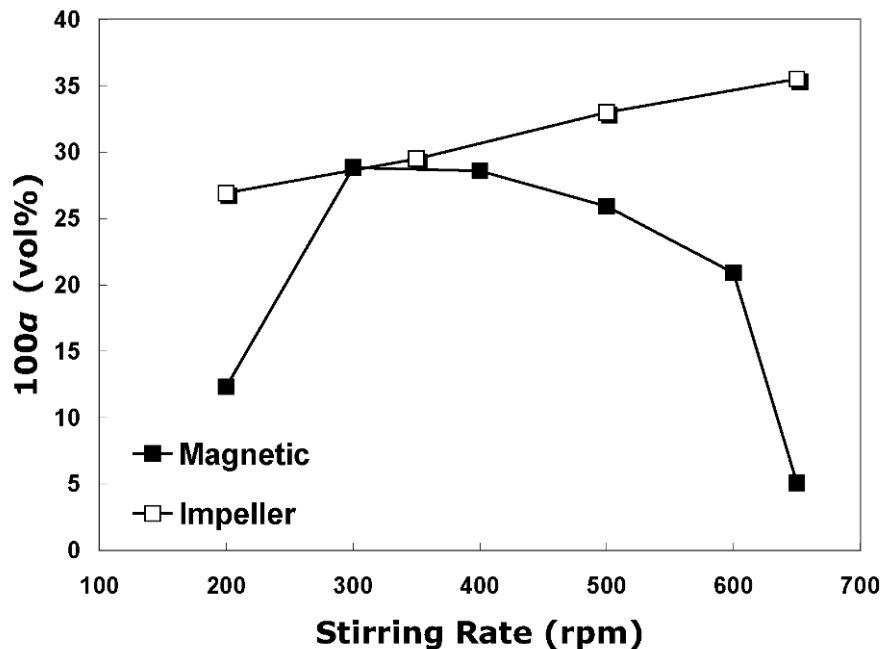


Figure 2-9 Volume fraction of particles embedded in the coatings (α) as a function of bath agitation rate at a current density of 40 mA/cm^2 and a 20 g/L (0.34 vol\%) particle loading in the bath.

2.4 Conclusions

A method for co-deposition of LaCrO₃ particles in a Ni matrix on 430 stainless steel substrates, via electroplating, has been successfully developed. The effects of particle loading in the bath, deposition current density, solution pH, Ni ion adsorption on particles, particle zeta potential and electrolyte hydrodynamics on the volume fraction of embedded particles in the coatings were studied and optimized. The volume fraction of particles in the coating (α) was measured by means of image analysis.

Increasing particle loading in the bath (C) up to 20 g/L (0.34 vol%), as well as increasing the current density up to 50 mA/cm², increases the volume fraction of particles in the coating (α) until a limiting value (~30 vol%) is reached. The effect of particle loading and current density was described by the Guglielmi model. The maximum cathodic current efficiency (94%) and the maximum volume fraction of particles in the coatings (α) were obtained for solutions with pH levels of 4. Stirring the electrolyte with a toward-the-cathode surface flow pattern proved to be more effective than stirring in the opposite manner and increased the maximum volume fraction of particles in the coating increased from ~30 to ~35 vol%. The optimum conditions to achieve the highest volume fraction of particles in the coatings (α) were determined to be 20 g/L (0.34 vol%) of particle loading (C), 40-50 mA/cm² of current density, a pH of 4 and a stirring pattern of top-to-bottom (towards-the-cathode). Under the optimum conditions, a volume fraction of embedded particles in the coatings (α) of ~35 vol% was obtained.

2.5 References

1. Z. G. Yang, K. S. Weil, D. M. Paxton and J. W. Stevenson, *Journal of The Electrochemical Society*, **150**, A1188 (2003).
2. W. Z. Zhu and S. C. Deevi, *Materials Science and Engineering*, **A348**, 227 (2003).

3. Z. G. Yang, M. S. Walker, P. Singh, J. W. Stevenson and T. Norby, *Journal of the Electrochemical Society*, **151**, B669 (2004).
4. K. Kendall, *International Materials Reviews*, **50**, 257 (2005).
5. J. W. Fergus, *Solid State Ionics*, **171**, 1 (2004).
6. Meadowcr.Db, *Journal of Physics D-Applied Physics*, **2**, 1225 (1969).
7. M. P. Brady, B. A. Pint, Z. G. Lu, J. H. Zhu, C. E. Milliken, E. D. Kreidler, L. Miller, T. R. Armstrong and L. R. Walker, *Oxidation of Metals*, **65**, 237 (2006).
8. S. J. Geng, J. H. Zhu, M. P. Brady, H. U. Anderson, X. D. Zhou and Z. G. Yang, *Journal of Power Sources*, **172**, 775 (2007).
9. *Standard Practice for Preparation of and Electroplating on Stainless Steel, B254-92*, American Society for Testing and Materials (ASTM) (2004).
10. Guglielmi.N, *Journal of the Electrochemical Society*, **119**, 1009 (1972).
11. P. Bercot, E. Pena-Munoz and J. Pagetti, *Surface & Coatings Technology*, **157**, 282 (2002).
12. H. F. Liu and W. X. Chen, *Intermetallics*, **13**, 805 (2005).
13. H. F. Liu and W. X. Chen, *Surface & Coatings Technology*, **191**, 341 (2005).
14. M. Azizi, W. Schneider and W. Plieth, *Journal of Solid State Electrochemistry*, **9**, 429 (2005).

3 Oxidation and Electrical Behavior of Ni/CrO₃ Coated Stainless Steel Interconnects

3.1 Introduction

In an effort to increase the conductivity and reduce Cr migration and poisoning of AISI-SAE 430 steel interconnects, an electrodeposited composite coating of LaCrO₃ particles in a Ni matrix has been developed and studied in Chapter 2. The issues regarding the use of uncoated commercial ferritic stainless steels have been previously discussed in Chapter 1 in detail.

The objective of the current work is to study and characterize the long-term (up to 2040 hours at 800°C) oxidation behavior and the oxide scale electrical properties for Ni/LaCrO₃-coated AISI-SAE 430 steels. The procedure for composite deposition of Ni/LaCrO₃ for AISI-SAE 430 steel coupons has been described in Chapter 2. SEM/EDX, XRD, SIMS and AES were used to characterize the oxide scales. The oxidation behaviour of Ni-coated and uncoated substrates were also studied and the results were compared with Ni/LaCrO₃ coatings. Superior oxidation and oxide scale spallation resistance as well as excellent electronic conductivity were achieved with the application of Ni/LaCrO₃ coatings.

3.2 Experimental methods

Coupons of AISI 430 stainless steel, measuring 20 mm × 10 mm × 1 mm were used as substrates. The composition of AISI 430 stainless steel is listed in Table 3-1. Specimens were cleaned, activated and electrodeposited with Ni/LaCrO₃ from a Watts nickel plating bath containing 20 g/L of suspended LaCrO₃ particles*. The deposits were ~7 μm thick and contained ~30 vol% LaCrO₃. For the purpose of comparison, identical samples were also electroplated with pure Ni

* For particle size distribution see **Figure 2-2**

to a thickness of $\sim 7 \mu\text{m}$. The deposition procedure was optimized and is described in Chapter 2 of this thesis. Oxidation tests were performed for specimens in static air at 800°C in an electrical box furnace for up to 2040 hours.

Table 3-1 Chemical composition of AISI 430 stainless steel

Element	Fe	C	Cr	Mn	Si	S	P
Concentration (wt.%)	Bal.	0.12	16-	1	1	0.03	0.04
		max	18	max	max	max	max

The detailed method of cross sectional sample preparation has been discussed in Chapter 2 (Section 2-2) of this thesis. A Hitachi H2700 SEM, equipped with a Princeton Gamma-Tech (Prism IG) UTW EDX spectrometer was used for imaging and chemical analysis. A Rigaku Geigerflex 2173 rotating anode system was employed for the purpose of glancing angle ($\theta = 2^\circ$) XRD analysis and phase identification of oxidized specimens. The X-ray penetration depth for this angle was about $10 \mu\text{m}$. The anode used for XRD was cobalt with CoK_α radiation with the wavelength of $\lambda = 0.1789 \text{ nm}$. Due to spatial resolution limitations, associated with EDX analysis, depth profiling for oxidized (170 and 2040 hours) Ni/LaCrO₃-coated specimens was performed by means of SIMS. The instrument employed for this purpose was an Ion-ToF SIMS IV. Specimens were sputtered with Cs⁺ ions at 1 keV and 250 nA. The sputtering area was $200 \times 200 \mu\text{m}$. Ga⁺ ion sputtering at 15 keV over an area of $34 \times 34 \mu\text{m}$ was used for analysis. A JEOL Auger scanning microprobe (JAMP 9500F) was used for surface analysis and elemental mapping of oxidized Ni/LaCrO₃-coated AISI 430 steels. The specific weight gains for oxidized specimens were measured according to the method described in Section 2-2 of this thesis.

In order to measure the ASR of the oxidized samples, the set-up shown in Table 3-1 was employed. Platinum wires were spot welded to one side of two identical non-oxidized samples to provide electrical connections. To avoid alloy-to-alloy adhesion and erroneous results, platinum wire welded coupons were pre-oxidized

for 24 hours at 800°C. No conductive paste, which may affect the oxidation mechanism, was applied between the two samples. To prevent contact loss between samples, a static load of 9.8 N was applied to the samples. A constant current density of 300 mA/cm² was applied and the voltage was recorded every 120 seconds. An electrochemical measurement instrument, Gamry Series G 300, was employed for this purpose. The data were used to calculate the resistance according to Ohm's law and the ASR was calculated as a product of the resistance and surface area. In order to measure the resistance contribution from the junctions, wires and the alloy, two platinum wires were spot welded to the sides of a single AISI 430 coupon and the resulting resistance was subtracted from the original test results. All the above-mentioned tests, including ASR and other oxidation tests, were run at 800°C in an electric box furnace and static air.

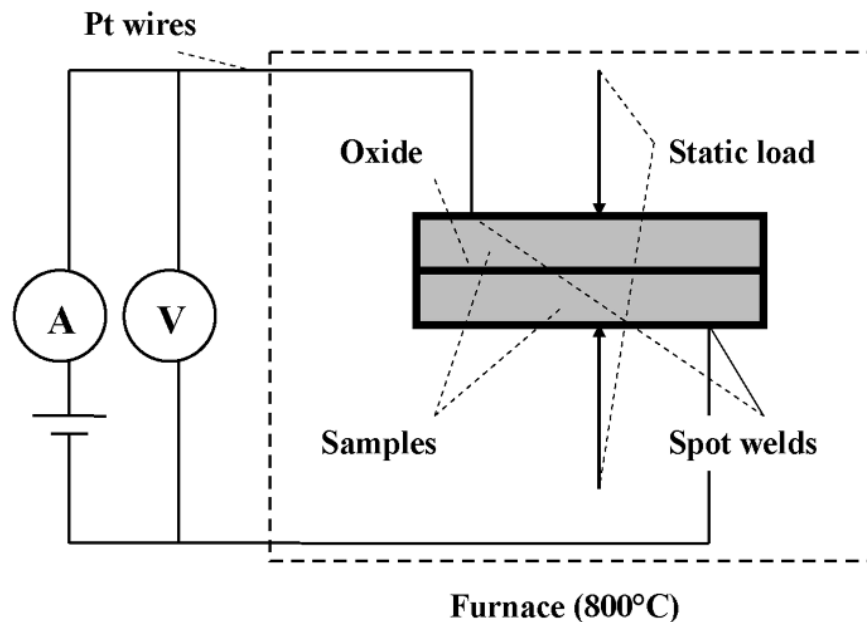


Figure 3-1 Experimental set-up for measuring the electrical contact resistance of oxide scales.

3.3 Results and discussion

3.3.1 Scale characterization

SEM plan view and cross sectional images of Ni/LaCrO₃-coated specimens, oxidized for 170 and 2040 hours at 800°C in air, are shown in Figure 3-2. The compositions of the numbered regions on the images were determined by EDX analysis and are listed in Table 3-2. Oxygen levels are not shown in the table. Figure 3-2(a) and (c) show that the oxide surfaces consist of some large oxide particles (region (1) in Figure 3-2(a) and (c)) embedded in a fine-grained matrix (region (2) in Figure 3-2(a) and (c)). EDX analysis (Table 3-2) shows that the coarse particles are rich in Ni (>70 wt.%), while the matrix grains of the coating are rich in both Fe and Ni. Both regions contain small amounts of Mn and Cr (<1 wt.%). No cracks and/or spalled areas were observed on the surface, even though the samples were air-cooled from 800°C to room temperature.

From Figure 3-2(b) and (d), it is evident that the oxide scales consist of two distinguishable layers. The brighter outer layer, which is also seen in the plan view images (Figure 3-2(a) and (c)), shows different regions of dark and light contrast in the BSE images (Figure 3-2(b) and (d)). The regions with higher concentrations of Ni appear lighter. This outer scale retains its thickness over the oxidation period as seen in Figure 3-2(b) and (d). According to the EDX analysis (Table 3-2), the concentrations of both Mn and Cr in this layer increase slightly with increasing oxidation time. The Mn concentration increases more noticeably in region (2). The Cr concentration does not exceed 3 wt.% in the outer scale. This indicates that Cr migration to the scale surface and consequently Cr volatilization has been inhibited. The apparent porosity in the oxide scale, seen in the cross sectional images (Figure 3-2(b) and (d)), are particle pullouts, resulting from polishing and ultrasonic cleaning. The inner scale (region (3) in Figure 3-2(b) and (d)) is rich in Cr, and also contains Mn, Fe and Ni. This layer grows as the oxidation time is increased. The LaCrO₃ particles are distributed throughout this Cr-rich subscale. An adherent, but uneven alloy-scale boundary is seen for the

specimen oxidized for 170 hours (Figure 3-2(b)). Porosity at the alloy-scale interface, however, is seen for the specimen oxidized for 2040 hours (Figure 3-2(d)).

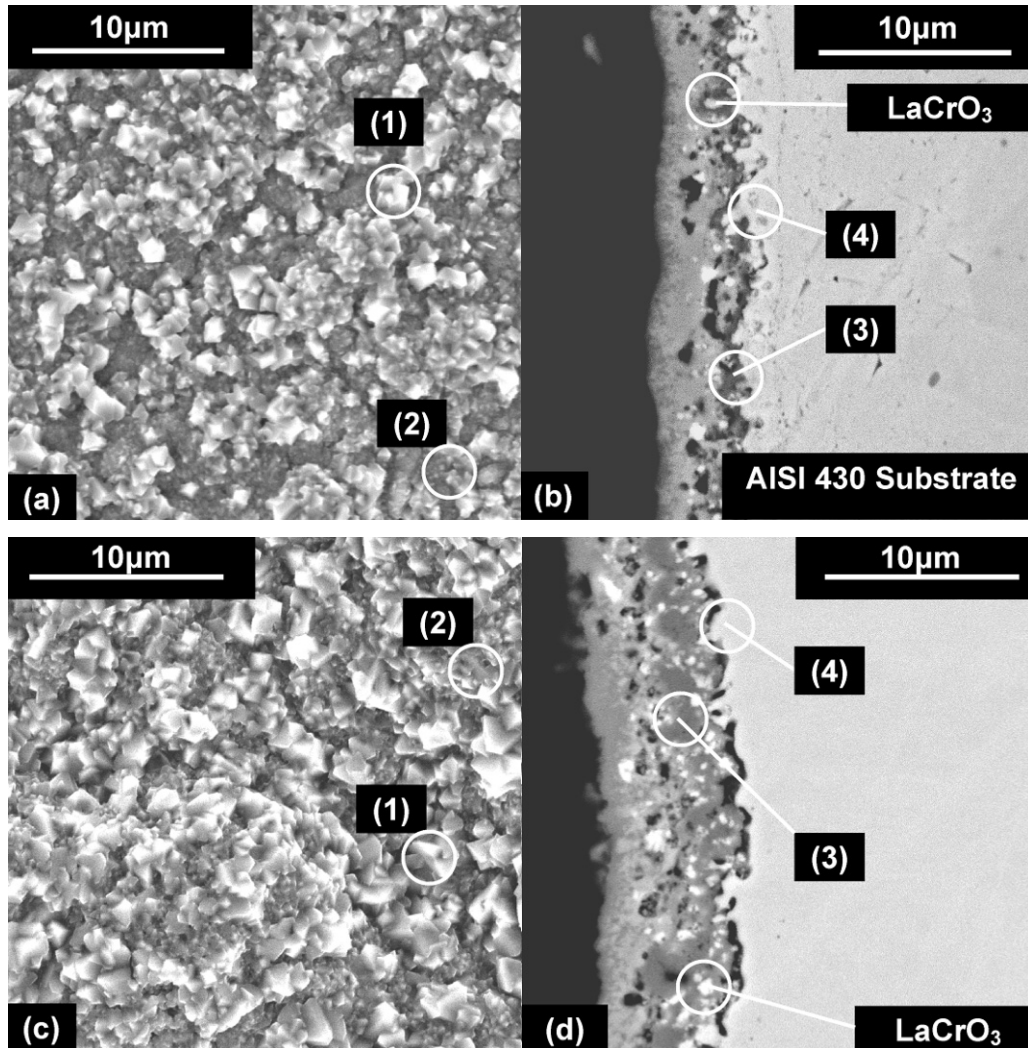


Figure 3-2 SEM images of oxidized Ni/LaCrO₃ coated AISI 430 stainless steels: (a) and (b) after 170 hours; (c) and (d) after 2040 hours of oxidation in air at 800°C. (a) and (c) are plan view SE images; (b) and (d) are cross sectional BSE images.

Table 3-2 Compositions (wt.%) determined by EDX point analysis for different regions shown in **Figure 3-2**

Regions (points)	Figure 3-2(a) and (b) (170 h)					Figure 3-2(c) and (d) (2040 h)				
	Fe	Ni	Cr	Mn	Si	Fe	Ni	Cr	Mn	Si
(1)	11	85	3	1	0	16	80	2	2	0
(2)	58	40	1	1	0	45	48	2	5	0
(3)	18	27	50	2	3	14	9	72	5	0
(4)	65	22	10	2	1	78	8	12	1	1

The presence of 22 wt.% Ni in the substrate surface region (region (4)) for the specimen oxidized for 170 hours shows that a portion of Ni diffuses into substrate during initial oxidation. After long-term oxidation, the Ni concentration in the same region drops to 8 wt.%. The decrease in the Ni content is not due to oxidation, since the thickness of the outer scale, containing Ni, does not increase substantially. Therefore, during high-temperature oxidation, Ni diffuses into the substrate and is replaced with Fe and Cr diffusing out from the substrate towards the alloy-scale interface.

The phases that form in the Ni/LaCrO₃-coated specimens during oxidation for 170 and 2040 hours were identified by means of glancing angle X-ray diffraction with the aid of EDX microanalysis. The XRD patterns from the scales are shown in Figure 3-3. The identified phases for the sample oxidized for 170 hours include FCC spinel, rhombohedral chromia (with Fe, Ni and Mn), cubic NiO and perovskite-type LaCrO₃. There may be peaks from the FCC Fe-Ni-Cr substrate surface region present in the patterns, but they overlap with FCC spinel and NiO peaks, making identification inconclusive. Also, some peaks for the FCC spinel and NiO phases overlap, but EDX analysis confirms their presence. In addition to the phases identified for the sample oxidized for 170 hours, two BCC substrate peaks at $2\theta = 52.34^\circ$ ($d_{110} = 0.2028$ nm) and $2\theta = 77.18^\circ$ ($d_{200} = 0.143$ nm) appear in the pattern obtained from the specimen oxidized for 2040 hours. Since Ni is a

well known austenite stabilizer in stainless steels, an FCC to BCC phase transformation was likely in the surface region of the substrate, adjacent to the scale, due to a drop in the Ni concentration from 22 wt.% (170 hours of oxidation) to 8 wt.% or less after further oxidation (2040 hours).

The peaks identified as chromia-rich are more intense for the specimen oxidized for 2040 hours than those for 170 hours of oxidation. This indicates that more of the chromia-rich phase has formed for samples oxidized for 2040 hours than for samples oxidized for 170 hours. This is consistent with the cross sectional images in Figure 3-2(b) and (d).

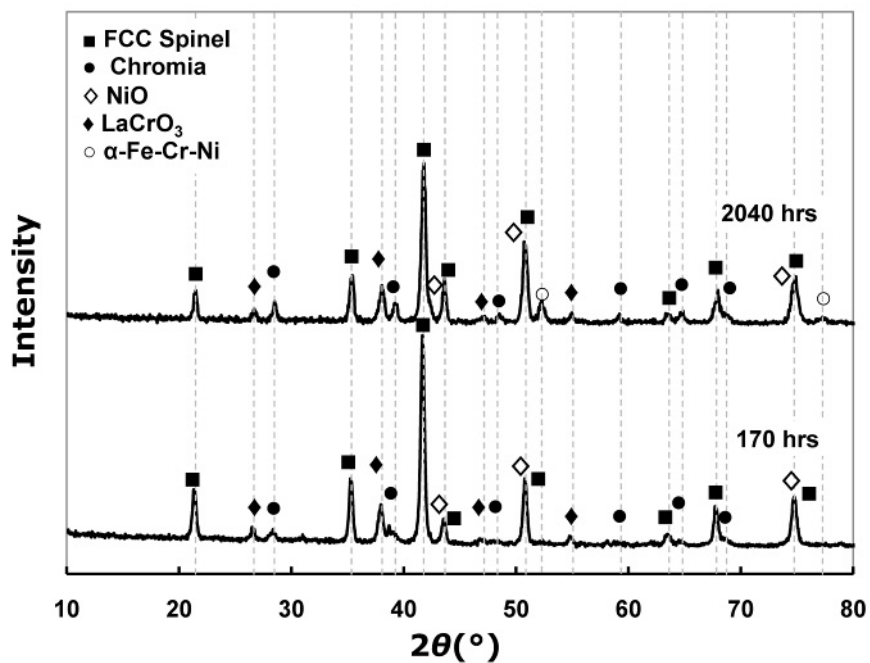


Figure 3-3 XRD patterns for Ni/ LaCrO_3 -coated AISI 430 stainless specimens oxidized for 170 and 2040 hours.

SIMS depth profiles for Ni/ LaCrO_3 -coated specimens oxidized for 170 and 2040 hours are shown in Figure 3-4. Both Cr profiles show a maximum in the chromia-rich subscale. The Cr intensity increase in the spinel/NiO layer, near the surface,

is seen in both profiles. This may be due to Cr solubility in the spinel phase. EDX analysis results from cross sectional images do not show more than 3 wt.% Cr in the spinel/NiO layer. The Fe and Ni profiles exhibit a decrease through the chromia-rich layer followed by an increase in the outer scale. The Mn profile shows a high concentration of Mn in the outer oxide layer, which corresponds to the spinel layer. Manganese is able to easily diffuse through the chromia-rich subscale into the outer scale. Comparison between Figure 3-4(a) and (b) shows that the Mn content in the spinel phase increases with oxidation time. EDX results (Table 3-2) also confirm that the amount of Mn in the spinel phase has increased from 2 to 5 wt.% (region (2) in Figure 3-2) with increasing oxidation time from 170 to 2040 hours. Silicon segregation (likely as SiO₂) is evident at the alloy-scale interface beneath the chromia-rich subscale. This segregation is more noticeable in Figure 3-4(b) for the sample oxidized for 2040 hours. Lanthanum appears in the entire scale depth with a higher concentration in the chromia-rich scale where most of particles are located. The presence of La on the surface, where there are no LaCrO₃ particles in the SEM images (Figure 3-2(a) and (c)), indicates that La ions diffuse from the particles present throughout the scale.

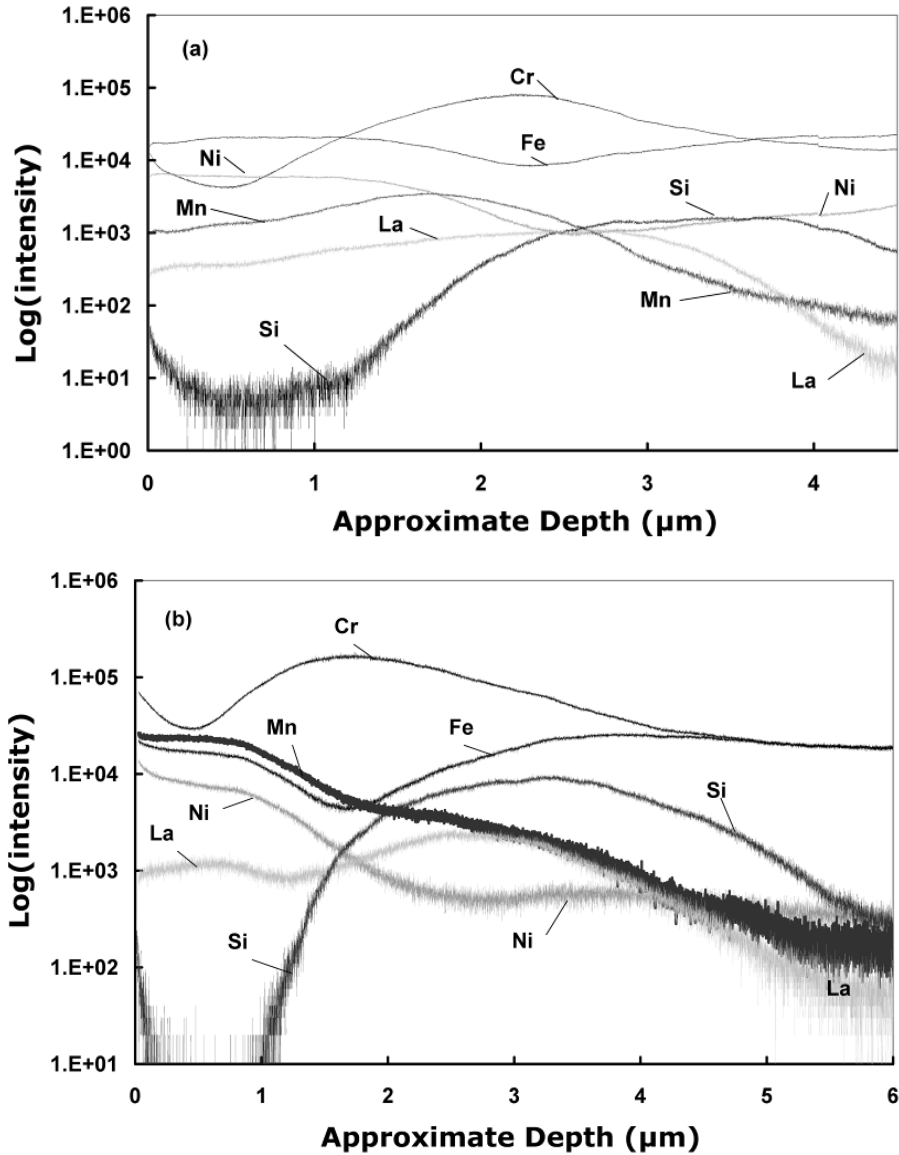


Figure 3-4 SIMS depth profiles for oxidized Ni/LaCrO₃-coated AISI 430 stainless specimens for (a) 170 and (b) 2040 hours of oxidation.

In summary, the thermally grown oxide scale forming on the surface of Ni/LaCrO₃-coated AISI 430 stainless steels is a double layer consisting of a slowly growing, particle filled chromia-rich subscale, containing some Fe, Ni and Mn, and a complex Ni-Fe-Mn-Cr spinel/NiO outer scale which does not grow significantly with oxidation time. The 3 wt.% Cr (determined by EDX) in the outer scale (Table 3-2) also indicates that Cr migration from the chromia-rich

subscale has been effectively limited by the outer scale. Segregation of Si (likely as SiO_2) at metal-oxide scale interface is clearly seen, although the layer does not appear to be continuous (Figure 3-2(b) and (d)). The porosity at the metal-oxide scale interface for the sample oxidized for 2040 hours (Figure 3-2(d)) may be due to the formation of this discontinuous silica layer. Silica is not miscible with chromia [1, 2] and the adhesion between the two oxides is poor. However, no spallation was observed in the case of Ni/LaCrO₃-coated steels.

In order to compare the oxide scale morphology of Ni/LaCrO₃ coated samples with uncoated substrates, cross sectional and surface images of oxidized AISI-SAE 430 uncoated substrates are demonstrated in Figure 3-5. Images of specimens oxidized for 170 hours are shown in Figure 3-5(a) and (b) and those obtained from substrates oxidized for 2040 hours are presented in Figure 3-5(c) and (d). The scale, which grows on the uncoated substrates, consists of an inner chromia scale and an outer Mn-Cr spinel. The scale characterization for AISI-SAE 430 steels has been conducted previously in our research group by means of EDX/XRD [3, 4]. As seen in Figure 3-5(a), there is a continuous gap at the metal-oxide scale interface where there is also a continuous layer of silica. The presence of silica layer has been confirmed in [3] by means of EDX line scanning and SIMS depth profiling. Spallation of the scale is observed for uncoated substrates and shown in Figure 3-5(b). The spalled areas are so large that can be observed even with naked eye. As previously discussed, there is neither spallation of the scale or a continuous gap at the metal-oxide scale interface observed for Ni/LaCrO₃-coated, oxidized steels. Elimination of the scale spallation is, therefore, an obvious advantage of coated over uncoated steels.

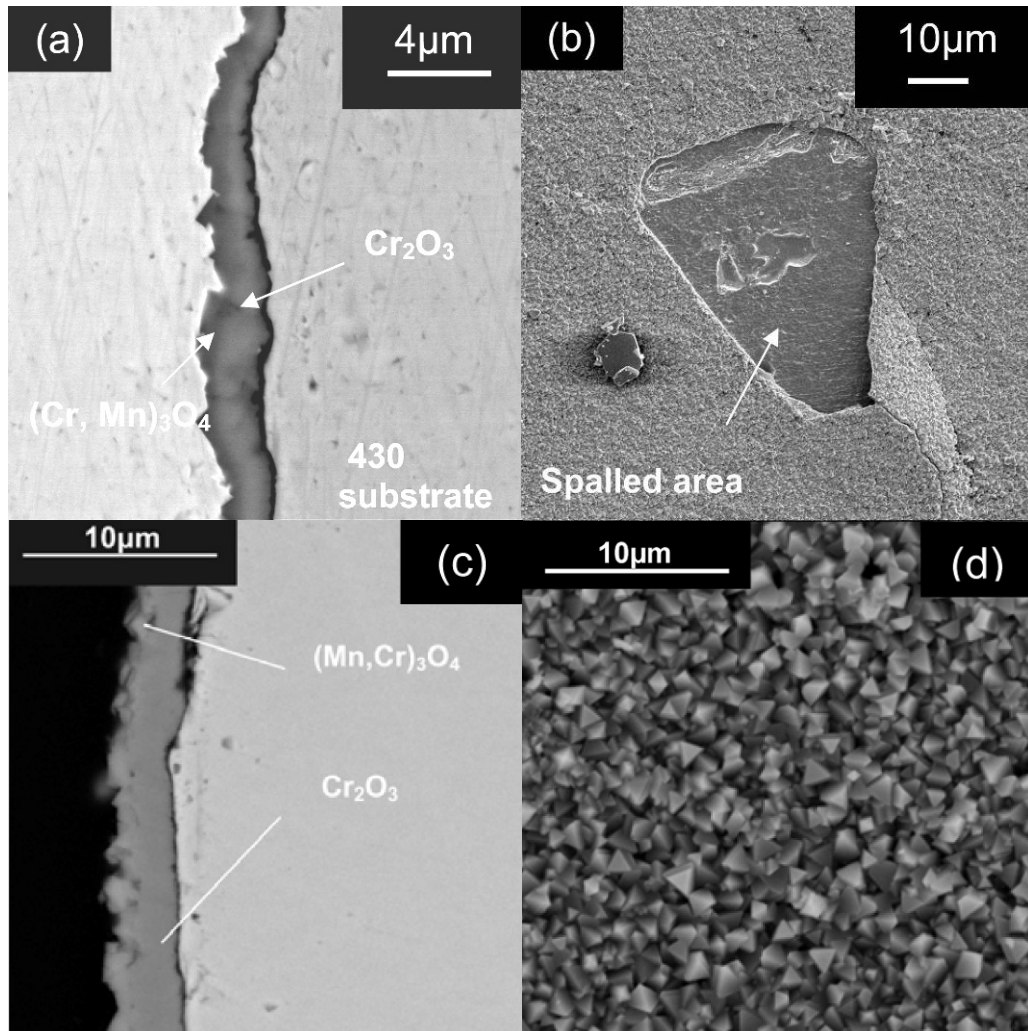


Figure 3-5 SEM images of oxidized uncoated AISI 430 stainless steels: (a) and (b) after 170 hours; (c) and (d) after 2040 hours of oxidation in air at 800°C. (a) and (c) are cross sectional BSE images; (b) and (d) plan view SE images.

3.3.2 Effect of LaCrO_3 particles on oxidation behaviour

In order to determine the effect of LaCrO_3 particles on the oxidation behavior of Ni/ LaCrO_3 -coated samples, identical substrates were plated with pure Ni to the same thickness ($\sim 7 \mu\text{m}$) and oxidized under the same conditions as the Ni/ LaCrO_3 -coated samples. SEM plan view and cross sectional images of these samples are shown in Figure 3-6. The composition of the numbered regions in Figure 3-6 are tabulated in Table 3-3. A thicker scale, in comparison with that grown on the Ni/ LaCrO_3 -coated specimens, forms on the Ni-coated samples. A

wide gap is also visible between the substrate and scale in Figure 3-6(d). It is clear from comparing Figure 3-6(a) and (c) that the outer oxide particles for the Ni-coated samples have grown significantly larger from 170 to 2040 hours of oxidation, relative to what was seen for the Ni/LaCrO₃-coated steels shown in Figure 3-6(a) and (c). For these samples, only a small change in oxide particle size occurred. Large, isolated nodules of oxide start to form and grow on the surface of Ni-coated samples after oxidation times longer than 600 hours. Examples are shown in Figure 3-6(e) and (f) for a Ni-coated specimen oxidized for 2040 hours. XRD analysis of the Ni coated samples indicated that the nodules were hematite Fe₂O₃; chromia, spinel and NiO were also identified (Figure 3-7).

According to EDX analysis (Table 3-3 region [4]), the concentration of Cr in the substrate surface does not exceed ~10 wt.%, which is below the critical concentration of Cr (12 wt.%) needed to form a protective chromia layer. The drop in Cr concentration at the surface of substrate is due to inward diffusion of a portion of the non-oxidized Ni, which also occurs for the Ni/LaCrO₃-coated samples. In addition, there is rapid outward diffusion of Cr, contributing to formation of a thick chromia-rich subscale. For Ni/LaCrO₃-coated samples oxidized for 2040 hours, the concentration of Cr at the surface of the substrate is 12 wt.% (Table 3-2, region (4)). This indicates that for the composite coating, less Cr contributes to the formation of the chromia-rich layer and that a more protective, less permeable chromia-rich layer forms in the presence of the LaCrO₃ particles. No damage to the chromia-rich subscale, with the corresponding formation of oxide nodules, was observed even after 2040 hours of oxidation for Ni coatings with LaCrO₃.

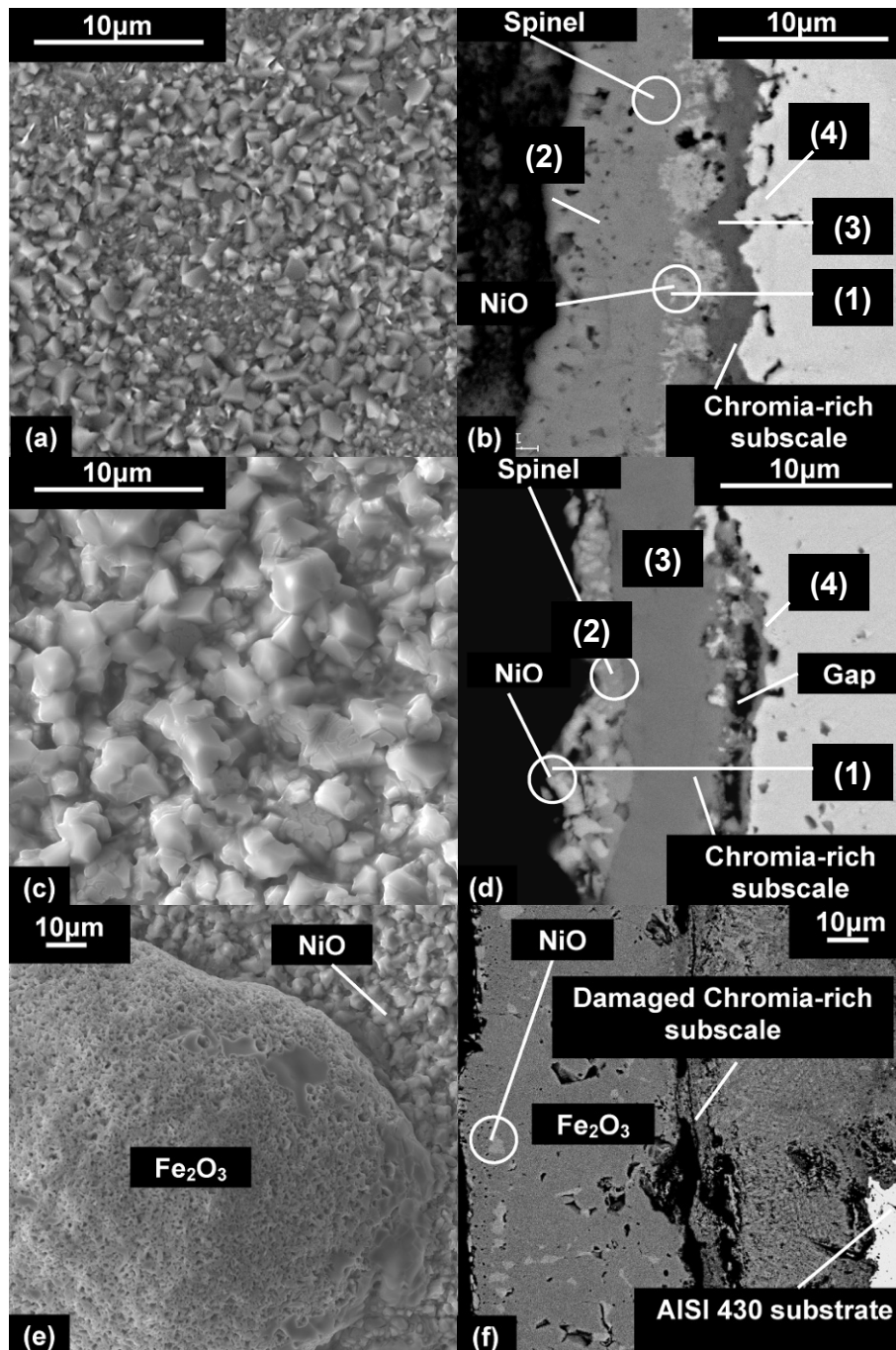


Figure 3-6 SEM images for oxidized Ni-coated AISI 430 stainless steels: (a) and (b) after 170 hours; (c), (d), (e) and (f) after 2040 hours of oxidation in air at 800°C. (e) and (f) show oxide nodules; (a), (c) and (e) are plan view SE images; (b), (d) and (f) are cross sectional BSE images.

Table 3-3 Compositions (wt.%) determined by EDX point analysis for different regions shown in **Figure 3-6**.

Regions (points)	Figure 3-6(b) (170 h)					Figure 3-6(d) (2040 h)				
	Fe	Ni	Cr	Mn	Si	Fe	Ni	Cr	Mn	Si
(1)	8	90	2	0	0	9	81	6	3	0
(2)	62	36	2	1	0	42	35	17	4	0
(3)	5	2	89	2	0	14	8	68	7	0
(4)	65	26	8	1	1	82	5	12	1	1

Figure 3-8 shows the specific weight gains for cyclically oxidized Ni/LaCrO₃-coated, Ni-coated and uncoated AISI 430 stainless steels. Ni/LaCrO₃-coated and uncoated steels show a similar weight gain trend, except for the initial stage when Ni oxidizes faster than the uncoated steel. Ni-coated samples, however, exhibit notably faster oxidation rates in comparison with both Ni/LaCrO₃-coated and uncoated steels. Exponential oxidation kinetics is seen after 600 hours when Fe oxide nodules start to appear and grow. From the SEM images (Figure 3-2 and Figure 3-6) and weight gain results (Figure 3-8), it is evident that Ni/LaCrO₃-coated steels exhibit superior oxidation resistance, in terms of scale growth rate and formation of a protective scale, over Ni-coated samples.

The marked improvement in the oxidation resistance is attributed to the presence of LaCrO₃ particles, which is the only difference between the Ni/LaCrO₃-coated and Ni-coated samples. Lanthanum, present in the dispersed particles, is considered to be a reactive element (RE), which can greatly improve the oxidation resistance and scale adhesion of high-temperature alloys [5-16].

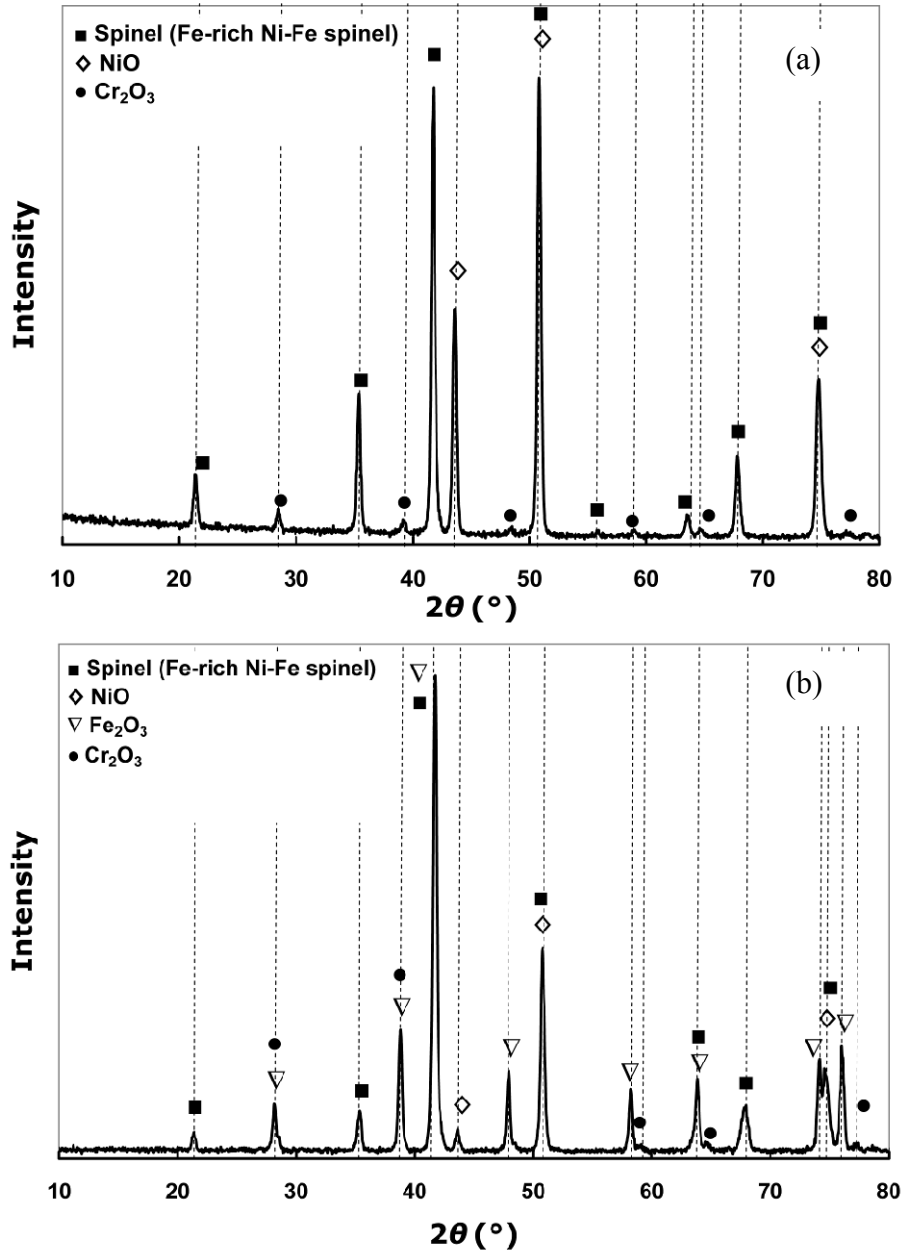


Figure 3-7 XRD patterns for Ni-coated AISI 430 stainless specimens oxidized for (a) 170 and (b) 2040 hours.

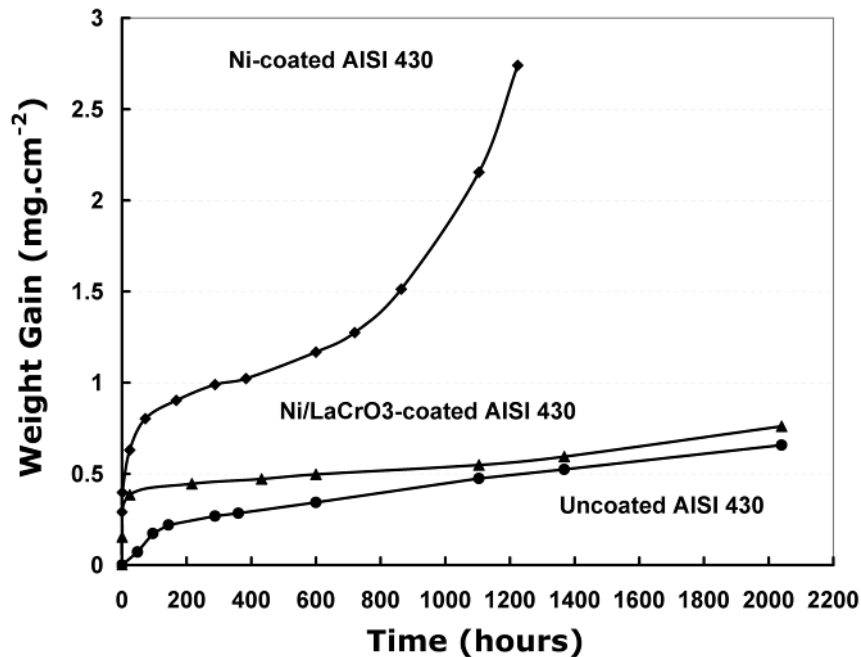


Figure 3-8 Specific weight gains for oxidized Ni/LaCrO₃-coated, Ni-coated and uncoated AISI 430 stainless steels as a function of oxidation time.

AES was performed for Ni/LaCrO₃-coated specimens oxidized for 2040 hours. In addition to Ni, Fe, Mn, Cr and O, trace amounts of La and S were detected on the oxide surface. Sulfur is present as an impurity in the steel (to a maximum of 0.03 wt.%). Also, the Ni plating solution may introduce trace amounts of co-deposited sulfur to the coating, although a saccharin-free bath was used. Figure 3-9 depicts an SE image (Figure 3-9(a)) and the corresponding Auger electron maps for La (Figure 3-9(c)). Regions appearing brighter on the maps (according to intensity bars shown on the maps) correspond to higher concentration of elements in question, i.e., La and S. Regions that show up darker have negligible concentrations of the elements. Lanthanum shows a higher concentration along the crystal edges and grain boundaries. Sulfur is detected in grain boundary junctions, indicated by the circled regions. Where sulfur is concentrated, La is also present with a higher concentration than for the rest of surface. This indicates that sulfur is associated with lanthanum.

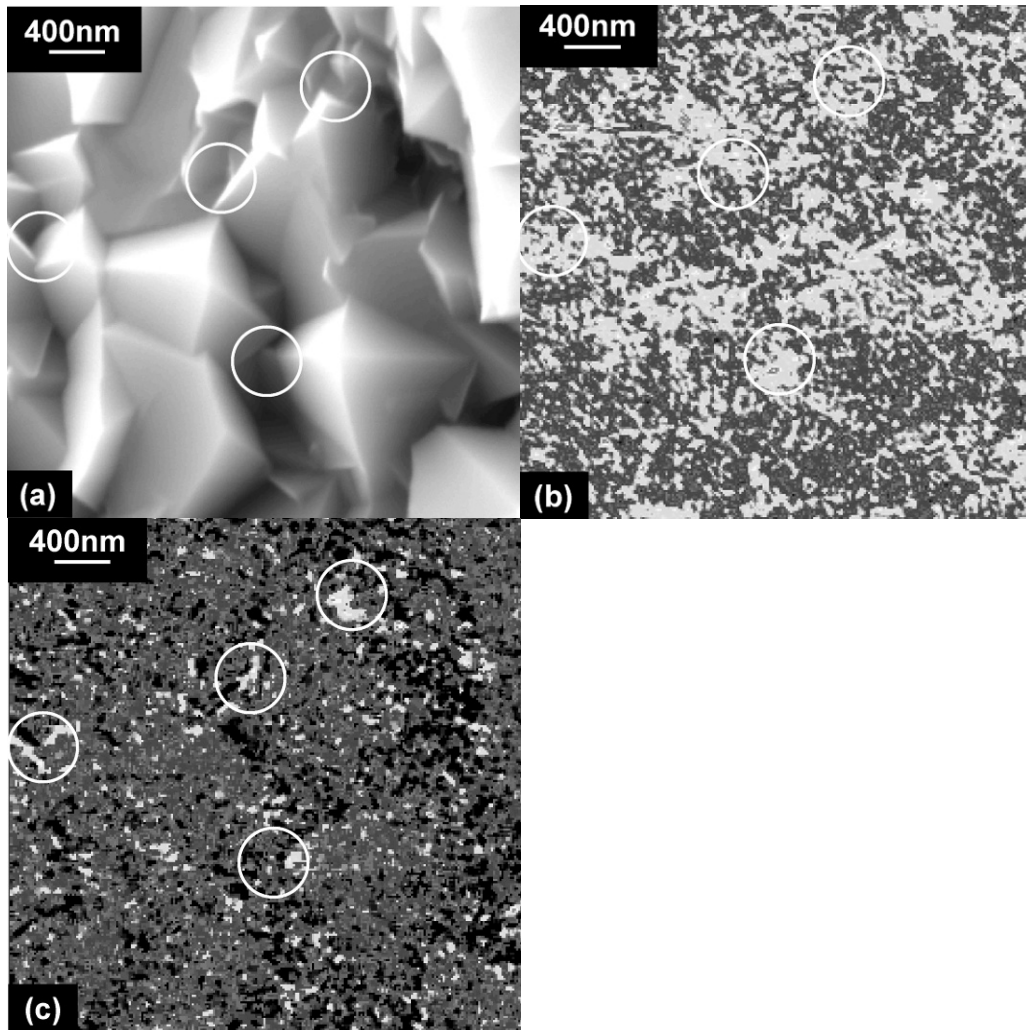


Figure 3-9 SE image (a) and corresponding La (b) and S (c) Auger electron maps for Ni/LaCrO₃-coated AISI 430 steel, oxidized for 2040 hours in air at 800°C.

The “sulfur effect” theory proposed by Lees [17] explains the reactive element and oxide dispersion influence on oxidation resistance enhancement for high-temperature alloys. According to this theory, the impurity S has two detrimental effects on oxidation resistance. The first effect is that S tends to segregate to oxide grain boundaries and enhance cation migration, while it has almost no effect on oxygen transport. The second effect is that S segregates to the metal-oxide interface and reduces scale adhesion dramatically, causing buckling of the scale.

According to the “sulfur effect” hypothesis, finely dispersed oxide particles (both reactive oxides and other stable oxides) in the alloy adsorb a large portion of impurity sulfur and eliminate its detrimental effects.

According to Pint’s “dynamic-segregation” theory [5], reactive elements have a strong affinity for oxygen. Due to this driving force, reactive elements tend to migrate to the scale surface where the activity of oxygen is higher than that in the scale and the substrate. Reactive ions diffuse through oxide grain boundaries, which are rapid diffusion pathways. Because of their large ionic radii, reactive ions tend to segregate to oxide grain boundaries during their migration. Such segregation of reactive ions at the grain boundaries blocks paths for cation outward diffusion. This reduces the scale growth rate and grain size and changes the oxide formation mechanism from being predominantly cation outward diffusion to oxygen anion inward diffusion.

Since S was detected along with La on the oxide surface, it is evident that relatively large ($\sim 1 \mu\text{m}$) dispersed LaCrO_3 particles are not able to adsorb the S impurities to a great extent. This is consistent with Wright et al. [18, 19], who suggest that coarse oxide dispersions do not provide a large enough metal-oxide interface area to effectively adsorb S.

Sulfur facilitates cation outward migration [17], while La reduces cation diffusion rates due to its blocking of the rapid diffusion paths [5]. Sulfur, in this work, is always associated with La in the oxide scale. Therefore, S cannot promote cation diffusion when La blocks the cation diffusion paths. It is proposed that La supplied by LaCrO_3 particles reduces the deleterious effect of S on oxidation resistance. Also, by blocking the diffusion paths, the addition of La changes the oxidation mechanism from a predominantly outward cation diffusion process to an inward anion diffusion process resulting in better adhesion of the scale.

3.3.3 Area specific resistance (ASR)

A major objective of this work is to enhance the high-temperature electronic conductivity of AISI 430 stainless steel interconnects.

Figure 3-10 shows the area specific resistance (ASR) of uncoated and Ni/LaCrO₃-coated AISI 430 stainless steels at 800°C, as a function of time. The ASR profile for uncoated AISI 430 shows a parabolic trend which approaches 0.035 Ωcm² after 250 hours. For the Ni/LaCrO₃-coated AISI 430, the ASR value does not exceed 0.005 Ωcm² after 400 hours. This value is considerably smaller than that for the uncoated AISI 430 steel.

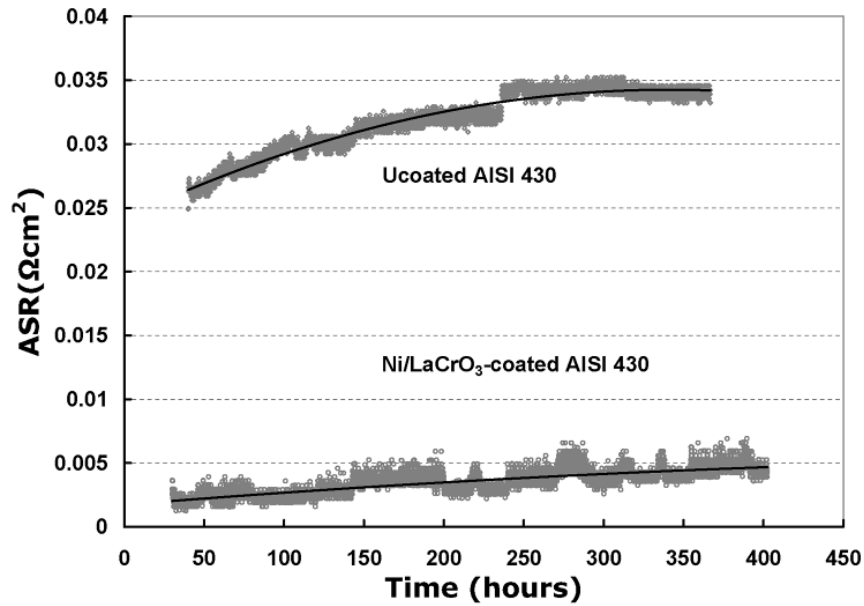


Figure 3-10 Measured ASR values for Ni/LaCrO₃-coated and uncoated AISI 430 stainless steel at 800°C in air as a function of time.

The oxide scale that has formed on uncoated AISI 430, after 170 hours of oxidation at 800°C in air, is ~1 μm thick and consists of a chromia-rich subscale and a (Mn,Cr)₃O₄ spinel outer scale. A thin, continuous layer of silica forms beneath the chromia-rich subscale. The oxide scale grows to a thickness of ~2 μm

after 2040 hours of oxidation. Figure 3-11 shows a region beneath some buckled scale on an AISI 430 specimen, oxidized for 170 hours in air at 800°C. Underneath the scale are several ~20 μm wide or larger cavities. These cavities lead to the formation of gaps between the scale and the substrate. Cavity formation is attributed to outward diffusion of cations (i.e., Cr cations) from the grain boundaries of the alloy surface during oxidation. This hypothesis was confirmed by Auger electron spectra taken from the cavities and substrate surface underneath the scale (Figure 3-12). Figure 3-12(a) shows a spectrum from the surface of a cavity. Only oxide forming/diffusing elements, Cr and Si, in addition to weak signals for Fe were detected on the surface. The spectrum from the substrate surface underneath the cavity (Figure 3-12(b)) shows the presence of bulk steel components, Fe and Cr. Oxygen and C are also present and are considered as common contaminants.

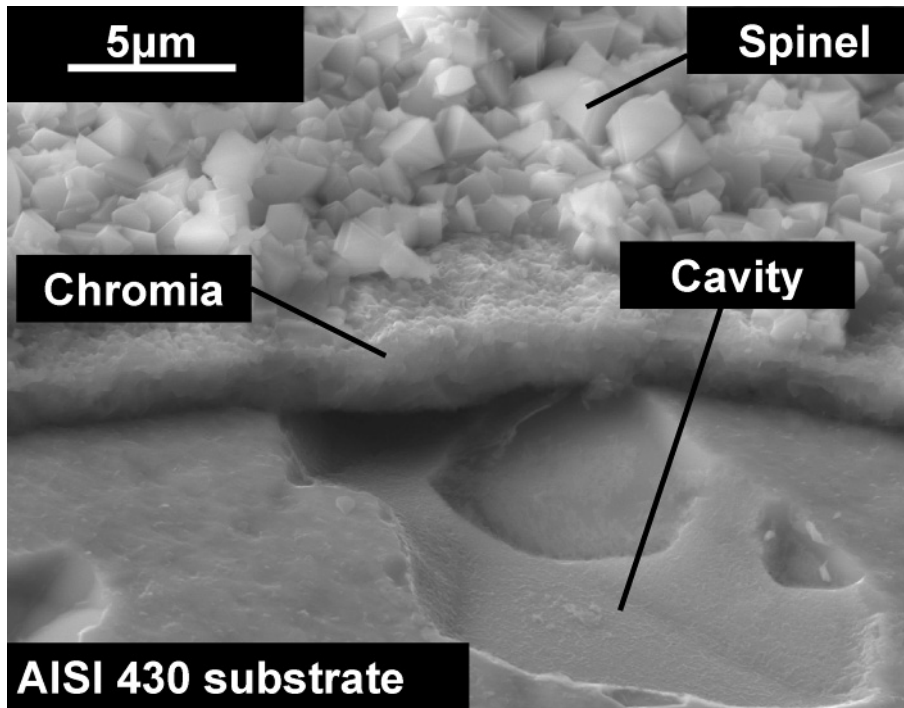


Figure 3-11 SEM secondary electron (SE) image of a spalled area on an AISI 430 stainless steel oxidized for 170 hours in air at 800°C. The specimen was tilted 40°.

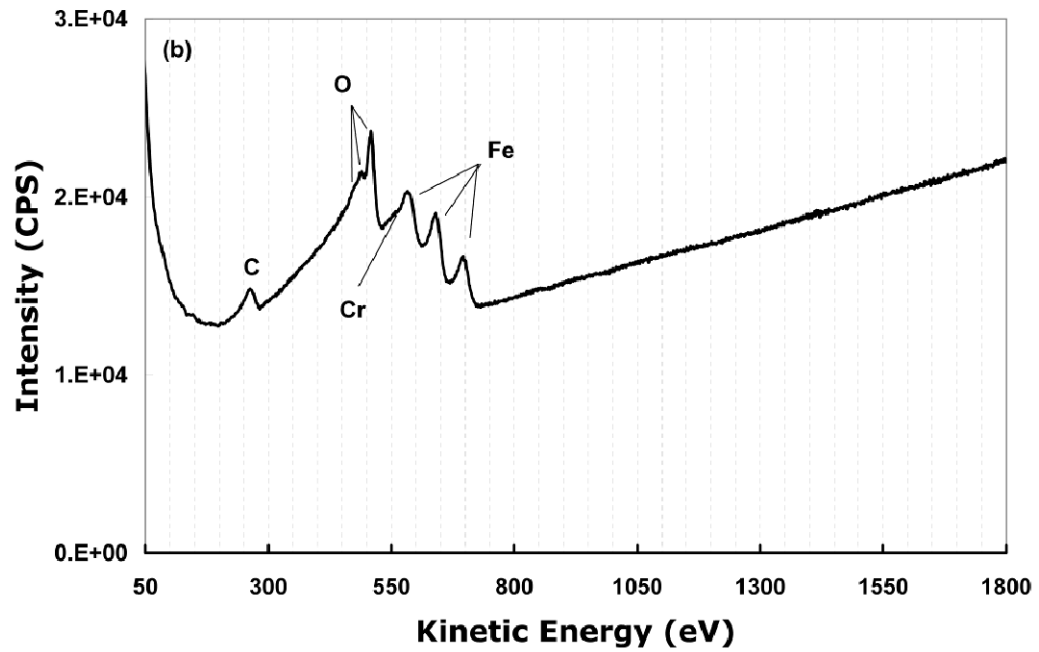
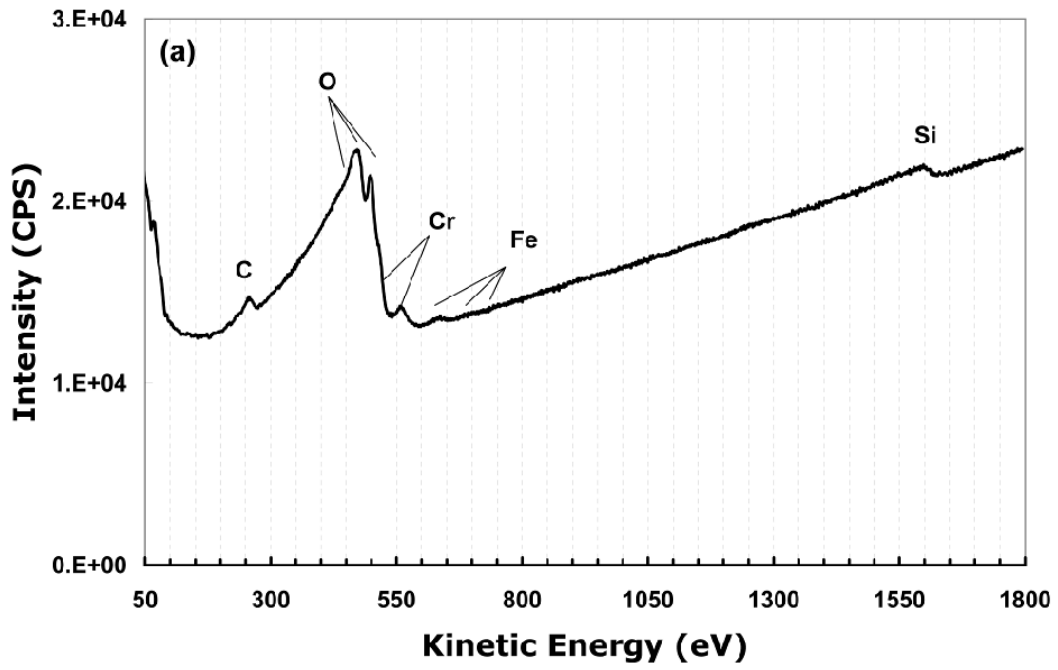


Figure 3-12 Auger electron spectra of (a) cavity and (b) substrate surface shown in Figure 3-11.

The formation of these cavities reduces the actual contact surface area between the alloy and scale. This leads to a higher ASR value, which is the product of the resistance and the nominal contact surface area of the scale and alloy. It is clear that changing the oxidation mechanism from outward cation diffusion to inward oxygen anion diffusion eliminates or reduces the formation of these cavities, which decrease the actual contact area between the scale and substrate resulting in large ASR values. No spallation or formation of cavities is observed for Ni/LaCrO₃-coated steels.

In addition to elimination or reduction of the diffusion cavities beneath the scale, the significantly reduced ASR by application of Ni/LaCrO₃ coatings can be attributed to the presence of conductive LaCrO₃ particles in the chromia-rich subscale and good scale adhesion. However, the electronic conductivity of the chromia scale itself is not possible (or, at least, not easy) to calculate or measure, due to the resistance contributions from the imperfect alloy-scale interface where an insulating SiO₂ layer is also detected (Figure 3-4).

3.4 Conclusions

1. The oxide scale, which forms on the surface of Ni/LaCrO₃-coated AISI 430 stainless steels, consists of a subscale of LaCrO₃ particle filled and adherent chromia and an outer scale composed of a Ni/Fe-rich complex spinel (containing Mn and Cr) as well as NiO.
2. No buckling of the scale, which occurs for uncoated AISI 430 steels, was observed for oxidized Ni/LaCrO₃-coated AISI 430 stainless steels even during air cooling from 800°C.
3. Oxidation resistance has been greatly improved by the addition of LaCrO₃ particles to Ni coatings, due in part to the reduction by La of the deleterious effects of the impurity S in the steel.
4. Cavities form as the result of grain boundary outward migration of cations during oxidation of uncoated AISI 430 stainless steels. The formation of

these cavities reduces the actual contact area between the scale and alloy, resulting in high ASR values.

5. A stable low ASR value ($0.005 \Omega\text{cm}^2$ after 400 hours at 800°C) was obtained for Ni/LaCrO₃ coatings.

In the next chapter oxidation and electrical behavior of an alternative composite coating will be discussed. Nickel as the metal matrix can be replaced with Co, which is believed to form highly conductive oxides.

3.5 References

1. M. L. Keith, *Phase Diagrams for Ceramists*, the American Ceramic Society (1964).
2. Z. Yang, *International Materials Review*, **53**, 39_54 (2008).
3. L. Cooper, *MSc Thesis*, University of Alberta, Edmonton (2007).
4. L. Cooper, S. Benhaddad, A. Wood and D. G. Ivey, *Journal of Power Sources*, **184**, 220 (2008).
5. B. A. Pint, *Oxidation of Metals*, **45**, 1 (1996).
6. B. A. Pint, in *John Stringer Symposium on High Temperature Corrosion*, P. F. Tortorelli, I. G. Wright and P. Y. Hou Editors, p. 9, Materials Park, Ohio (2003).
7. D. P. Whittle, M. E. Eldahshan and J. Stringer, *Corrosion Science*, **17**, 879 (1977).
8. D. P. Whittle and J. Stringer, *Philosophical Transactions of the Royal Society of London Series a-Mathematical Physical and Engineering Sciences*, **295**, 309 (1980).
9. I. M. Allam, D. P. Whittle and J. Stringer, *Oxidation of Metals*, **12**, 35 (1978).
10. B. A. Pint, *Oxidation of Metals*, **48**, 303 (1997).
11. B. A. Pint, *Materials Science Forum*, **251-4**, 397 (1997).
12. B. A. Pint, *Journal of the American Ceramic Society*, **86**, 686 (2003).

13. B. A. Pint, K. L. More and I. G. Wright, *Materials at High Temperatures*, **20**, 375 (2003).
14. J. G. Smeggil, *Materials Science and Engineering*, **87**, 261 (1987).
15. J. G. Smeggil, *Journal of Metals*, **40**, 85 (1988).
16. J. G. Smeggil, A. W. Funkenbusch and N. S. Bornstein, *Metallurgical Transactions a-Physical Metallurgy and Materials Science*, **17**, 923 (1986).
17. D. G. Lees, *Proceedings of the Royal Society of London Series a-Mathematical Physical and Engineering Sciences*, **459**, 1459 (2003).
18. I. G. Wright and B. A. Wilcox, *Oxidation of Metals*, **8**, 283 (1974).
19. I. G. Wright, B. A. Wilcox and R. I. Jaffee, *Oxidation of Metals*, **9**, 275 (1975).

4 Co/LaCrO₃ Composite Coatings for AISI 430 Stainless Steel SOFC Interconnects

4.1 Introduction

In the work presented in Chapters 2 and 3, the electrodeposition technique and oxidation behavior and electronic conductivity of an electrodeposited composite coating of LaCrO₃ particles in a Ni matrix has been studied. A double-layer scale consisting of a particle filled chromia-rich subscale and an outer layer composed a Ni-Fe mixed spinel (containing Mn and Cr), together with NiO, forms as the result of oxidation in air at 800°C. The addition of reactive element containing oxide particles, LaCrO₃, greatly improves the oxidation resistance of coated, oxidized AISI 430 steels. Excellent electronic conductivity (ASR \approx 0.005 Ωcm^2 after 400 hours of oxidation), good adhesion of the scale and elimination of scale buckling were achieved with this coating system. It has been reported in the literature that Co containing spinels are more conductive than their Ni containing counterparts [1, 2]. Therefore, in order to further improve the electronic conductivity, Ni has been replaced with Co in this portion of the study. The present work emphasizes evaluation of the oxidation behavior and electrical properties of electrodeposited composite Co/LaCrO₃ coatings applied to AISI 430 ferritic stainless steel substrates.

4.2 Experimental methods

Coupons of AISI 430 stainless steel (measuring 20 mm \times 10 mm \times 1 mm) were coated with a composite layer of LaCrO₃ particles in a Co matrix. The coatings were applied via electroplating in an all-sulfate cobalt plating bath; the composition and operating conditions are shown in Table 4-1. The plating bath contained 35 gL⁻¹ suspended LaCrO₃ particles*. The cathode and anode were placed horizontally in the plating beaker with the cathode substrate surface facing up. Prior to composite Co/LaCrO₃ coating, the specimens were anodically

* For particle size information see **Figure 2-2**

activated to remove the passive film on the stainless steel and coated with a thin layer of cobalt (strike plating). The solution composition and conditions for activation/Co strike plating are listed in Table 4-2. Specimens were ultrasonically cleaned in an alkaline solution prior to activation and after electrodeposition.

Table 4-1 Composition and operating conditions for Co/LaCrO₃ composite electroplating

Cobalt sulfate, heptahydrate (CoSO ₄ ·7H ₂ O)	450 gL ⁻¹ (1.6 M)
Boric acid (H ₃ BO ₄)	40 gL ⁻¹ (0.6 M)
Sodium dodecyl sulfate (SDS) (NaC ₁₂ H ₂₅ SO ₄)	0.1 gL ⁻¹ (0.3 mM)
Lanthanum chromite (LaCrO ₃), Temperature	35 gL ⁻¹ 40±2 °C
pH	~4, (adjusted with NaOH and/or H ₂ SO ₄)
Agitation	Magnetic bar from the bottom (600 rpm)
Current Density	45 mA.cm ⁻² , DC
Anode	Commercially pure Co rod
Time (Thickness)	7 min (4-5µm)

Table 4-2 Composition and operating conditions of activation/Co strike plating

Cobalt chloride, hexahydrate (CoCl ₂ ·6H ₂ O)	100 gL ⁻¹ (0.42 M)
Hydrochloric acid (HCl, 37 vol%)	85 mL ⁻¹ (1 M)
Anodic activation	2 minutes, 22 mA.cm ⁻²
Cathodic cobalt strike	6 minutes, 22 mA.cm ⁻²
Temperature	20 °C
Anode	Commercially pure Co rod

Oxidation tests were performed for coated samples in static air at 800°C for various time periods and up to 2040 hours.

The cross sectional sample preparation technique has been discussed in detail in Section 2.2 of this thesis. The SEM used for the purpose of imaging and chemical microanalysis was a Hitachi H2700 SEM equipped with a Princeton Gamma-Tech (Prism IG) ultra thin window (UTW) (EDX) spectrometer. Particle volume fraction of the coatings was determined by means of image analysis software, Image-Pro® Version 6. Phase identification for coated, oxidized specimens was performed by glancing angle X-ray diffraction employing a Rigaku Geigerflex 2173 rotating anode instrument. The anode used for XRD was cobalt with CoK_α radiation with a wavelength of $\lambda = 0.1789$ nm. The incident beam angle was $\theta = 5^\circ$ and the approximate penetration depth was 15 μm . Depth profiling for oxidized Co/LaCrO₃-coated specimens was performed by means of SIMS. An Ion-ToF SIMS IV instrument was employed for this purpose. Specimens were sputtered with Cs⁺ ions at 1 keV and 250 nA. The sputtering area was 200 × 200 μm . Ga⁺ ion sputtering at 15 keV over an area of 34 × 34 μm was used for analysis. All oxidation tests were performed in air at 800°C. The specific weight gains for the oxidized samples were conducted according to the method described in section 2.2 of this thesis.

The area specific resistance (ASR) of the oxidized Co/LaCrO₃-coated and uncoated specimens were measured at 800°C in air according to the method described in section 3.2 of this thesis.

4.3 Results and Discussion

4.3.1 As-deposited composite Co/LaCrO₃ coating

Figure 4-1(a) and (b) illustrate the as-deposited coating surface and cross sectional structure. Uniform embedding of LaCrO₃ particles in the Co matrix is seen. The coating has a uniform thickness and exhibits good adhesion to the substrate. These

samples were prepared according to the conditions described in Table 4-3. Image analysis from the plan view image (Figure 2a), shows ~20 vol.% of embedded particles in the coating.

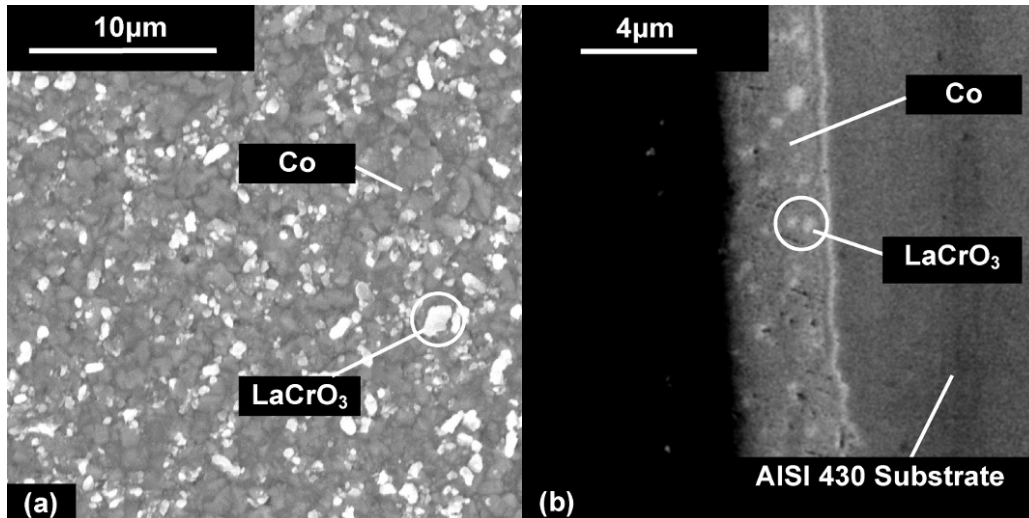


Figure 4-1 SEM images of the as-deposited Co/LaCrO₃-coating; (a) surface secondary electron (SE) and (b) cross sectional backscattered electron (BSE) image.

4.3.2 Oxide scale structure and morphology

Surface and cross sectional SEM images of Co/LaCrO₃-coated AISI 430 stainless steel coupons oxidized for 170 and 2040 hours at 800°C are illustrated in Figure 4-2. A nodular surface morphology with uniform-size oxide particles is observed on the surface of both oxidized specimens (Figure 4-2(a) and (c)). Some porosity is seen on the oxide surfaces. The cross sectional backscattered electron (BSE) images (Figure 4-2(b) and (d)) show three different layers in the scale. Some porosity is also present at the scale-metal interface for the sample oxidized for 2040 hours (Figure 4-2(d)). The EDX results from the numbered regions in Figure 4-2(b) and (d) are listed in Table 4-3.

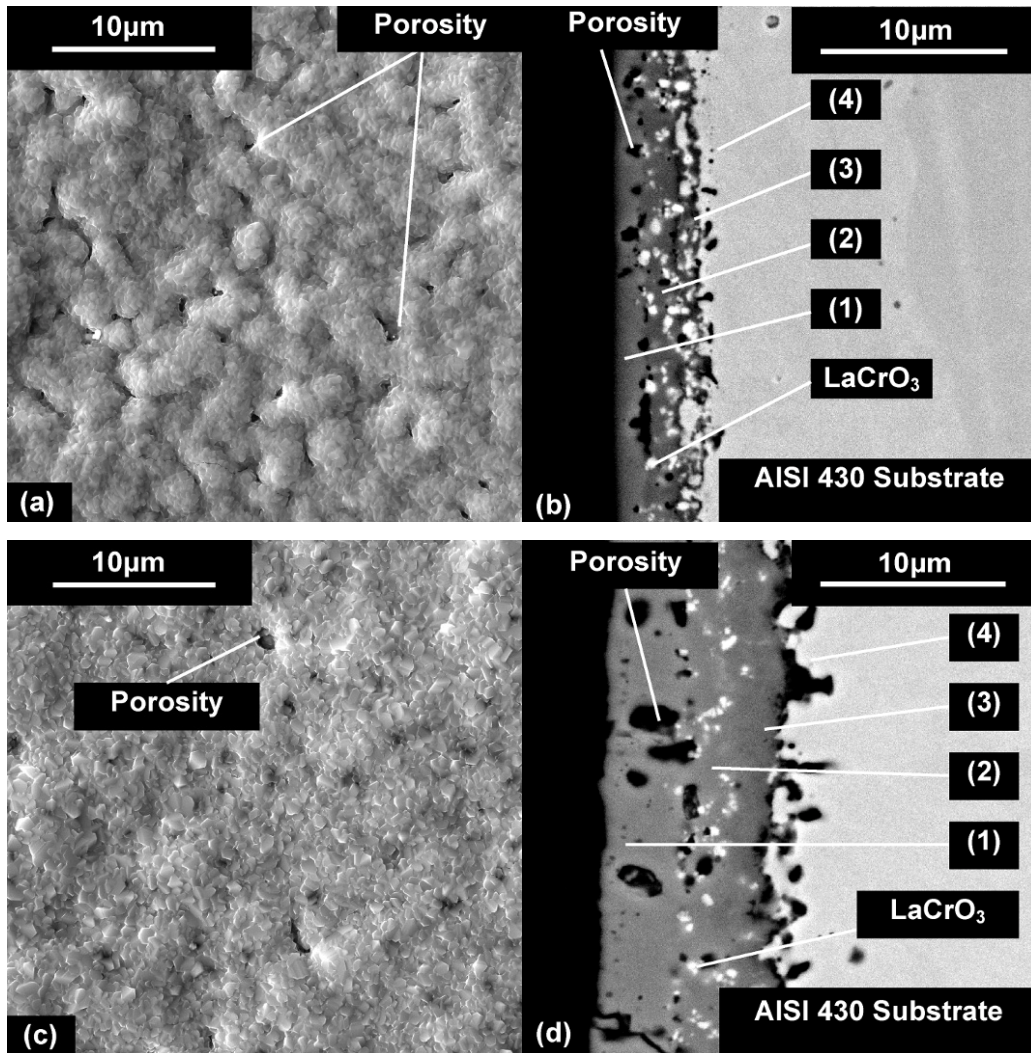


Figure 4-2 SEM images of oxidized Co/LaCrO₃ coatings: (a) and (b) after 170 hours; (c) and (d) after 2040 hours of oxidation in air at 800°C. (a) and (c) are surface SE images; (b) and (d) are cross sectional BSE images.

Table 4-3 Chemical composition (wt.%) and phases for the numbered regions in **Figure 4-2(b)** and (d) as determined by EDX/XRD analysis.

Regions (points)	Phase	(170 h, Figure 4-2(b))				(2040 h, Figure 4-2(d))			
		Fe	Co	Cr	Mn	Fe	Co	Cr	Mn
(1)	Co ₃ O ₄ spinel	8	91	1	0	3	96	1	0
(2)	(Co,Fe) ₃ O ₄ spinel	48	49	2	1	34	61	2	1
(3)	Chromia-rich	29	21	48	2	2	26	65	3
(4)	α-Fe-Cr-Co	64	25	10	1	84	2	13	1

Oxygen levels are not shown.

Glancing angle X-ray diffraction patterns were also obtained to identify the phases in the oxide scales for the samples oxidized for 170 and 2040 hours. The XRD patterns are shown in Figure 4-3. The three layers of the scale have been identified to be FCC-spinel Co₃O₄ (JCPDS file: 65-3103 [3]), containing Fe and a small amount of Cr, as the outer layer, (Co,Fe)₃O₄ FCC-spinel (closely matching CoFe₂O₄, JCPDS file: 03-0864 [3]), containing small amounts of Cr and Mn, as the mid layer, and a LaCrO₃ (JCPDS file: 33-0701 [3]) particle filled chromia-rich (JCPDS file: 38-1479 [3]) layer, also containing Co, Fe and Mn, as the inner layer. The peaks corresponding to the chromia-rich phase are not very intense for the sample oxidized for 2040 hours. This is due to the increased thickness of the scale which limits penetration of the incident X-rays to the chromia layer. The thickness of the chromia-rich scale after 2040 hours of oxidation is ~2μm.

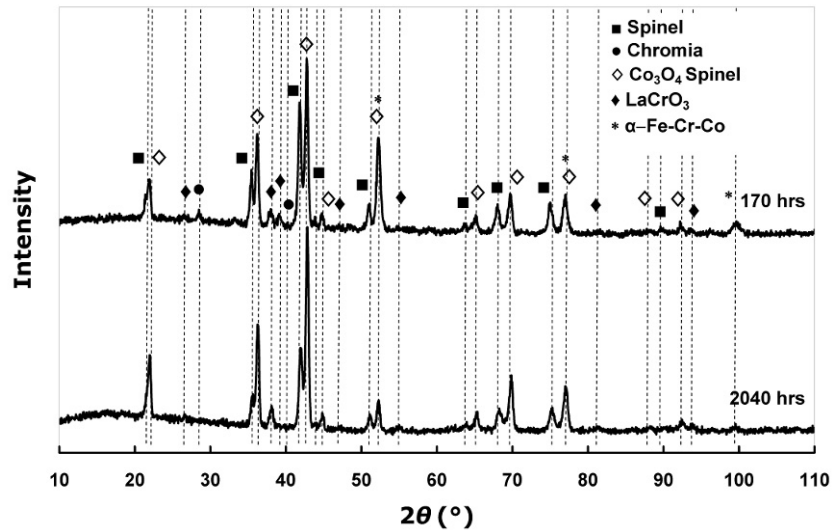


Figure 4-3 XRD patterns for Co/LaCrO₃-coated specimens oxidized for 170 and 2040 hours. The peaks labelled spinel are (Fe,Co)₃O₄ spinel.

4.3.3 SIMS depth profiles

The distribution of metallic elements throughout the scale was analyzed by means of SIMS depth profiling. Depth profiles for Co/LaCrO₃-coated specimens oxidized for 170 and 2040 hours are shown in Figure 4-4(a) and (b), respectively. Intensity profiles for Cr show a maximum in the inner scale for both samples. The Cr intensity in the outer scale is small even for the sample oxidized for 2040 hours. The Cr intensity increase at the outside surface is due to a faster ionization rate of Cr from the scale surface during depth profiling and is an artefact. This indicates that Cr migration to the scale surface has been effectively reduced. The intensity profiles for Fe and Co exhibit a similar increase in the mid-spinel layer where Mn also exhibits an increase. The major element contributing to the outer scale is Co. Small amounts of Fe and Cr are also present in the outer layer as they were detected by EDX (regions (1) in Table 4-3). Diffusion of Mn through the inner layer into the mid layer is seen in Figure 4-4(a) and (b). Lanthanum exists in the entire oxide scale with a very small concentration in the outer Co₃O₄ layer. Segregation of Si (likely as SiO₂) underneath the chromia-rich inner scale is

apparent, particularly in Figure 4-4(b). The porosity at the scale-metal interface (Figure 4-2(d)) may have formed due to the formation of a silica network. Silica is not miscible with chromia, and the poor adhesion between the oxides may cause detachment of chromia from silica, which is adherent to the substrate, during the development of thermal stresses. Stainless steel substrates with smaller Si content may be more promising.

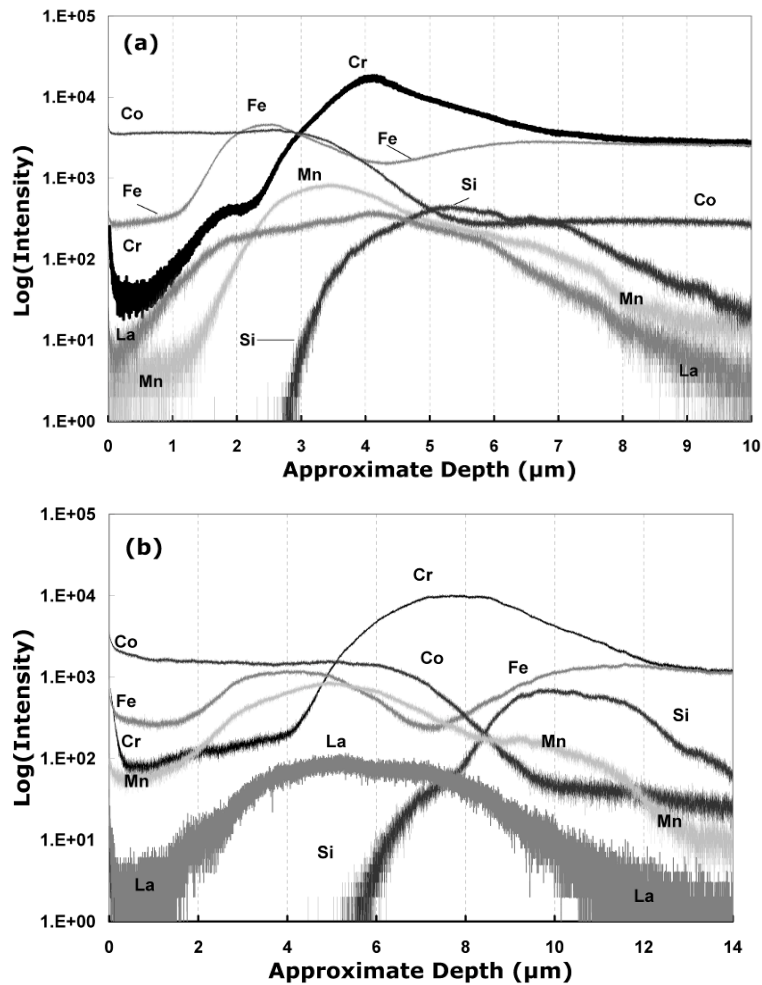


Figure 4-4 SIMS depth profiles for oxidized Co/LaCrO₃-coated specimens for (a) 170 and (b) 2040 hours of oxidation.

4.3.4 Effect of LaCrO₃ particles

In order to investigate the effect of LaCrO₃ particle addition on the oxidation behaviour of coated steels, substrates of AISI 430 steel were coated with pure Co to the same thickness as the composite Co/LaCrO₃ coatings (~4-5 μm) and oxidized under identical conditions. For these samples, however, the scale partially spalled off after ~1200 hours of oxidation. Figure 4-5 illustrates the specific weight gains as a function of time for oxidized uncoated, Co-coated and Co/LaCrO₃-coated steel coupons. For the coated samples, the initial oxidation rate is considerably higher than that for uncoated samples. This is due to rapid oxidation of Co in the coatings. After ~100 hours of oxidation, however, the Co/LaCrO₃-coated samples show similar oxidation kinetics to the uncoated steels. The Co-coated specimens exhibit a higher oxidation rate in comparison with the Co/LaCrO₃-coated coupons.

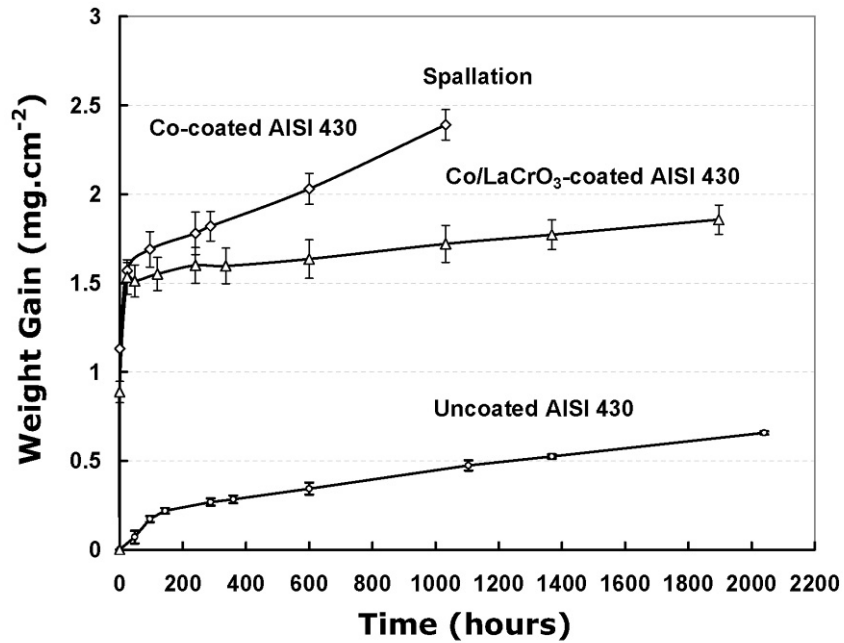


Figure 4-5 Specific weight gains for oxidized Co/LaCrO₃-coated, Co-coated and uncoated AISI 430 coupons as a function of oxidation time.

Figure 4-6(a) and (b) show the surface and cross sectional SEM images of Co-coated samples oxidized for 170 hours. The scale structure is similar to that which grows on Co/LaCrO₃-coated samples, except that in this case the scale is thicker and no particles are present. The scale is composed of three visible layers which are numbered on the images. Table 4-4 shows the composition and phases present in the scale, determined by EDX and XRD analysis. The three layers in the scale are a chromia-rich inner layer, a mixed Co-Fe-Cr spinel midlayer and a Co₃O₄ outer layer. Figure 4-6(c) and (d) depict the oxide scale after 1200 hours of oxidation. The cross sectional image (Figure 4-6(d)) shows a thick scale consisting of a thick, non-adherent chromia-rich layer covered by two porous outer layers. The composition and structure of the layers are also listed in Table 4-4. Figure 4-6(c) shows a spalled area of the scale; underneath the scale are isolated, dark islands of silica, as determined by EDX analysis. Since silica is not entirely removed by the spalled scale (Figure 4-6(c)), there is inadequate adhesion between chromia and silica (silica is not miscible with chromia). This poor adhesion and formation of a silica network at the alloy-scale interface may be a reason for spallation of the scale.

For uncoated AISI 430, the oxide scale consists of a chromia-rich subscale covered by a Mn-Cr spinel layer. A thin layer of silica also forms beneath the chromia-rich layer. After 170 hours of oxidation at 800°C in air, the scale is ~1 μm thick and grows to a thickness of ~2 μm after 2040 hours of oxidation.

The addition of LaCrO₃ particles to the coating not only decreases the oxidation rate but also eliminates scale spallation. The mechanisms through which LaCrO₃ particles enhance the oxidation properties of the coating are not clear for this case. A similar effect has been observed for Ni/LaCrO₃ coatings developed for stainless steel interconnects and studied in the Chapter 3. The beneficial effects and mechanisms of oxidation resistance improvement of reactive elements have been reviewed by Whittle and Stringer [6] and discussed by many other studies [e.g., 4-33].

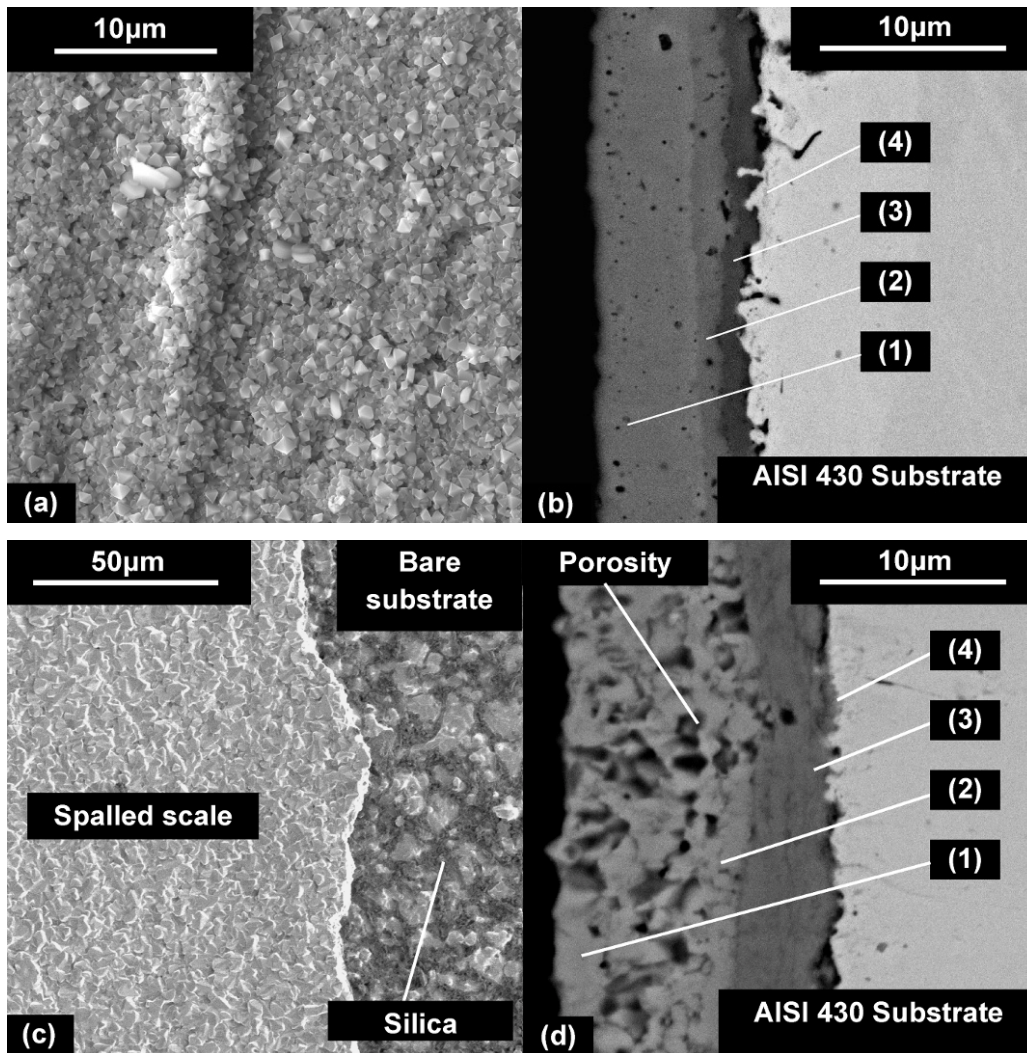


Figure 4-6 SEM images of oxidized Co coatings: (a) and (b) after 170 hours; (c) and (d) after 1200 hours of oxidation in air at 800°C. (a) and (c) are surface SE images; (b) and (d) are cross sectional BSE images.

Table 4-4 Chemical composition (wt.%) and phases for the numbered regions in **Figure 4-6(b)** and (d) as determined by EDX/XRD analysis

Regions (points)	Phase Structure	(170 h, Figure 4-6(b))				(1200 h, Figure 4-6(d))			
		Fe	Co	Cr	Mn	Fe	Co	Cr	Mn
(1)	Co ₃ O ₄ spinel	8	90	1	1	11	80	1	1
(2)	(Co,Fe) ₃ O ₄ spinel	42	50	6	2	44	46	6	4
(3)	Chromia-rich	6	2	90	2	2	2	93	2
(4)	α-Fe-Cr-Co	81	8	11	1	82	6	11	1

Oxygen levels are not shown.

4.3.5 Area specific resistance

The ASR for Co/LaCrO₃-coated and uncoated AISI 430 stainless steels, as a function of time, is plotted in Figure 8. ASR values for uncoated AISI 430 increase rapidly with oxidation time for up to ~50 hours and approach a constant value of 0.035 Ωcm² after ~250 hours with a parabolic trend. Co/LaCrO₃-coated specimens, however, show a very low resistance (ASR < 0.005 Ωcm²) for up to ~165 hours of oxidation. The ASR starts to increase parabolically after this point and approaches a constant value of ~0.02 Ωcm² after ~600 hours of oxidation. No further increase in ASR for Co/LaCrO₃-coated steels is seen for the test time of 900 hours. The sudden increase in ASR after 160 hours is attributed to the formation of porosity at the metal-scale interface which reduces the actual area of contact between the scale and substrate. This porosity, which is visible in Figure 4-6(d), may be due to outward diffusion of Co. SIMS results (Figure 4-4) show the outward diffusion of Co through the chromia-rich inner layer. The increase in the thickness of the outer layer, which is Co-rich, also suggests that there is outward diffusion of Co through the chromia-rich inner layer. Therefore, the

chromia-rich subscale is not protective enough against the outward diffusion of Co.

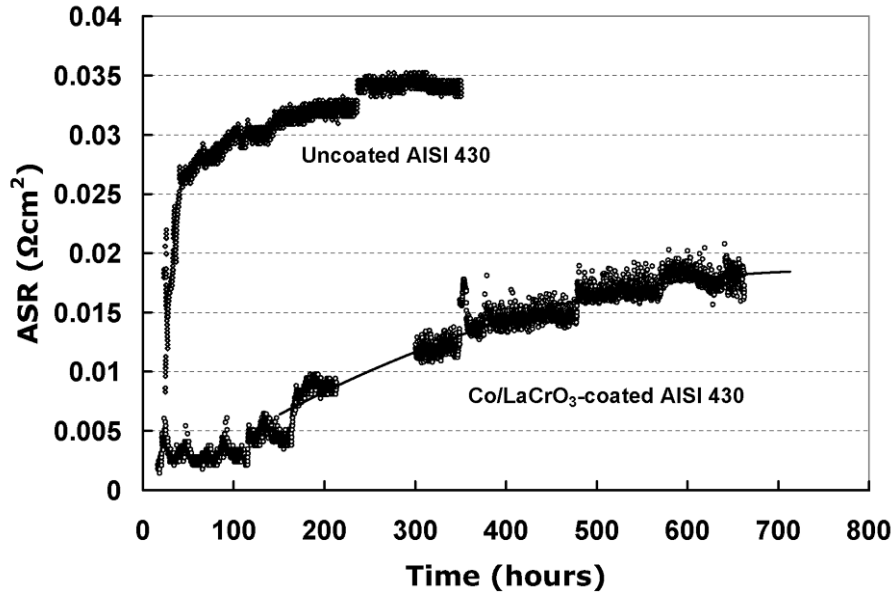


Figure 4-7 ASR values for Co/LaCrO₃-coated and uncoated AISI 430 stainless steel at 800°C in air as a function of time.

Several factors can contribute to the improved electrical conductivity for the Co/LaCrO₃-coated steels over uncoated AISI 430 steels. These include the higher electronic conductivity of the scale consisting of Co containing spinel layers, the presence of conductive perovskite LaCrO₃ particles in the oxide scale, improved adhesion of the scale to the substrate and elimination of scale spallation.

4.4 Conclusions

The application of composite Co/LaCrO₃ coatings for AISI 430 stainless steel was studied as a potential solution to limit chromium migration and increase high-temperature electronic conductivity of the substrate. The scale, which forms on the surface of oxidized Co/LaCrO₃-coated AISI 430 at 800°C in air, consists of two layers of cobalt containing spinel, a Co-Fe spinel as the mid layer, Co₃O₄ as

the top layer and a chromia-rich inner layer. The mid and inner layers of the scale contain LaCrO_3 particles. The coating limits the diffusion of Cr into the scale surface to less than 1 wt.% Cr after 2040 hours of oxidation. The addition of LaCrO_3 particles not only improves the oxidation resistance of the coating but also eliminates scale spallation. The ASR of Co/ LaCrO_3 -coated AISI 430 steels does not exceed $\sim 0.02 \text{ } \Omega\text{cm}^2$ after 900 hours at 800°C in air. Silica networks, which form at the metal-scale interface, result in spallation of scale in Co-coated steels and pore formation in Co/ LaCrO_3 -coated specimens. This may be a problem for long-term service. A low silicon grade substrate may be more suitable for Co/ LaCrO_3 coatings.

4.5 References

1. W. Qu, L. Jian, J. M. Hill and D. G. Ivey, *Journal of Power Sources*, **153**, 114 (2006).
2. A. Petric and H. Ling, *Journal of the American Ceramic Society*, **90**, 1515 (2007).
3. JCPDS in, International Center for Diffraction Data, Newtown Square, PA (1996).
4. D. P. Whittle and J. Stringer, *Philosophical Transactions of the Royal Society of London Series a-Mathematical Physical and Engineering Sciences*, **295**, 309 (1980).
5. I. M. Allam, D. P. Whittle and J. Stringer, *Oxidation of Metals*, **12**, 35 (1978).
6. S. Chevalier and J. P. Larpin, *Materials Science and Engineering a-Structural Materials Properties Microstructure and Processing*, **363**, 116 (2003).
7. S. Chevalier, C. Nivot and J. P. Larpin, *Oxidation of Metals*, **61**, 195 (2004).

8. S. Chevalier, C. Valot, G. Bonnet, J. C. Colson and J. P. Larpin, *Materials Science and Engineering a-Structural Materials Properties Microstructure and Processing*, **343**, 257 (2003).
9. P. Y. Hou, Z. R. Shui, G. Y. Chuang and J. Stringer, *Journal of the Electrochemical Society*, **139**, 1119 (1992).
10. P. Y. Hou and J. Stringer, *Journal of the Electrochemical Society*, **132**, C362 (1985).
11. P. Y. Hou and J. Stringer, *Journal of the Electrochemical Society*, **134**, 1836 (1987).
12. P. Y. Hou and J. Stringer, in, p. 231 (1993).
13. P. Y. Hou and J. Stringer, *Materials Science and Engineering a-Structural Materials Properties Microstructure and Processing*, **202**, 1 (1995).
14. D. G. Lees, *Oxidation of Metals*, **27**, 75 (1987).
15. B. A. Pint, *Materials Science Forum*, **251-4**, 397 (1997).
16. B. A. Pint, *Journal of the American Ceramic Society*, **86**, 686 (2003).
17. B. A. Pint, in *John Stringer Symposium on High Temperature Corrosion*, I. G. W. P. F. Tortorelli, and P. Y. Hou Editor, p. 9, Materials Park, OH (2003).
18. B. A. Pint, K. L. More and I. G. Wright, *Materials at High Temperatures*, **20**, 375 (2003).
19. B. A. Pint and J. H. Schneibel, *Scripta Materialia*, **53**, 379 (2005).
20. J. G. Smeggil, A. W. Funkenbusch and N. S. Bornstein, *Metallurgical Transactions a-Physical Metallurgy and Materials Science*, **17**, 923 (1986).
21. J. G. Smeggil and A. Rotunno, *Journal of the Electrochemical Society*, **133**, C117 (1986).
22. A. Strawbridge and P. Y. Hou, in, p. 177 (1994).
23. I. M. Allam, D. P. Whittle and J. Stringer, *Oxidation of Metals*, **13**, 381 (1979).
24. O. T. Goncel, J. Stringer and D. P. Whittle, *Corrosion Science*, **18**, 701 (1978).

25. O. T. Goncel, D. P. Whittle and J. Stringer, *Journal of the Electrochemical Society*, **125**, C113 (1978).
26. O. T. Goncel, D. P. Whittle and J. Stringer, *Corrosion Science*, **19**, 305 (1979).
27. O. T. Goncel, D. P. Whittle and J. Stringer, *Oxidation of Metals*, **15**, 287 (1981).
28. J. Stringer, I. M. Allam and D. P. Whittle, *Thin Solid Films*, **45**, 377 (1977).
29. J. Stringer, V. Nagarajan and D. P. Whittle, *Journal of the Electrochemical Society*, **124**, C316 (1977).
30. D. P. Whittle, M. E. Eldahshan and J. Stringer, *Corrosion Science*, **17**, 879 (1977).
31. W. Dong, H. E. Bishop, D. Johnson, D. G. Lees and G. W. Lorimer, *Oxidation of Metals*, **54**, 509 (2000).
32. D. G. Lees, *Proceedings of the Royal Society of London Series a-Mathematical Physical and Engineering Sciences*, **459**, 1459 (2003).
33. H. B. Qi and D. G. Lees, *Oxidation of Metals*, **53**, 507 (2000).

5 Metal-Oxide Scale Interfacial Imperfections and Performance of Stainless Steel Interconnects Utilized in Solid Oxide Fuel Cells

5.1 Introduction

As described earlier in Chapter 1, premature degradation of SOFCs using commercial grades of ferritic steel interconnects occurs as the steel oxidizes at the relatively high operating temperatures, especially at the cathode side with an air atmosphere. The thermally grown oxide scale that forms on the surface of most commercially used ferritic stainless steel interconnects consists of three layers including an outer Cr-Mn spinel, an inner chromia-rich layer and a thin layer of amorphous insulating oxides (silica and/or alumina depending on the composition of the substrate) at the metal-oxide scale interface beneath the chromia-rich scale [1-7]. The rapid increase in contact resistance is a crucial problem resulting from oxidation of stainless steel interconnects [8-10]. The increase in contact resistance has been attributed to insufficient oxidation resistance and the relatively high growth rates of the chromia-rich scale [3, 11], as well as the formation of insulating oxides underneath the chromia-rich layer [6, 7, 12].

There are, however, other factors which affect the conductivity of oxidized metallic interconnects. The actual metal-oxide scale contact surface area and metal-to-scale adhesion are critical factors directly influencing the area specific resistance (ASR) of oxidized interconnects.

The objective of this chapter is to study the metal-oxide scale interfacial imperfections which affect the performance of stainless steel interconnects. Two types of stainless steels, AISI-SAE 430 and Hitachi ZMG232, were selected for experiments. AISI-SAE 430 is a low-cost commercial grade containing non-metallic impurities, such as S and P; while ZMG232 is a specialty grade, developed specifically for interconnect applications. This steel contains small

amounts of Zr and La as reactive elements. Electron microscopy as well as surface science analysis techniques were used to study the metal-oxide scale interface. This study suggests that deterioration of the interconnect conductivity is highly dependent on metal-oxide scale interfacial imperfections resulting from the steel composition, rather than the poor conductivity and growth rate of the oxide scales.

5.2 Experimental Methods

5.2.1 Specimens and sample preparation

Two grades of ferritic stainless steel, AISI-SAE 430 and ZMG232 (Hitachi Metals), were utilized. The nominal compositions of these steels are listed in Table 5-1. AISI-SAE 430 contains S and P as impurities in addition to the main alloying elements (i.e., Fe, Cr, Mn, Si and C). ZMG232 contains small amounts of Zr, Ni, Al and La in addition to the main alloying elements. This steel contains lower levels of Si, Mn and C in comparison with AISI-SAE 430. The manufacturer has not reported the presence and amounts of indigenous impurities in ZMG232, such as S and P. This may indicate that the amounts of impurities in this steel are negligible.

The dimensions of coupons cut from as-supplied sheets of ZMG232 were 10 mm × 20 mm × 0.25 mm, while AISI-SAE 430 sheets were cut into 10 mm × 20 mm × 1 mm pieces. Oxidation for the steel coupons was performed in static air at 800°C in an electric box furnace for various time periods. In order to remove any contamination, soap, ultrasonic cleaning in acetone and then rinsing in ethanol and distilled were performed immediately before oxidation.

The metal-oxide scale interface of the aforementioned steels was studied after oxidation. In order to study the surface of the metal and oxide scale sides of the metal-oxide scale interface, the scale was detached from the substrates. For this purpose, a non-oxidized steel coupon with the same dimensions as test specimens

was glued with curable epoxy to the outer scale surface of the steel coupons. The stack was then cured at approximately 160°C in vacuum for 2 h. After cooling, the two steel pieces were mechanically detached from each other. In doing so, some portions of the scale, attached to the non-oxidized coupon, were peeled off and the metallic area underneath was exposed. This allowed simultaneous observation of both the underside of the scale and the exposed metallic surface underneath. Scale detachment was only possible for AISI-SAE 430 oxidized specimens. The scales on ZMG232 samples adhered so well to the substrate that epoxy failure occurred instead of scale detachment.

5.2.2 Analysis methods

SEM as well as surface science analysis techniques, including AES, XPS and SIMS as a means of depth profiling, were used to study the metal-oxide scale interface of the oxidized AISI-SAE 430 steels. Due to impracticality of scale detachment for ZMG 232, only SIMS depth profiling was used for this steel. A JEOL field emission Auger scanning microprobe (JAMP 9500F) was used for both secondary electron (SE) imaging and AES analysis. SE imaging was performed with 25kV accelerating voltage and a working distance of approximately 25 mm. XPS was used to detect and determine the chemical state of the elements on the underside of the scale, as well as the exposed metallic surface. For this purpose, a Kratos Axis 165 XPS system was employed. A monochromatic Al X-ray beam with a $K\alpha$ energy of 1486.6 eV was used for analysis. XPS results were analyzed using Casa software. The instrument used for SIMS depth profiling was a time of flight ION-ToF SIMS IV. Cs^+ and O^{2+} ions were used for sputtering for positive and negative polarities, respectively. The ion beam current used for both positive and negative polarities was approximately 100 nA and the area for sputtering was $200\ \mu m \times 200\ \mu m$. Ga^+ ions with a kinetic energy of 15 keV, over an area of $34\ \mu m \times 34\ \mu m$, were used for analysis. Image analysis software, Image-Pro[®] Version 6, was used to determine the fraction of the surface occupied by interfacial defects.

Table 5-1 Nominal compositions of ferritic stainless steels used in this Chapter

Steel	Composition (wt.%)										
	Cr	Fe	Ni	Mn	Si	C	P	S	Al	Zr	La
AISI-	16-	Bal.	-	1	1	0.12	0.04	0.03	-	-	-
SAE 430	18					max	max	max			
ZMG232	22.0	Bal.	0.26	0.5	0.4	0.02	-	-	0.22	0.22	0.0

4

5.3 Results and discussion

5.3.1 SEM/AES analysis

Coupons of the two steels (ZMG232 and AISI-SAE 430) were oxidized for 170 h in air at 800°C. After oxidation, samples were removed from the furnace (at the furnace temperature) and air-cooled. The purpose of air-cooling was to induce thermal stresses that can lead to spallation of the scale on the areas where scale adhesion is poor. Partial spallation of the scale was observed only for AISI-SAE 430 samples. Scales on ZMG232 samples did not spall.

Similar steel coupons were oxidized for longer times (i.e., 500 h). For these coupons the scale were mechanically detached via the procedure described in the Experimental Methods section. This was performed in order to expose larger areas of the interface at both the metal side and the corresponding underside of the scale. No scale detachment occurred for ZMG232 samples.

Figure 5-1(a) and (b) show a partially spalled scale on AISI-SAE 430 and the exposed, metallic substrate underneath. In Figure 5-1(a), the sample was tilted 40° from the horizontal axis for enhanced observation of the interface. The oxidation time for these coupons was 170 h. Relatively large cavities underneath the spalled scale on the metallic substrate surface are clearly visible. The scale is almost uniform in thickness and is not in contact with the inner surfaces of cavities. The cavities appear as wide, but shallow depressions, under the scale and on the metal

surface. The cavity surfaces are faceted (Figure 5-1(b)) and similar to those reported for alumina forming alloys (e.g., NiAl [13] and FeAl [14]). The facets are likely closely packed crystallographic planes with specific orientations where the surface energy is minimal and in favor of growth. However, the exact orientation of these facets is not clear at this time.

SE images of the exposed metal surface after scale detachment for samples oxidized for 500 h are shown in Figure 5-1(c) and (e), and images of the corresponding detach scale undersides are represented in Figure 5-1(d) and (f). In addition to cavities, some submicron-sized particles are observed on the metal surface of samples oxidized for 500 h (Figure 5-1(c) and (e)). These particles are not detected for the samples oxidized for shorter periods (Figure 5-1(a) and (b)). Some pit-like imprints of the particles are seen on the underside of the detached scale (Figure 5-1(d) and (f)). These imprints represent particle positions prior to scale detachment. The particles do not adhere to the scale, and as a result remain on the metal surface upon scale detachment.

In order to analyze the surface composition of the interface and its possible contribution to the formation of voids, cavities and particles, AES analysis was conducted for both the exposed metal surfaces including cavities and other areas as well as for the corresponding scale undersides. Note that C and O are observed in all Auger spectra. These elements can be adsorbed on the surface of the samples when exposed to the atmosphere. They also can be indigenous parts of the surface composition. Therefore, a definite judgment cannot be made on whether the interface naturally contains these elements or they are artefacts.

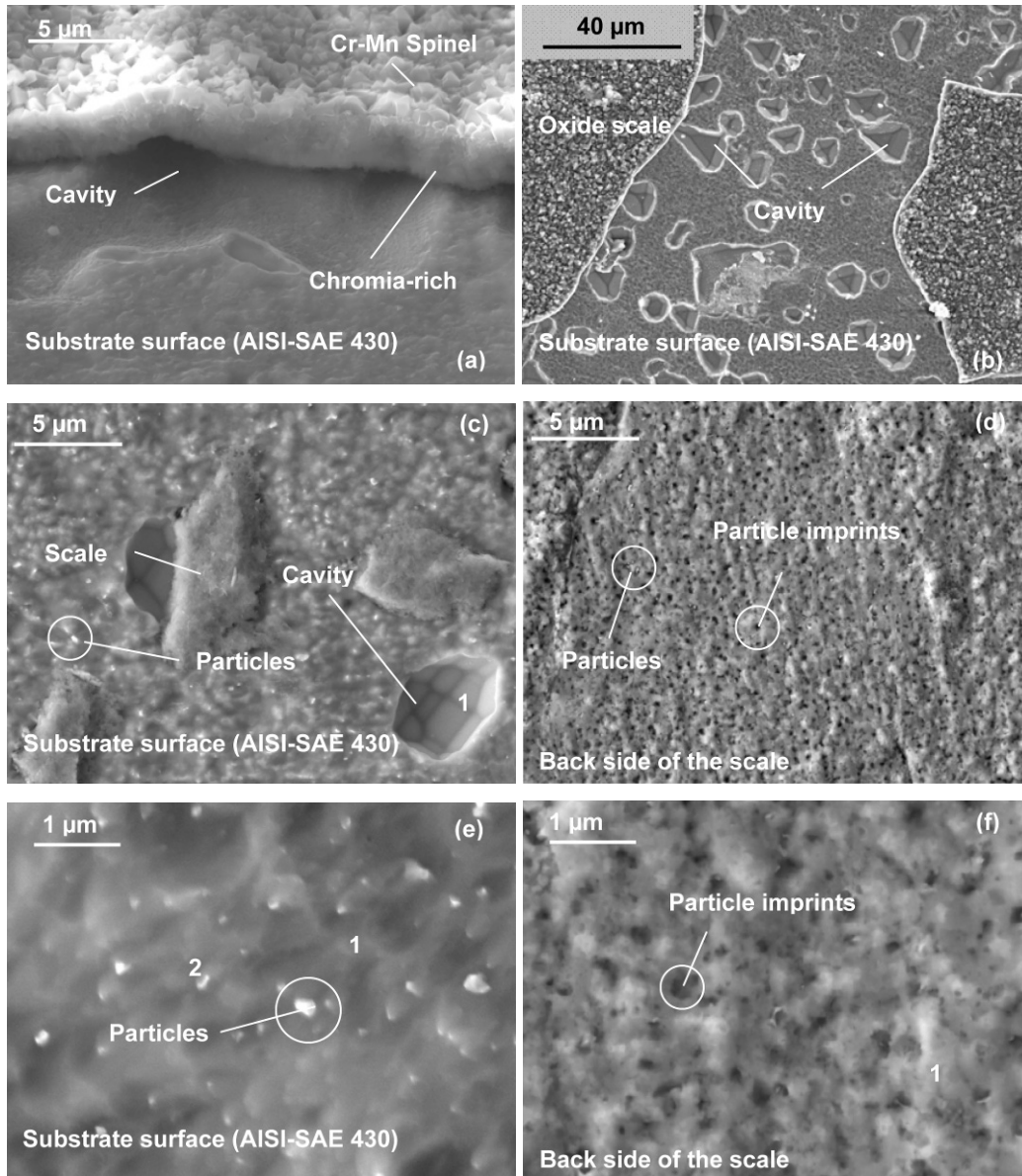


Figure 5-1 SE images of the spalled areas on AISI-SAE 430 and underside of the detached scale. (a), (b), (c) and (e) show the metallic surface; (d) and (f) represent the related underside of the scale.

The Auger spectra are presented in Figure 5-2. The spectrum in Figure 5-2(a) shows Fe, Cr, S and Cl on the metal surface at point 1 in Figure 5-1(e) where no particle is present. Figure 5-2(b) shows the spectrum obtained from the particle surfaces, i.e., point 2 in Figure 5-1(e). The same elements, as well as N, are

observed for the particles on the surface. This indicates that only particle containing surfaces contain small amounts of N, while S and Cl are present throughout the surface as well as on the particles. Elements such as S, Cl and N are tramp impurities, the presence of which is not uncommon in commercial grades of steels even with negligible concentrations of these elements (e.g., ppm levels). The spectrum obtained for the surface of cavities (point 1 in Figure 5-1(c)) shows Si, Cr and weak signals for Fe (Figure 5-2(c)). Segregation of Si to the interior surface of cavities is observed. Silicon was not detected on the metal surfaces (Figure 5-2(a)). The Auger spectrum in Figure 5-2(d), which was obtained from point 1 in Figure 5-1(f), shows that the underside of the scale mostly consists of Si. A weak signal for Cr (likely as chromia) is also present. This means that the underside of the scale surface is mainly a layer of silica.

Since both cavity surfaces and the underside of the scale contain Si, it can be concluded that Si segregates to the entire interface. Si attaches to the underside of the scale and detaches from the metal surface upon spallation of the scale. However, Si remains on the surface of the cavities where the scale is not in contact with metal.

Although the levels of impurities in the bulk substrate may be too small to be detected by AES, they can be detected at the scale/metal interface because of their segregation and concentration enhancement at the interface. Surface segregation of impurity elements, in particular S, in alumina and chromia formers at high temperatures is a well known phenomenon [13-22]. When the temperature is sufficiently high for diffusion of dissolved elements to occur, several driving forces lead to surface segregation. These driving forces include [16]:

- free surface bond saturation with segregating atoms;
- segregating atoms reducing the surface energy of the steel;
- the release of elastic energy from the alloy lattice by surface segregation of interstitials and substitutional atoms larger than the Fe atoms.

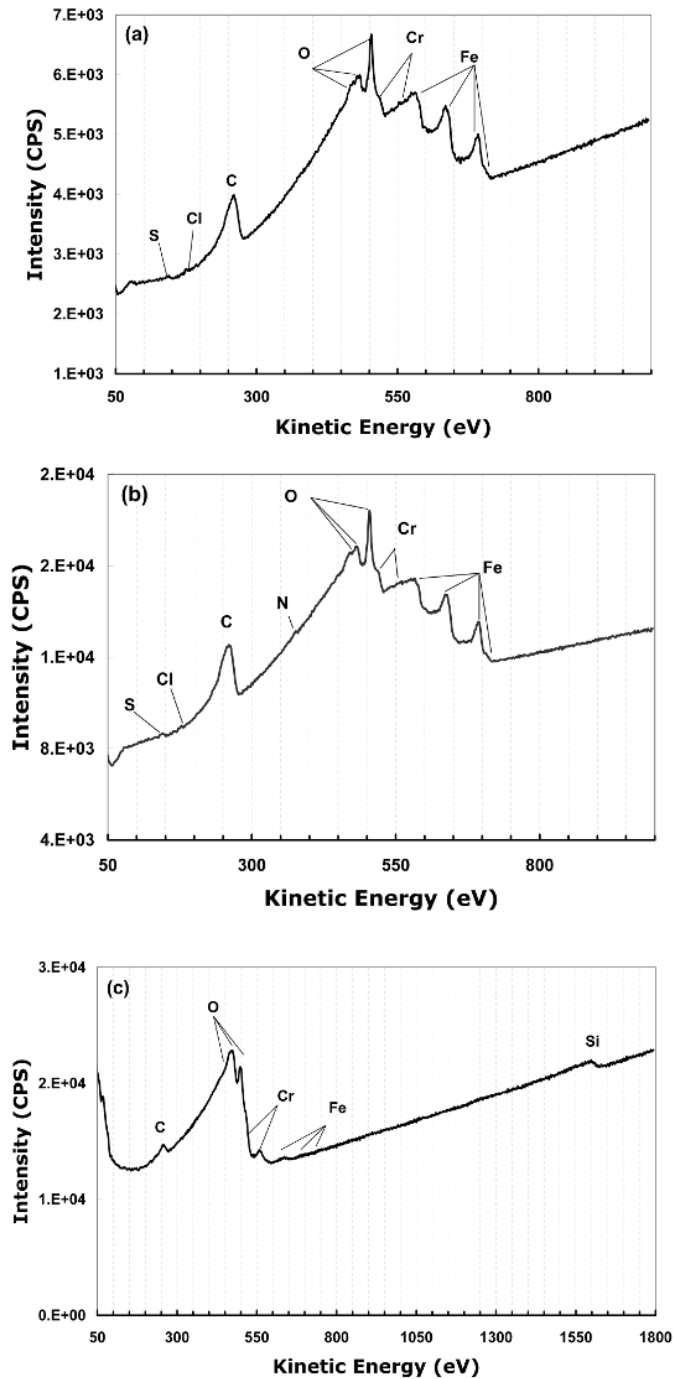


Figure 5-2 Auger electron spectra (AES) for the metal surface (a), particles (b), cavity surface (c) the corresponding underside of the scale.

Nucleation and growth of interfacial voids has been studied for alumina and chromia formers, in more detail for alumina formers, and are attributed to

interfacial segregation of S in the absence of reactive elements [13, 14, 22-24]. In chromia forming alloys, chromia scales grow predominately by outward transport of Cr cations through the scale grain boundaries [25]. Outward diffusion of Cr and its consumption in the scale results in depletion of the alloy surface region in Cr. Deficiency of Cr in the surface region creates a concentration gradient through the metal surface layer. At the same time, there will be an opposite gradient for the Fe concentration, which is richer at the interface compared to regions deeper in the bulk. Iron diffuses faster than Cr in α -Fe-19Cr alloys (e.g., $D^*_{Fe} \approx 1.33 \times 10^{-11} \text{ cm}^2/\text{s}$ (26) vs. $D^*_{Cr} \approx 5 \times 10^{-12} \text{ cm}^2/\text{s}$ (27) at 1073K). This leads to formation of opposing fluxes for Cr and Fe and the development of a net flux of vacancies toward the interface. Vacancies coalesce and form vacancy clusters in high-energy locations (e.g., misfit dislocations at the interface), which are suitable for the nucleation of voids. Voids introduce new free surfaces, which increase the interfacial surface energy. The growth of voids is then limited by the increase in interfacial energy. However, as has been discussed previously, impurity segregation effectively decreases the surface energy of voids via saturation of the free surface bonds or by decreasing the lattice elastic energy induced by dissolved atoms. [15, 16, 22]. Reducing the surface energy of voids, as the result of impurity segregation, results in void growth and the formation of cavities.

Segregation of Si, S, Cl and N to the metal-oxide scale interface on the metallic side is confirmed by AES for the AISI-SAE 430 samples. Therefore, formation of the cavities underneath the scale is attributed to an outward Cr cation diffusion mechanism for oxidation and segregation of impurities, in particular Si. Outward diffusion of Cr results in nucleation of voids, while segregation of impurities results in a reduction in the surface energy of the voids and their favoured growth and the formation of cavities.

Cavities dramatically reduce the contact surface area between the metal and oxide scale. The reduced actual contact area directly increases the ASR. Cavities account for 23% of the metal surface area after 500 h of oxidation at 800°C,

according to image analysis of Figure 5-1(b). Also, formation of N containing particles at the interface results in a porous, non-adherent interface on the oxide side. This also severely reduces the actual contact area, which can further increase the ASR. The particles also account for 18% of the underside of the scale (Figure 5-1(d)). The actual metal contact area, based on these contributions, is 63% of the nominal surface area. This corresponds to an increase in ASR by 37%.

5.3.2 XPS analysis

In order to study the interfacial chemistry and the chemical state of segregated impurities, XPS analysis was conducted for both the exposed, metal substrate surface and the underside of the oxide scale for an AISI-SAE 430 coupon oxidized for 500 h. In order to obtain enough surface area, i.e., larger than the lateral resolution of XPS, of exposed metal and the related underside of the oxide scale, the scale was detached mechanically as described earlier. Scale detachment was not possible for ZMG232 samples due to excellent scale adhesion.

The binding energies of the detected elements for the metal surface and the underside of the scale are listed in Table 5-2 and Table 5-3, respectively. For low intensity peaks (N 1s, Cl 2p, S 2p and Pb 4f) as well as the C 1s peak, high resolution XPS was also performed.

XPS analysis shows that in addition to S, Cl and N, which were also detected by AES, V and Pb are present on the metal surface under the scale (Table 5-2). The binding energies for Pb and V show that these elements are not in their metallic state. The binding energies reported for metallic Pb 4f_{5/2} are 141.70 eV and 141.90 eV [28] and those for Pb 4f_{7/2} range from 136.40 to 137.9 eV [28]. The binding energy for metallic V 2p_{3/2} varies from 512.14 to 512.90 eV [28]. The binding energies obtained for Pb and V are shifted away from the metallic state. Although a chemical formula for Pb and V cannot be suggested, Pb could be in the form of an oxide or halide (not sulphide or nitride) and V could be in the form

of an oxide, nitride, halide or sulphide based on the binding energies. These elements are considered as indigenous impurities in the steel, which have accumulated at the metal-oxide scale, interface and remain on the metal surface upon scale detachment. This indicates that, in addition to non-metallic impurities, metallic impurities can also exhibit interfacial segregation. The driving force for interfacial segregation of impurities, in general, is a reduction in surface energy that was discussed earlier.

No Pb, V, S or Cl was detected by XPS for the underside of the scale. This indicates that these elements tend to remain on the metal side of the interface and do not adhere to the scale as Si does. Therefore, segregation of these impurities can dramatically decrease scale adhesion. Low intensity peaks for N, Fe and Mn were also detected on the underside of the scale. These elements were not detected by AES. This is attributed to the higher sensitivity for XPS in comparison with AES.

Table 5-2 XPS analysis results for metal substrate surface of AISI-SAE 430 coupons (oxidized for 500 h in air at 800°C) after scale detachment

Peak	Position (binding energy (eV))
Fe 2p	707.06
Mn 2p	642.05
Cr 2p	576.38
O 1s	530.18
V 2p _{3/2}	514.67
N 1s	396.80 (high resolution)
C 1s	284.60 (high resolution)
Cl 2p	200.84 (high resolution)
S 2p	161.98 (high resolution)
Pb 4f _{5/2}	143.24 (high resolution)
Pb 4f _{7/2}	138.40 (high resolution)

Table 5-3 XPS analysis results for underside of detached scale formed on AISI- SAE 430 coupons (oxidized for 500 h in air at 800°C)

Peak	Position (binding energy (eV))
Fe 2p	711.02
Mn 2p	642.71
Cr 2p	575.390
O 1s	531.170
N 1s	398.80
C 1s	284.60
Si 2p	101.84

5.3.3 SIMS depth profiles

In order to confirm the interfacial segregation of Si, S, Cl, N, C, V, Pb and possibly others, and their distribution profiles along the cross section of oxidized specimens, SIMS depth profiling was performed on AISI-SAE 430 as well as ZMG232 oxidized samples. Note that the SIMS profiles were obtained from non-spalled, intact areas. SIMS depth profiles, generated with negatively and positively polarized ions, are shown in Figure 5-3(a) and (b), respectively, for an AISI-SAE 430 coupon oxidized at 800°C in air for 100 h. In addition to the impurity elements detected by AES and XPS, F, P and Al were detected with SIMS, due to the high sensitivity of this technique. Pronounced segregation of Si and non-metallic impurities (S, C, Cl, F and N as a C-N species) at the metal-oxide scale interface is seen (Figure 5-3(a)). However, P that is present in low levels in the steel does not appear to accumulate at the interface. Carbon cannot be considered as an artefact here, since analysis was conducted along with sputtering in an ultra high vacuum (UHV) environment. Metallic impurities, such as Al, V and Pb, also exhibit segregation at the interface. Note that Pb and V were also detected by XPS, and their presence at the interface is confirmed by SIMS.

The SIMS analysis here is qualitative, and higher intensities do not necessarily indicate higher concentrations when comparing different species. Higher intensities observed in the outermost 0.5 μm of the scale may be due to different ionization rates of the elements present in the Mn-Cr spinel portion and in the chromia-rich part of the scale or due to their different concentrations. The Mn-Cr spinel layer is around 0.5 μm thick, as the Mn profile shows a plateau in this region of the scale.

SEM, AES and XPS study of the metal-oxide scale interface was not possible for ZMG232 due to the good oxide scale-to-metal adhesion, which prevented scale detachment. Therefore, SIMS depth profiling was used for metal-oxide scale interfacial analysis for ZMG232 steels. SIMS depth profiling was also selected because of its fast sputtering rates and higher sensitivity to trace amounts of impurities compared with both AES and XPS depth profiling. SIMS depth profiles for a ZMG232 coupon oxidized at 800°C in air for 100 h are shown in Figure 5-4(a) for negatively polarized ions and in Figure 5-4(b) for positively polarized ions. Although S, Cl, F, C and P impurities are incorporated into the scale, they do not exhibit pronounced segregation to the metal-oxide scale interface as was observed for AISI-SAE 430 steels. The non-metallic impurities are spread throughout the entire scale thickness. Sulphides of reactive elements (Zr and La) are also detected within the scale.

Prevention of non-metallic impurities (i.e., S, Cl and F) from segregating to the scale-metal interface is attributed to the presence of reactive elements (Zr and La). Reactive elements exhibit a strong affinity for oxygen, and their ions migrate through the scale to reach the scale-gas interface where the activity of oxygen is optimal [29]. They can also form stable refractory sulphides [30]. Migration of reactive ions through the scale and their affinity for S to form stable sulphides results in dispersion of S throughout the entire scale, instead of segregation at the metal-oxide scale interface. Reactive elements may have a similar effect on Cl and P [30]. Very low levels of P are detected in the scale on AISI-SAE 430

specimens (Figure 5-4(a)), while for ZMG232, which contains reactive elements P is distributed throughout the scale (Figure 5-4(a)). Also, Cl is found throughout the scale for ZMG232 specimens. This effect was not observed for AISI-SAE 430 samples that do not contain any reactive elements. Also, large reactive ions segregate at the scale (i.e., chromia-rich) grain boundaries during their migration to the scale surface [29]. This segregation results in reduced diffusivity of oxide forming cations through the scale and can change the predominant oxidation mechanism from outward cation diffusion to inward oxygen anion transport [29]. This decreases the nucleation and growth rate of voids at metal-oxide scale boundary [29] and, therefore, increases metal-oxide scale contact and enhances metal-to-scale adhesion. The beneficial effects of reactive element addition have been thoroughly reviewed by Whittle and Stringer [31] and more recently by Pint [32], who evaluated Whittle and Stringer's work with new advancements in the field.

For positively polarized ions (metals), segregation of Si is seen (Figure 5-4(b)). However, segregation of Si is less prominent for ZMG232 compared with AISI-SAE 430 (Figure 5-4(b)). The lower Si concentration in the bulk alloy for ZMG232 relative to AISI-SAE 430 steel (0.4 vs. 1 wt.%) may be a reason for this behaviour. Also, it is possible that reactive elements show a similar spreading effect on Si as they do for non-metals. No Pb was detected for the ZMG232 steel. Segregation of Al (an alloying element in ZMG232) and V (an impurity) is not seen. Nickel is spread almost uniformly throughout the scale. Small amounts of Zr and La are also detected in the metal-oxide scale and metal portions of the samples. Most of the Zr and La in the scale is associated with S, forming sulphide phases. Sulphides are negatively polarized and hard to detect under positive polarization conditions.

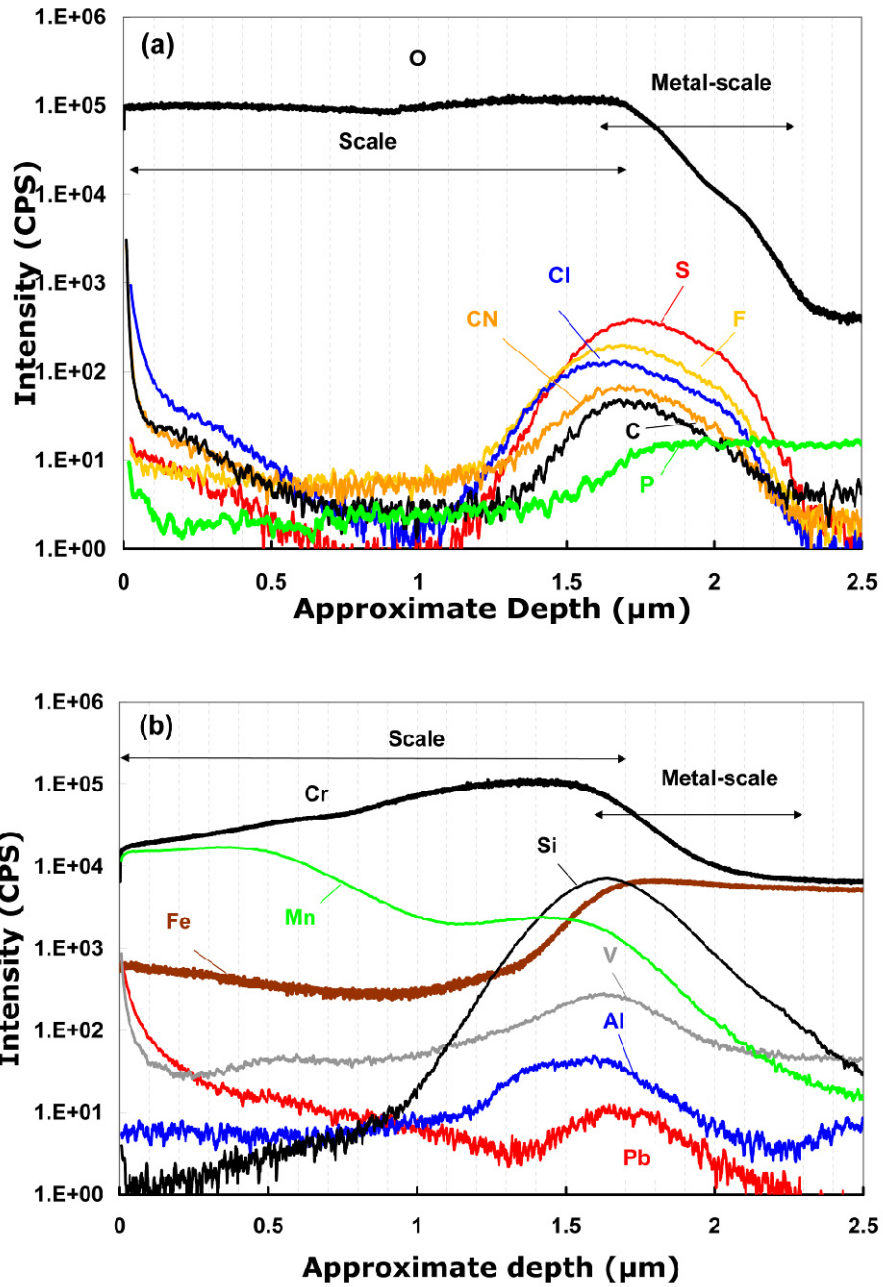


Figure 5-3 SIMS depth profiles for AISI-SAE 430 sample oxidized for 100 h at 800°C in air; (a) for negatively polarized ions and (b) for positively polarized ions.

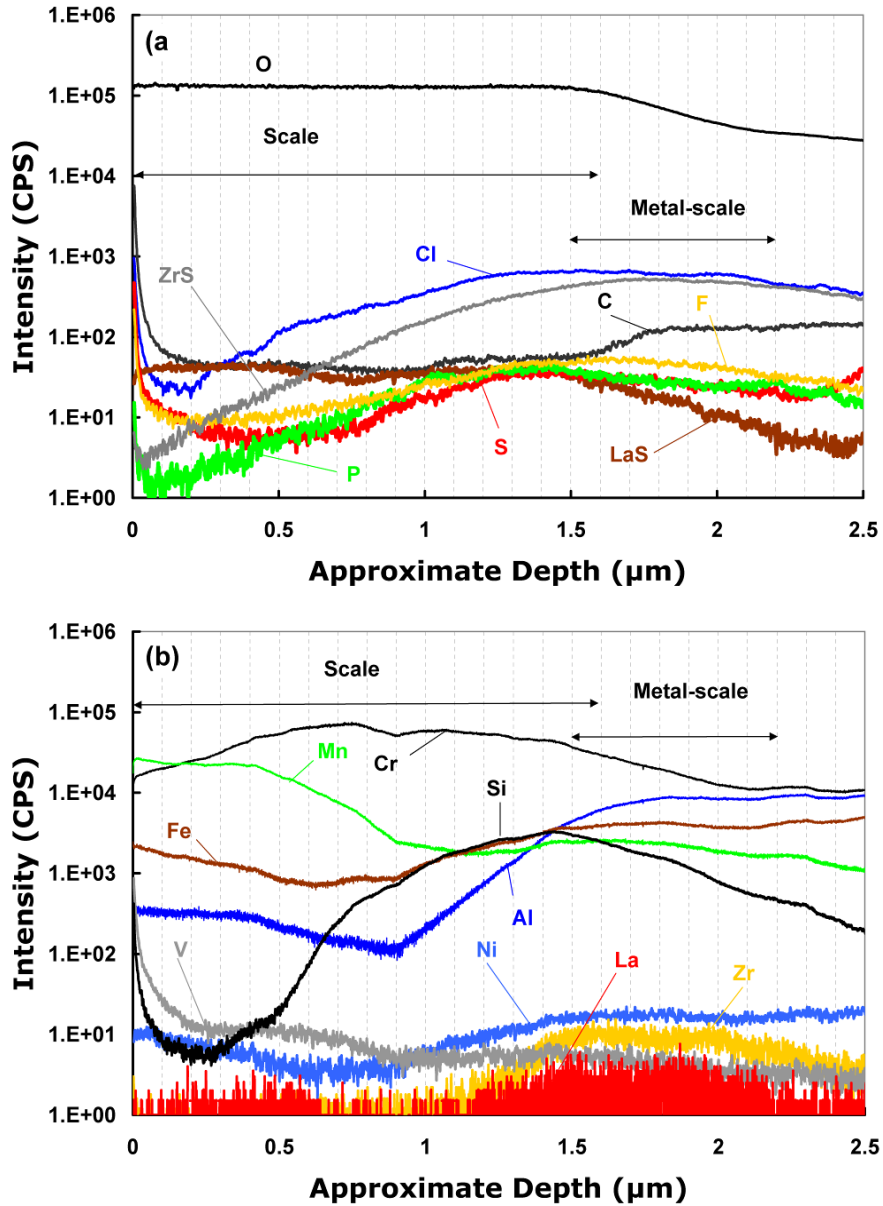


Figure 5-4 SIMS depth profiles for a ZMG232 sample oxidized for 100 h at 800°C in air; (a) for negatively polarized ions and (b) for positively polarized ions.

Improved oxide scale-to-metal adhesion and spallation resistance of the ZMG232 steel in comparison with AISI-SAE 430 steel is then attributed mainly to the presence of reactive elements in the ZMG232 steel. In the ZMG232 steel, oxygen

anion inward diffusion predominates, so there is little or no vacancy flux to the oxide/metal interface. As such void formation should be limited or non-existent.

Improved oxide scale-to-metal adhesion and spallation resistance of ZMG232 in comparison with AISI-SAE 430 is then attributed to the smaller amounts of impurities and the presence of reactive elements in ZMG232 steel.

5.3.4 Interconnect performance and interfacial defects

It is clear that interfacial imperfections, such as voids and cavities and segregated impurities can result in weakened scale-to-metal bonds, reduced scale-metal contact area and considerably higher contact resistances for the metallic interconnects. The interfacial defects stem from impurities in the steel. As a result, the composition of the steel selected for interconnect purposes evidently significantly affects scale formation and therefore interconnect performance. The portion of lost contact area due to cavities and interfacial N-containing particles is 37% for AISI-SAE 430 stainless steel after oxidation for 500h at 800°C. This does not include other segregation effects (e.g., S, Cl and Si), which further contribute to lost contact area.

It is generally known that ZMG232 steel interconnects exhibit superior conductivity over AISI-SAE 430 steels. An ASR value of 0.26 Ωcm^2 at 800°C in air after 650 h [33] has been reported for AISI-SAE 430. The reported values for ZMG232 are approximately 0.025 Ωcm^2 after 1000 h of oxidation at 750°C [34] and 0.05 Ωcm^2 after 1500 h of oxidation at 800°C [35], which are considerably lower than that for AISI-SAE 430.

5.4 Conclusions

Metal-oxide scale interfacial defects were analyzed by means of SEM, AES, XPS and SIMS for AISI-SAE 430 and by SIMS for ZMG232 stainless steels oxidized in air at 800°C. For AISI-SAE 430 oxidized steels, spallation occurs, as the

specimens are air-cooled from the furnace temperature (800°C). Spallation is attributed to poor oxide scale-to-metal adhesion resulting from segregation of non-metallic impurities such as S and Cl to the scale-metal interface. The impurities reduce the scale and remain on the metal surface upon spallation or detachment of scale. Cavities, which also contribute to poor adhesion and spallation of the scale, appear under the spalled scale on the metal surface. The formation of cavities is attributed to outward cation diffusion during oxidation, resulting in void nucleation and segregation of impurities (e.g., Si) which reduces the surface energy in favour of void growth. Also, the cavities are not in contact with the scale and, therefore, the actual metal-oxide scale contact area is reduced, which adversely affects the ASR. Segregation of impurities at the metal-oxide scale interface is also seen as submicron precipitates containing N for AISI-SAE 430. The particles, which do not adhere to the underside of the scale, lead to poor scale-to-metal adhesion and reduced contact area which further affects the ASR. For oxidized ZMG232 steels, no spallation occurs upon air-cooling from the furnace temperature. Noticeable interfacial segregation of impurities is not present for this steel; rather, the impurities are spread throughout the entire scale. This phenomenon is due to the presence of reactive elements (Zr and La) which prevent the impurities from segregating. Spallation resistance and the superior conductivity of ZMG232 steels in comparison with AISI-SAE 430 are attributed to a less defective metal-oxide scale interface.

5.5 References

1. I. Saeki, H. Konno and R. Furuichi, *Corrosion Science*, **38**, 1595 (1996).
2. I. Saeki, H. Konno and R. Furuichi, *Corrosion Science*, **38**, 19 (1996).
3. P. Singh and N. Q. Minh, *International Journal of Applied Ceramic Technology*, **1**, 5 (2004).
4. P. Huczowski, N. Christiansen, V. Shemet, L. Niewolak, J. Piron-Abellan, L. Singheiser and W. J. Quadackers, *Fuel Cells*, **6**, 93 (2006).

5. P. Huczkowski, N. Christiansen, V. Shemet, J. Piron-Abellan, L. Singheiser and W. J. Quadackers, *Journal of Fuel Cell Science and Technology*, **1**, 30 (2004).
6. L. Cooper, *MSc Thesis*, University of Alberta, Edmonton (2007).
7. L. Cooper, S. Benhaddad, A. Wood and D. G. Ivey, *Journal of Power Sources*, **184**, 220 (2008).
8. W. Z. Zhu and S. C. Deevi, *Materials Research Bulletin*, **38**, 957 (2003).
9. W. Z. Zhu and S. C. Deevi, *Materials Science and Engineering*, **A348**, 227 (2003).
10. Z. G. Yang, K. S. Weil, D. M. Paxton and J. W. Stevenson, *Journal of the Electrochemical Society*, **150**, A1188 (2003).
11. Z. G. Yang, *International Materials Reviews*, **53**, 39 (2008).
12. K. Kendall, *International Materials Reviews*, **50**, 257 (2005).
13. P. Y. Hou and K. Priimak, *Oxidation of Metals*, **63**, 113 (2005).
14. P. Y. Hou, Y. Niu and C. Van Lienden, *Oxidation of Metals*, **59**, 41 (2003).
15. H. J. Grabke, G. Kurbatov and H. J. Schmutzler, *Oxidation of Metals*, **43**, 97 (1995).
16. H. J. Grabke, V. Leroy and H. Viefhaus, *Isij International*, **35**, 95 (1995).
17. P. Y. Hou and G. D. Ackerman, *Applied Surface Science*, **178**, 156 (2001).
18. P. Y. Hou, *Journal of Materials Science Letters*, **19**, 577 (2000).
19. P. Y. Hou, *Annual Review of Materials Research*, **38**, 275 (2008).
20. P. Y. Hou and J. Mosquito, *Oxidation of Metals*, **59**, 559 (2003).
21. P. Y. Hou, X. F. Zhang and R. M. Cannon, *Scripta Materialia*, **50**, 45 (2004).
22. H. J. Grabke, D. Wiemer and H. Viefhaus, *Applied Surface Science*, **47**, 243 (1991).
23. H. J. Schmutzler, H. Viefhaus and H. J. Grabke, *Surface and Interface Analysis*, **18**, 581 (1992).
24. F. Gesmundo and P. Y. Hou, *Oxidation of Metals*, **59**, 63 (2003).
25. A. Atkinson and R. I. Taylor in *Transport in Non-Stoichiometric Compounds*, V.S. Stubican and Gim Simkovich, Plenum, New York (1985).

26. S. P. Ray and B. D. Sharma, *Acta Metallurgica*, **16**, 981 (1968).
27. A. W. Bowen and G. M. Leak, *Metallurgical Transactions*, **1**, 2767 (1970).
28. A. V. N. Charles D. Wagner, Anna Kraut-Vass, Juanita W. Allison, Cedric J. Powell, and John R. Rumble, Jr. , NIST X-ray Photoelectron Spectroscopy Database in, 2000 ed., National Institute of Standards and Technology (NIST) (2007).
29. B. A. Pint, *Oxidation of Metals*, **45**, 1 (1996).
30. J. G. Smeggil, A. W. Funkenbusch and N. S. Bornstein, *Metallurgical Transactions a-Physical Metallurgy and Materials Science*, **17**, 923 (1986).
31. D. P. Whittle and J. Stringer, *Philosophical Transactions of the Royal Society of London Series a-Mathematical Physical and Engineering Sciences*, **295**, 309 (1980).
32. B. A. Pint, in *John Stringer Symposium on High Temperature Corrosion*, I. G. W. P. F. Tortorelli, and P. Y. Hou Editor, p. 9, Materials Park, OH (2003).
33. X. H. Deng, P. Wei, M. R. Bateni and A. Petric, *Journal of Power Sources*, **160**, 1225 (2006).
34. A. Toji and T. Uehara, Stability of Oxidation Resistance of Ferritic Fe-Cr Alloy for SOFC Interconnects, in *10th International Symposium on Solid Oxide Fuel Cells (SOFC-X)*, K. Eguchi, J. Mizusaki, S. Singhal and H. Yokokawa Editors, p. 2117, The Electrochemical Society, Nara, Japan (2007).
35. C. L. Chu, J. Y. Wang and S. Y. Lee, *International Journal of Hydrogen Energy*, **33**, 2536 (2008).

6 General discussion, conclusions and recommendations

The original objective of this research work was to find an effective, conductive/protective coating for stainless steel interconnects used in SOFCs. As described earlier in Chapter 1, the ASR criterion for SOFC interconnects requires ASR values to be smaller than $0.1 \Omega \cdot \text{cm}^2$ for a period of 40,000 hours of operation. Also, the coating must be adequately effective to prevent Cr diffusion and alleviate Cr poisoning of the cathode. These objectives are discussed in detail in Chapter 1 of this thesis.

According to the literature survey of this study, the most efficient type of conductive/protective coatings is spinel. Among various techniques for application of spinel coatings, the electrodeposition of metals or alloys followed by oxidation/heat treatment in air (described in Chapter 1) is the preferred method. The application of composite metal-matrix coatings, which contain reactive element oxide particles, can further improve the protection and conduction properties of the spinels obtained by conventional metal electrodeposition. As discussed in Chapters 3 and 4, coatings with pure metals result are prone to breakaway oxidation behaviour (in the case of Ni) and spallation (in the case of Co) after relatively short periods of oxidation. The main reason for breakaway oxidation behaviour is dilution of the substrate surface in Cr as a result of the inevitable inward diffusion of a portion of the coated metal into the substrate when exposed to high temperatures for oxidation. This is a major problem associated with the use of electrodeposition for spinel coatings, which can be solved by the addition of reactive element oxide particles in the coating. As discussed in Chapter 3, the critical Cr concentration threshold for the formation of a dense, protective chromia is smaller in the presence of reactive ions.

To achieve the objective, novel coating systems for a commercially used ferritic stainless steel interconnect material, AISI-SAE 430, were developed and studied. Composite electrodeposition of reactive element containing particles in a metal matrix, which form conductive oxides when exposed to oxygen at high

temperatures, was the approach taken. Electrodeposition is a conventional technique, which can be easily employed on an industrial scale. The process is inexpensive and controllable without any need for sophisticated equipment. In addition, the composite electrodeposition process for these metals has been well studied, and high quality deposits on stainless steel substrates are attainable with electrodeposition.

The particles selected for the purpose of composite coating were LaCrO_3 . Lanthanum chromites can supply reactive element ions (i.e., La cations) to the oxide scale, and are conductive at high temperatures and stable in the aqueous electrolytes used for electrodeposition of metals. Reactive elements, particularly La, effectively enhance the oxidation resistance of high-temperature alloys. Nickel and Co were used as the metal matrices since they can form conductive oxides, including complex spinel solutions upon high-temperature oxidation.

As discussed in detail in Chapter 2, adherent, uniform composite coatings of Ni/ LaCrO_3 can be deposited on AISI-SAE 430 steels with a particle content of greater than 30 vol.%. This is attainable utilizing a simple, conventional Watts Ni plating process provided that the deposition parameters are adjusted. The results achieved in this study show that the amount of LaCrO_3 particles of $\sim 1\mu\text{m}$ average size embedded in the metal matrix depends on deposition parameters including current density, particle loading in the bath, agitation and pH. Increasing the current density and particle loading in the bath increases the amount of embedded particles to a certain point; beyond that point no increase in embedded particles can be achieved. Lowering the pH of the electrolyte results in a smaller amount of embedded particles. However, pH cannot be increased more than a specific value since increased pH decreases the cathodic current efficiency and leads to precipitation of metal ions as hydroxides in the electrolyte. In addition, the agitation method and flow pattern in the electrolyte is a factor affecting the amount of embedded particles. Agitation from the top with the use of an overhead impeller increases the amount of embedded particles by approximately 5 vol.%.

For Ni/LaCrO₃ coatings, by adjusting the above parameters, approximately 35 vol.% particles can be included in the metal matrix. The higher the amount of particles the greater the source of beneficial reactive elements.

Long-term oxidation of Ni/LaCrO₃-coated AISI-SAE 430 coupons results in the growth of a double layer oxide scale. The innermost layer is chromia-rich and contains LaCrO₃ particles. The outermost layer is a Ni-Fe-Mn-Cr spinel solid solution together with NiO particles. This oxide scale exhibits good adherence to the substrate and exhibits excellent, electronic conductivity. Ni/LaCrO₃ composite coatings greatly decrease the ASR of the substrates. The ASR value obtained with this type of coating was 0.005 Ωcm² after 400 hours of oxidation. The ASR was fairly stable during the test period and reached a plateau after short term of oxidation. The ASR value achieved with Ni/LaCrO₃ coatings is anticipated to be well below the criterion, although long test times are required to evaluate the very long-term performance. The ability of the coating to decrease ASR is attributed to the inclusion of conductive LaCrO₃ particles in the chromia-rich subscale, formation of conductive oxides including doped (with substrate elements) NiO, mixed Fe/Ni-based spinels and, more importantly, improved oxide scale-to-metal adhesion. The coating was also highly effective in reducing Cr outward diffusion from the chromia-rich subscale. Only 3 wt.% Cr was detected in the outer portion of the oxide scale.

In comparison with Ni/LaCrO₃, which can consist of 35 vol.% particles, the amount of embedded particles in Co/LaCrO₃ coatings does not exceed 20 vol.% under the optimal conditions. The oxide scale, which forms on the Co/LaCrO₃ coated samples, consists of three layers. The innermost layer is chromia-rich with some particles. The middle layer is a Co-Fe spinel solid solution, which also contains LaCrO₃ particles and the outermost layer is Co₃O₄. Porosity is observed in the outer Co₃O₄ layer and in the middle layer spinel. Coatings of Co/LaCrO₃ also effectively reduced the ASR values in comparison with uncoated substrates. The ASR achieved with Co/LaCrO₃ coatings was 0.02 Ωcm². The Cr retention

with this coating system was excellent. Only 1 wt.% Cr was detected in the outer portion of the scale. The improvements achieved with the application of this coating are attributed to the presence of reactive element containing particles that enhance the oxide scale-to-metal adhesion. The marked reduction in Cr outward diffusion is attributed to formation of Co-containing spinel solutions.

In both composite coatings, it was observed that LaCrO_3 particles play a critical role in reduction of oxidation growth rate and scale adhesion. This effect is attributed to the ability of the reactive element (La) to react with indigenous impurities, spread them throughout the oxide scale and, thus, prevent their interfacial segregation.

Superior results are achieved with the Ni matrix over the Co matrix. Although, as described in Chapter 1, Co containing spinels are better electronic conductors at high temperatures, the ASR values obtainable with Ni/ LaCrO_3 coatings are four times smaller than those for the uncoated substrate under similar testing conditions. This is attributed to a less porous, thinner oxide scale and less defective metal-oxide scale interface when Ni is used as the matrix for composite coatings. According to the results achieved in this study, Ni containing spinels (containing substrate elements such as Fe, Cr and Mn) are markedly denser than their Co containing counterparts. This improves the oxidation protection properties of the thermally grown spinel layer as well as the contact area between the spinel and inner chromia-rich layer.

Additionally, during experimentation, it was found that for currently used steel interconnects the metal-oxide scale interfacial imperfections play a critical role in electrical degradation of steel interconnects. Since the electric current must pass through the interface, poor adhesion and the presence of defects of various types can dramatically reduce the area through which the electric current passes and, thus, increase the contact resistance. Impurity element segregation, particularly Si, at the metal-oxide scale interface is the most critical issue addressed in Chapter 5.

The interfacial imperfections include cavities, small inclusions of N-containing particles and considerable accumulation of metallic and non-metallic impurities. The reason behind interfacial void formation and impurity segregation is the predominant outward Cr diffusion mechanism of oxidation. Outward migration of Cr from the substrate and through the chromia layer results in the formation of interfacial voids. Voids increase the interfacial free energy, but impurities decrease this energy by segregation and saturation of the free surface bonds. Reactive ions can prevent segregation of impurities and change the predominant mechanism of oxidation from outward cation diffusion to inward oxygen anion diffusion through the chromia layer. Therefore, as discussed in detail in Chapter 6, the presence of reactive elements in the steel, as well as in the coatings, is required to maintain good adhesion and contact between the oxide scale and the substrate. Therefore, it is suggested that the oxide thickness and its conductivity are not the only critical factors that must be accounted for and ASR is not simply the product of the oxide thickness and its conductivity, as was believed before. In calculating ASR, both the apparent surface area of the scale and the actual surface area of contact between the metal and the oxide scale must be accounted for (Eq. 6-1). These are not necessarily equal to one another unless perfect contact exists between the scale and the metal.

$$ASR = \rho \frac{l}{A_{contact}} A_{scale} \neq \rho \cdot l \quad \text{Eq. 6-1}$$

where R is resistance (Ω), $A_{contact}$ (cm^2) is the surface area where the metal and oxide scale are in actual contact, A_{scale} (cm^2) is the apparent surface area of the oxide scale, ρ (Ωcm) is the resistivity of the oxide scale and l (cm) is the thickness of the oxide scale.

In summary, the prominent advantage of the coatings developed and studied in this research work is to improve and solve the problems associated with the preferred method of spinel coating, i.e., electrodeposition. Also, the resistance

contributions from interfacial defects resulting from inappropriate steel composition had not been previously accounted for in studies concerning SOFC interconnects. Based on the results achieved in this study, future research on metallic interconnects will move towards a new direction.

6.1 Recommendations for future work

Since the main conclusion of this study indicates that the presence of reactive elements is a vital factor determining the performance of steel interconnects at high temperatures, further studies should concentrate on the role of reactive element additions. Electrodeposition of composite coatings was shown to be an effective way for both decreasing the contact resistance and providing Cr migration inhibition. This technique is also industrially feasible and inexpensive without any need for complicated and costly deposition instruments. Therefore, it is recommended that future studies focus on finding the optimal composite system. For example, Y is more effective than La in terms of oxidation behaviour improvement in most cases. Lanthanum can be replaced with Y to form more stable compounds (e.g., YCrO_3). The size of the reactive element containing particles can also be a determining factor. Theoretically, smaller particles can be more effective in supplying reactive element ions than larger ones due to the higher surface to volume ratio. The metal matrix can also be varied to achieve more promising results. Alloys that form conductive spinels can replace Ni or Co. Moreover, application of such coating on substrates with higher purity is recommended. Particularly, alloys with lower levels of Si can lead to improved scale adhesion and lower contact resistance.

In particular, the following items can be the subject of further studies:

- Application of Ni/LaCrO_3 and Co/LaCrO_3 on more advanced substrates (e.g., ZMG232, ZMG232L, Crofer 22 APU and E-brite).

- Development, study and optimization of composite electrodeposition/electroless deposition of metals and stable nano particles containing reactive elements (e.g., Ni/LaCrO₃ or Ni/YCrO₃).
- Application of the above mentioned nano-composite coatings on specialty interconnect alloys (e.g., ZMG232, ZMG232L, Crofer 22 APU and E-brite) and long term study of oxidation behaviour and electrical properties.
- Characterization of the oxide scales on the above mentioned coatings in more detail (e.g., use of transmission electron microscopy) to determine the role of reactive elements in the oxidation process.
- Characterization and analysis of metal-oxide scale interface for various interconnect steels, both coated or uncoated.

Moreover, inasmuch as there is no standard method for measuring the ASR of interconnects, research work can be dedicated to study and develop a standard, reliable method. This is important since the effectiveness of coatings is primarily determined through ASR tests.

7 Appendix- Preliminary proposal and experiments

7.1 Introduction

This section of the thesis is dedicated to some unpublished/unsuccessful work which was done in the early stages of this research project. Although this part of the work was unsuccessful, it was the basis for the successful and published material from the entire research project. This section concerns the early investigations and proposed solutions for the issues related to ferritic stainless coatings which are described in detail in Chapter 1 of this thesis.

As thoroughly described in Chapter 1, the main objective of this research study was to develop a coating system which is able to reduce the contact resistance and enhance the oxidation resistance of conventional ferritic stainless steels. To accomplish this aim, some ideas were proposed and some preliminary tests were conducted to evaluate the feasibility of the proposed methods. The initial proposed idea was to apply composite coatings containing particles that are reasonably conductive at the operating temperatures of SOFCs and chemically and physically stable under corrosive environments of SOFCs. Inclusion of such particles was expected to provide conductive paths through the poorly conducting oxide scale and connect the conductive, metallic substrate to the surface of the oxide scale. Also, the matrix of these composite coatings was designed to provide exceptional oxidation resistance at the upper operating temperature limit of SOFCs (800°C) for long periods of operation.

Since most research studies concerning high-temperature oxidation resistant coatings are related to turbine blades used in jet engines and power plants, reviewing related studies was the initial step to search for a suitable protective coating for stainless steel interconnects. Although there are several substantial differences between metallic SOFC interconnects and turbines in terms of function, operating conditions and materials, reviewing the research conducted in this area was done in the hope that it would lead to a reliable solution for SOFC

interconnects. The differences between turbines and SOFC interconnects include the substrate alloy to be coated, the operating temperature range and the requirement for reasonable electronic conductivity for the former case. The substrate alloys used for turbines are austenitic Ni-based (or Co-based) superalloys while the preferred interconnect alloys for SOFCs are ferritic stainless steel. The operating temperature range for turbine blades is 900-1200°C, while interconnects are supposed to operate at 750-850°C. Regardless of the differences, in both cases, protective coatings are required to provide oxidation and corrosion resistance at high temperatures and in harsh environments.

There are two basic protective coating systems which currently are used for gas turbines. These coatings are categorized as diffusion and overlay coatings [1].

Diffusion coatings change the substrate surface composition through a diffusion process. Diffusion coatings enrich the surface with Al, Cr or Si in order to form protective Al_2O_3 , Cr_2O_3 or SiO_2 oxide scales upon high temperature oxidation [1]. Chemical vapour deposition (CVD) (i.e., pack cementation) is the common technique for application of diffusion coatings [1] in particular aluminide coatings. Diffusion coatings of Al to provide Ni or Co aluminides on superalloys have been widely used in the past. Recently such coatings have been modified in several ways in order to enhance the protective properties of the coatings for application at higher temperatures and in corrosive environments. Diffusion Al coatings can be modified via the following techniques:

- Co-deposition of elements from a pack or slurry (e.g., reactive elements).
- Pretreatment of the substrate before pack aluminizing, e.g., chromizing prior to aluminizing.
- Deposition of a precious metal layer using electroplating or physical vapour deposition (PVD) techniques. For example, a platinum-aluminide coating is formed by depositing platinum onto the substrate before aluminizing.

Platinum is known to substantially improve the protective properties of aluminide coatings [1]. The presence of platinum in nickel aluminide promotes the formation of a slowly growing, high purity protective alumina scale [2]. Platinum enhances the diffusivity of Al in the alloy and, thus, results in an Al-rich phase at the alloy surface underneath the oxide scale. The enhanced diffusivity of Al is believed to promote the formation of a pure, uniform initial protective oxide scale and to limit the formation of interfacial voids and cavities. The beneficial effect of Pt addition can be reduced in the presence of S, as an indigenous impurity or a constituent of the environment [1].

Pack aluminization is a CVD process which has been widely used for the purpose of aluminization of Ni and Co-based high-temperature alloys. In this process, the substrates to be coated are immersed in a mixture of powders and retained in a sealed or semi-sealed container, which is referred to as a pack. The pack is then heated to 650-1200°C and kept at that temperature for a certain period of time (normally several hours) to reach the required diffusion depths [3]. The pack contains a powder mixture consisting of an aluminum donor (i.e., Al or an Al alloy), an activator (i.e., Al, ammonium or alkali halide) and a diluting media (i.e., alumina powder). Upon heating, the Al or Al alloy powder melts and reacts with the halides to form gaseous species of Al halides. These volatile compounds migrate to and dissociate on the surface of the substrate alloy and produce atomic Al which can diffuse inside the substrate surface to form aluminides. Provided that the activity of Al is high enough, the halides of other elements from the substrate are not stable and do not diffuse out of the substrate [4]. As described previously, an Al diffusion coating can be used on Pt-plated substrates for a more protective alumina scale.

The process is easy to conduct and sophisticated instruments are not necessary. However, diffusion parameters including pack composition, temperature and time

must be carefully adjusted to obtain the desired results. Also, Kirkendall diffusion voids can form along the aluminized zone and the intact substrate interface.

Alternative high-temperature protective coatings are overlay coatings. Basically a layer of a coating material is applied on the surface of the substrate and there is no reaction or diffusion process to form such coatings. Thermal spray techniques and, to a lesser extent electrochemical deposition, are the methods for application of overlay coatings on superalloys. The material used for the purpose of coating is generally known as MCrAlY, where M is a metal and can be selected from Fe, Ni, Co, Ti, Mn, etc. or a combination of them depending on the purpose of application. MCrAlY coatings normally contain 15-45 wt.% Cr, 7-20 wt.% Al and 0.1-5 wt.% Y, although other reactive elements, including La and Ce, can be used [5-7]. According to the ternary phase diagram for Cr-Ni-Al, shown in Figure 7-1, the microstructure of a typical MCrAlY alloy with a nominal composition of 20 wt.% Cr, 10 wt.% Al and 70 wt.% Ni, is β -NiAl phase in a γ -Ni matrix. This composition is ideal for oxidation resistance. At 1150°C, Cr exists as a solid solution in the nickel matrix and with a very small concentration in β -NiAl. At higher Cr concentrations, α -Cr may be present in the microstructure of the alloy.

The MCrAlY overlay coatings provide a high activity for Al as well as a significant concentration of Cr [9]. The β -NiAl phase provides a source of Al to promote the formation of alumina protective scales. Platinum can be added for enhanced activity of Al in the coating [9]. Chromium is required to provide high-temperature corrosion resistance in atmospheres containing oxygen and other corrosives [10]. Yttrium or other reactive elements enhance the scale-to-metal adhesion and oxidation resistance. A carefully designed MCrAlY coating material with appropriate composition can provide exceptional high-temperature oxidation and corrosion resistance in a variety of corrosive environments.

Since thermal spraying is used for overlay coating, the coating is porous and thick. Also, in thermal spray coating, the coverage depends on line-of-sight and

coatings on complex shapes are impossible. Therefore, diffusion coatings were preferred for the purpose of experiments in this research work. In addition, application of diffusion coatings is quite feasible using conventional laboratory equipment.

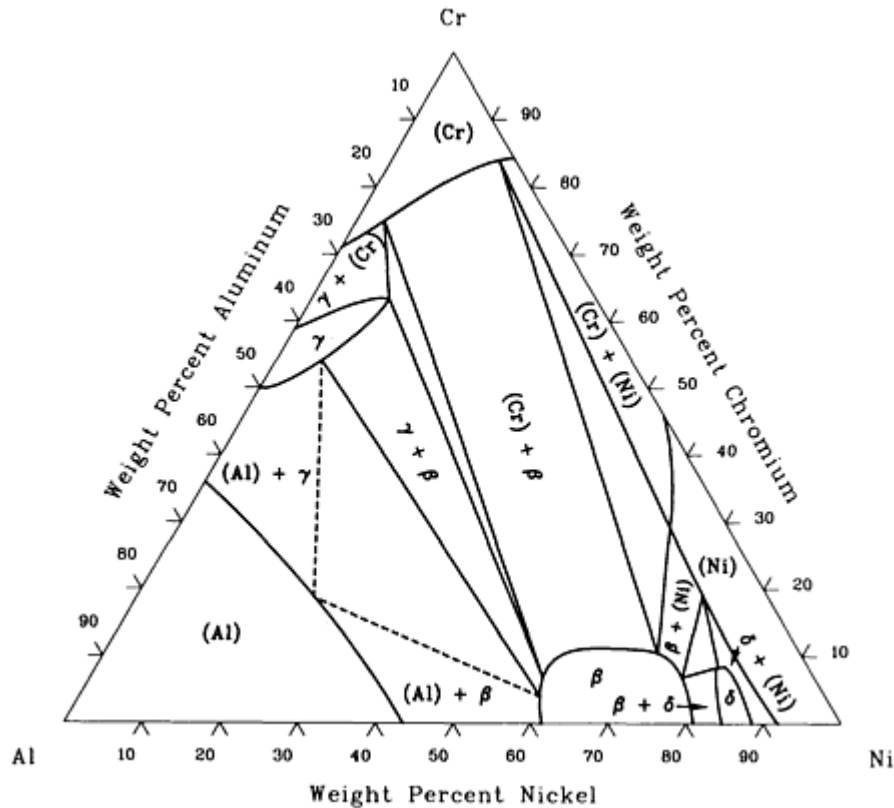


Figure 7-1 Al-Cr-Ni isothermal ternary phase diagram at 1150°C [8].

Although application of aluminide coatings, regardless of the application technique (diffusion or overlay), is limited due to insulating nature of alumina scales, it is possible to improve the conductivity of the scale by embedding stable, conductive ceramic particles. Conductive particles may provide conduction paths through the oxide scale and connect the scale surface to the conductive metallic substrate. In order to select a proper conductive compound, the following criteria must be met:

- Electronic conductivity at operating temperature (i.e., 800°C);
- Chemical and physical stability;
- Compatibility with Al at elevated temperatures;
- Negligible ionic conductivity especially for oxygen to avoid oxygen transport.

Binary ceramic compounds including borides, nitrides, carbides, silicides and oxides were investigated in terms of electronic conductivity and oxidation resistance. Although borides and nitrides have reasonable electronic conductivity, their oxidation resistance at 800°C or higher temperatures is poor. Carbides can barely satisfy both the electronic conductivity and oxidation resistance requirements simultaneously. Silicides are the most appropriate group of binary compounds in terms of electronic conductivity and oxidation resistance. However, their high oxidation resistance stems from the formation of a protective silica layer which is insulating. Most of the stable binary oxides do not exhibit adequate electronic conductivity. All the binary ceramic compounds are, therefore, excluded from serious consideration.

However, ternary oxides including perovskites and spinels can be good electronic conductors at elevated temperature depending on the composition. Perovskites are preferred over spinels due to their higher electronic conductivity and compositional stability. Also, most perovskites contain reactive elements which are beneficial for oxidation resistance.

Lanthanum chromites, which have a perovskite structure, have been investigated widely in terms of their physical and chemical properties as well as electronic and ionic conductivity under fuel cell operating conditions. Perovskites have been successfully applied in service as SOFC interconnects and are stable and conductive in SOFC operating environment.

Rare earth perovskites are good electronic conductors. The conductivity can be greatly improved once properly doped with alkali earth metals. The electrical conductivities of several doped lanthanum chromites at 1000°C in various atmospheres (air, argon and hydrogen) are summarized in Table 7-1 . Doping with Ca leads to a higher electronic conductivity in air and argon, while Sr doping results in a higher conductivity in a hydrogen environment. Also, from this table, it is clear that the conductivity increases with increasing dopant concentration [11].

Table 7-1 Electrical conductivities of some alkali earth doped lanthanum chromites at 1000°C [11]

Sample	Electrical conductivity (S cm ⁻¹)		
	In air	In Ar	In H ₂
LaCr _{0.9} Mg _{0.1} O ₃	5.6	5.6	0.27
LaCr _{0.8} Mg _{0.2} O ₃	5.9	5.6	0.39
La _{0.9} Ca _{0.1} CrO ₃	12.1	12.1	2.7
La _{0.8} Ca _{0.2} CrO ₃	40.0	38.4	4.8
La _{0.7} Ca _{0.3} CrO ₃	45.7	45.5	4.4
La _{0.9} Sr _{0.1} CrO ₃	8.5	8.3	2.1
La _{0.8} Sr _{0.2} CrO ₃	36.6	26.6	6.4
La _{0.7} Sr _{0.3} CrO ₃	41.5	40.4	4.9

Another issue in the selection of conductive particles is their compatibility with other cell components, the coating matrix and the ferritic stainless steel substrate. Reaction between the interconnect material and the other cell components can either increase cell resistance when the reaction product is an insulator, or lead to thermal stresses and subsequent failure. Lanthanum chromites are acceptably compatible with YSZ particularly in terms of CTE [12]. Lanthanum chromites doped with Sr are generally more chemically compatible with YSZ in comparison with those doped with Ca [11]. Reaction layers have been observed between Ca-doped lanthanum chromites and the YSZ electrolyte [13-15]. Although, strontium

doped lanthanum chromite appears to be more compatible than Ca-doped lanthanum chromite, SrCrO_4 has been observed to form at the interface between Sr-doped lanthanum chromites and a ceria-doped electrolyte [16].

As described previously, with a composite coating of lanthanum chromites, as conductive particles, and a high temperature oxidation resistant alloy, both goals of oxidation resistance and electronic conductivity can be attained. For this purpose, composite electrodeposition of lanthanum chromite particles in a Ni matrix followed by pack cementation aluminization was proposed. This idea is schematically shown in Figure 7-2. As seen in this diagram, conductive LaCrO_3 particles can pass through the alumina scale which is not conductive and provide conduction paths.

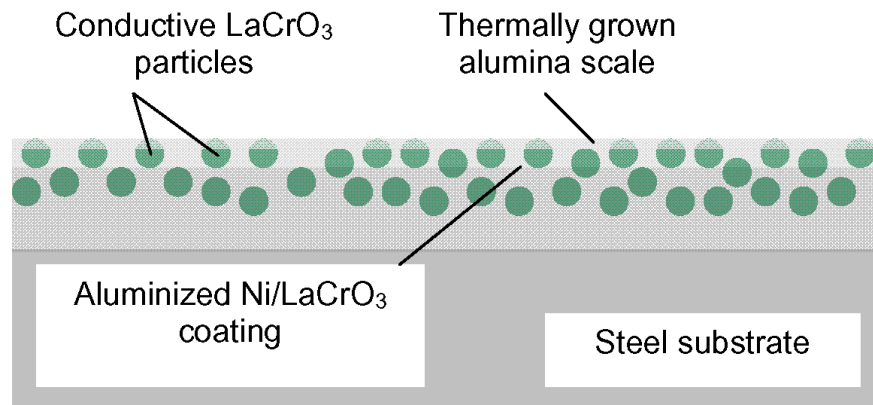


Figure 7-2 Schematic representation of an aluminized Ni/LaCrO₃ coating.

7.2 Experimental methods

The substrate alloy used for all experiments was AISI-SAE 430 stainless steel cut in small coupons measuring 1 mm × 10 mm × 20 mm. The sample preparation techniques, the instruments used for analysis and electrodeposition details are discussed in Chapter 2 of this thesis.

The first part of the preliminary experiments was dedicated to Ni/LaCrO₃ composite electroplating. For the purpose of co-deposition of LaCrO₃ particles in the Ni matrix, a Watts Ni bath containing suspended particles was employed. The details for composite electroplating can be found in Chapter 2 of this thesis. Two different anode and cathode positions, including vertical and horizontal, in the plating bath were examined.

As discussed previously, diffusion Al coating via pack cementation technique were preferred over thermal spray overlay coatings. The composition of the pack used was 4 wt.% Al powder with an average particle size of approximately 3 μm, 2 wt.% ammonium chloride and alumina powder as the filler. Quartz self-sealing crucibles were used to retain the pack powder. A tube furnace equipped with a sealed quartz tube was employed for the process. The process was conducted under an argon atmosphere at 1000°C for 5 hours. Annealing of the Ni/LaCrO₃ coated samples was also performed in the same electrical tube furnace, but using 5%H₂-N₂ forming gas instead of argon.

7.3 Results and discussion

The anode and cathode were first placed vertically in the plating beaker. No significant amount of embedded particles was observed in the coatings applied to vertically placed cathodes. A cross sectional SEM image of one such coating is shown in Figure 7-3. EDX spectra, however, confirmed the presence of some embedded particles.

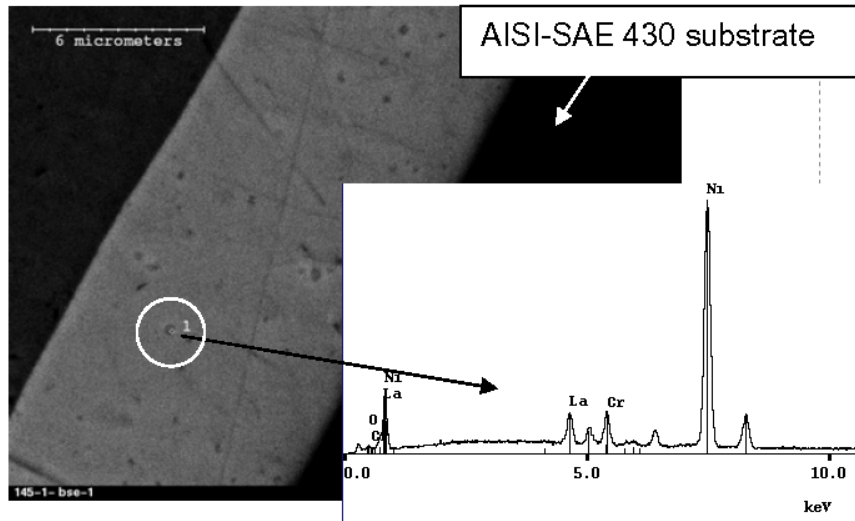


Figure 7-3 SEM cross sectional BSE image of a Ni/LaCrO₃ coating plated in a vertical bath set-up.

In contrast, with a horizontal cathode, the amount of embedded particles in the coating increased while other parameters remained unchanged. A cross sectional SEM image of a composite coating obtained using a horizontal cathode set-up is shown in Figure 7-4.

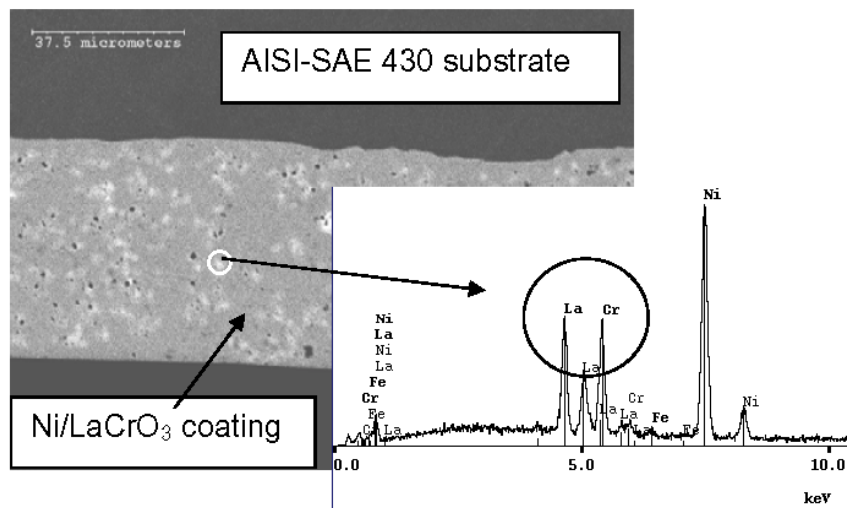


Figure 7-4 SEM cross sectional BSE image of a Ni/LaCrO₃ coating plated in a horizontal bath set-up.

The Ni/LaCrO₃ coated samples with a coating thickness of approximately 20 μm were placed in aluminization packs and aluminized for 5 hours at 1000°C under flowing argon.

A cross sectional SEM image of an aluminized Ni/LaCrO₃ coating, along with related EDX spectra, for different regions is shown in Figure 7-5.

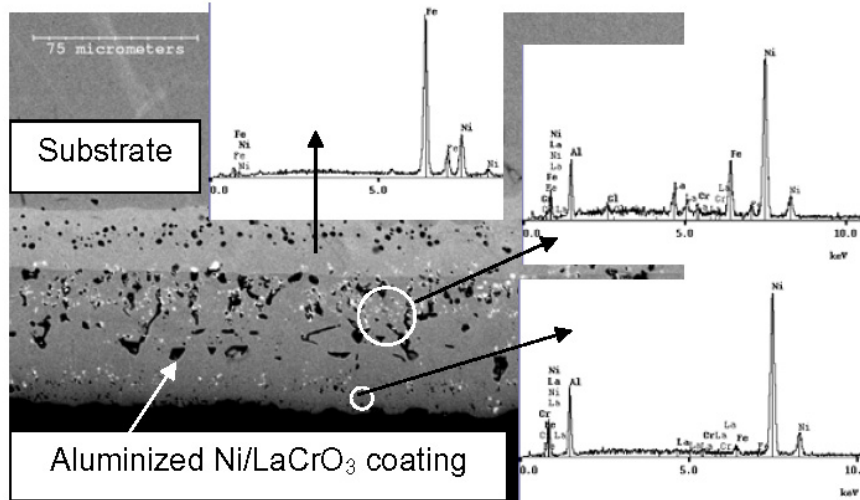


Figure 7-5 SEM cross sectional BSE image of a Ni/LaCrO₃ coating aluminized via pack-cementation at 1000°C for 5 hours.

In addition to the formation of diffusion voids at the substrate/aluminide interface, the aluminized zone is visibly porous. Also, it was found that Cl reacts with the LaCrO₃ particles. The incorporation of Cl and the compositional changes to the particles are more clearly seen in Figure 7-6.

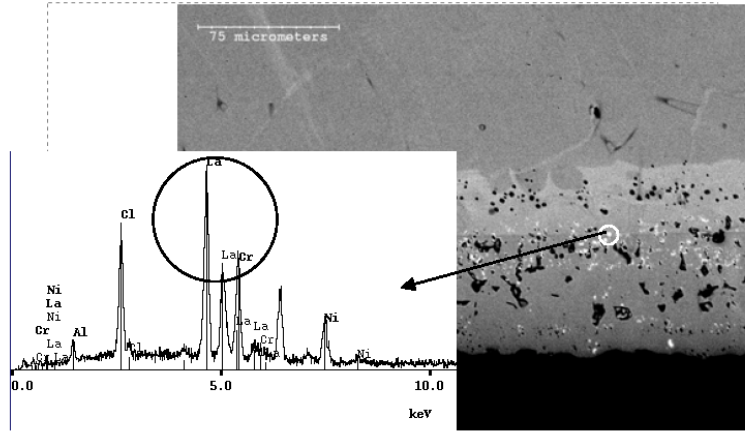


Figure 7-6 SEM cross sectional BSE image of a Ni/LaCrO₃ coating aluminized via pack-cementation at 1000°C for 5 hours (absorption of Cl into the LaCrO₃ particles).

It was concluded that LaCrO₃ particles can react with Cl and are not chemically stable in halide containing environments. Therefore, further experiments to modify the aluminization process were avoided and this process was abandoned.

It was believed that the Ni/LaCrO₃ coating would not show oxidation resistance since NiO is not regarded as a protective oxide. Therefore, it was decided to perform a heat-treatment in a controlled atmosphere in order for Cr to diffuse from the substrate to the surface to increase the oxidation resistance by the formation of protective chromia. In this way, 5%H₂-N₂ forming gas was used as the atmosphere and several combinations of temperature and time were used for heat-treatment. Temperatures of 800, 1000 and 1100°C for time periods of 15 min to 24 hours were selected for heat-treatment experiments.

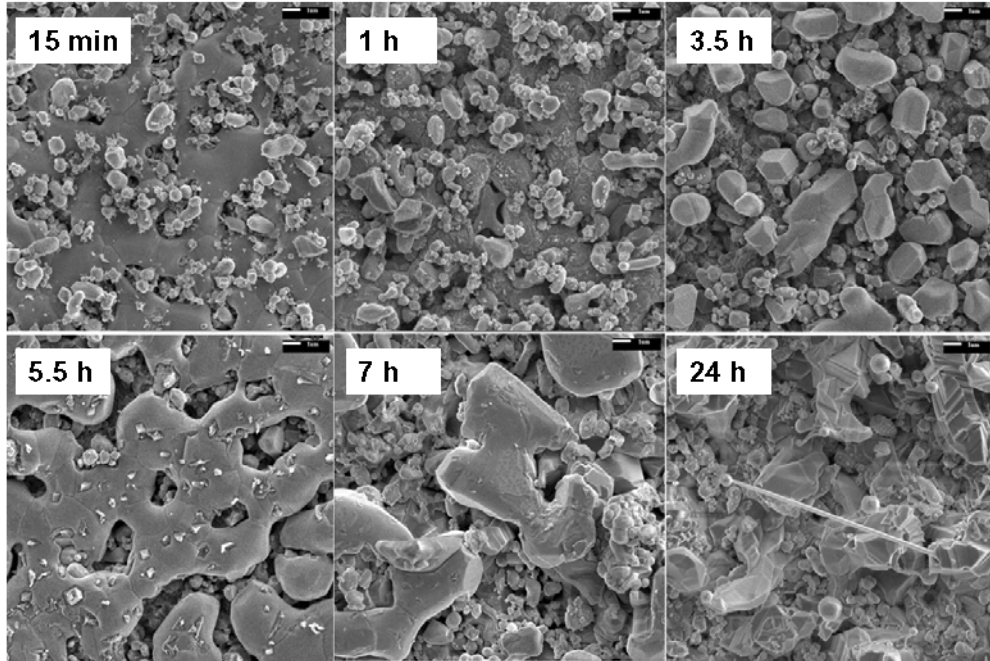


Figure 7-7 SEM plan view images of Ni/LaCrO₃ coatings heat-treated at 1100°C for various time periods; coalescence of particles and matrix morphology changes are seen for all images.

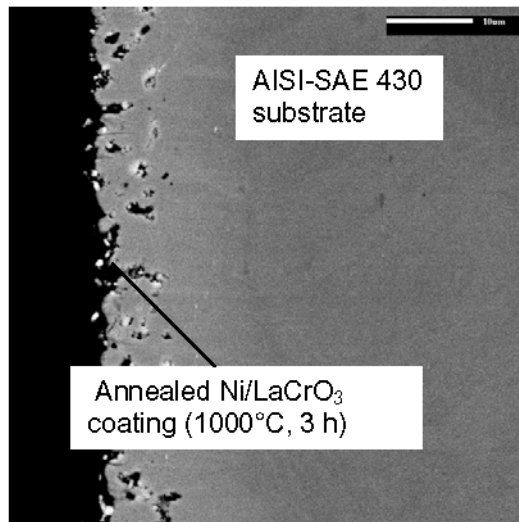


Figure 7-8 SEM cross section image of a Ni/LaCrO₃ coating heat-treated at 1000°C for 3 h; the porosity is clearly visible.

It was found that regardless of the conditions used, the morphology of the coating, including particle distribution and matrix alloy crystallite size and shape, changes

upon annealing. An extreme example is shown in Figure 7-7, which is an SEM plan view image of a Ni/LaCrO₃ coating heat-treated at 1100°C for 0.25, 1, 3.5, 5.5, 7 and 24 hours. As seen, particles have coalesced and the matrix morphology has changed after heat-treatment. Porosity is also seen in the cross sectional image shown in Figure 7-8.

The annealed coatings did not exhibit satisfactory oxidation behaviour. Breakaway oxidation behaviour and formation of hematite nodules were observed for annealed Ni/LaCrO₃ coatings. An example of an annealed/oxidized cross sectional image is shown in Figure 7-9. This sample was oxidized for 170 hours in air at 800°C. The poor oxidation resistance of the annealed samples was attributed to the presence of porosity and, more importantly, inadequate Cr content at the surface due to insufficient outward diffusion of Cr from the substrate to the coating layer.

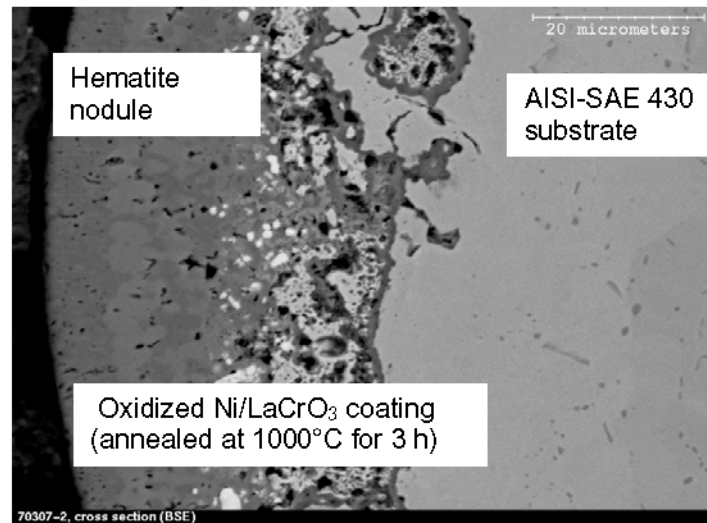


Figure 7-9 SEM cross section BSE image of the Ni/LaCrO₃ coating heat-treated at 1000°C for 3 h and oxidized in air at 800°C for 170 h. Breakaway oxidation is clearly observed.

Figure 7-10 shows EDX depth profiles for Ni, Fe and Cr from the surface to the substrate for a coated sample annealed at 1000°C for 3 hours. Data were collected by means of EDX point analysis. According to the data, the Cr concentration does

not exceed 8 wt.% even after 15 hours of annealing. The Cr concentration obtained by annealing is under the critical threshold (11 wt.%) which is required for formation of a protective chromia scale. Increasing the time and temperature does not significantly change the Cr concentration at the surface. As seen in Figure 7-11, even at 1100°C, after 3-4 hours the surface Cr concentration reaches a plateau and does not change considerably with annealing time.

Therefore, the annealing process to increase the Cr content of the coating and improve the oxidation behaviour was unsuccessful and no further experiments were performed.

The Ni/LaCrO₃ coated samples, which were not expected to exhibit good oxidation resistance, were tested for oxidation resistance at 800°C in air. Excellent results were achieved with the coatings without any pre-treatment. These results are discussed in Chapter 3 of this thesis. As mentioned previously, detailed discussion of unsuccessful results is beyond the scope of this section. In order for this thesis to be concise, only the results that exclusively fulfilled the objectives of this research are discussed in detail.

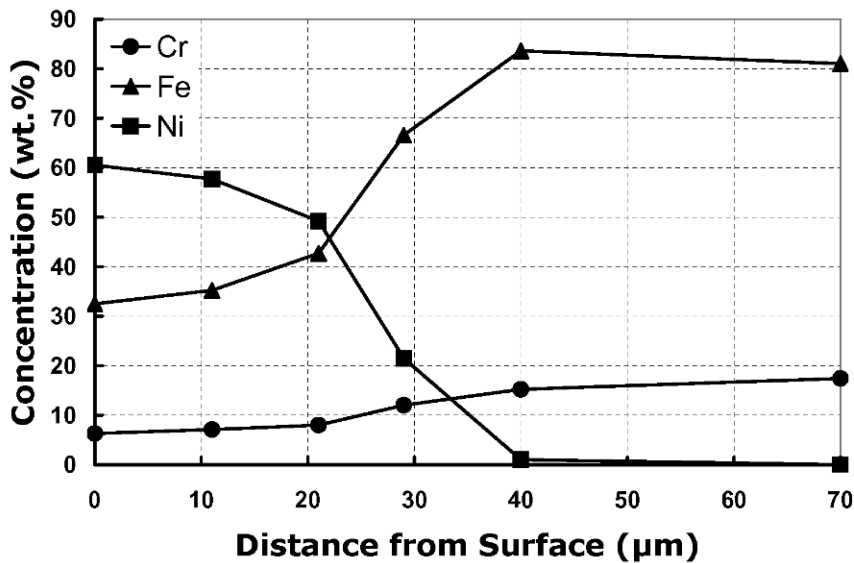


Figure 7-10 EDX depth profiles for Ni/LaCrO₃ coatings annealed at 1000°C for 3 hours.

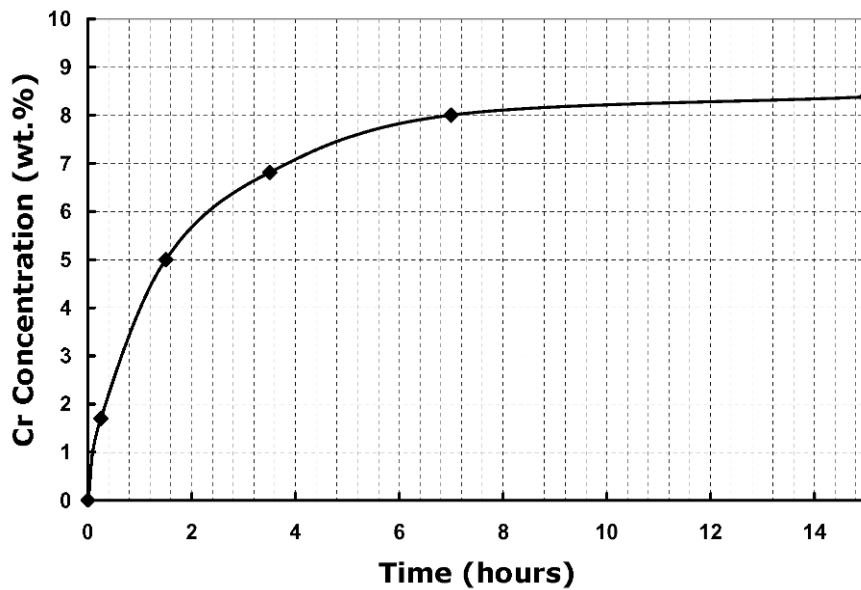


Figure 7-11 Surface Cr concentration versus annealing time for Ni/LaCrO₃ coatings annealed at 1100°C.

7.4 Conclusions

The following were concluded from the preliminary literature review and experiments:

1. Composite coatings consisting of conductive particles in an oxidation resistant matrix can provide a novel solution to metallic SOFC issues.
2. Rare earth perovskites are advantageous over other conductive ceramics (e.g., spinels) in terms of electronic conductivity, compositional stability and the presence of reactive elements which can improve the oxidation resistance of the composite matrix.
3. Composite coatings consisting of LaCrO₃ particles in a Ni matrix are practical provided a horizontal set-up is employed.
4. Pack aluminization, which necessarily uses halides, is not a suitable method of aluminization for the Ni/LaCrO₃ coatings because halides corrode LaCrO₃ particles.

5. Annealing in controlled, reducing atmospheres changes the morphology of the coating producing interconnected porosity.
6. Annealing in controlled, reducing atmospheres cannot increase the coating Cr content to the critical Cr concentration threshold.
7. Composite Ni/LaCrO₃ coatings do not require any pre-treatment to improve the oxidation resistance.
8. Overlay coatings were not tested due to the promising results achieved with the easy process of composite electrodeposition.

7.5 References

1. J. R. Nicholls and D. J. Stephenson, *Metals and Materials (Institute of Metals)*, **7**, 156 (1991)
2. B. M. Warnes, T. A. Legard, N. S. DuShane, J. E. Cockerill, and R. W. Beck, U.S. Pat. No. 6,136,451 (2000)
3. J. D. Reeves, B. K. Gupta, N. N. Das, U.S. Pat. No. 6,555,179 (2003)
4. C. Robert and Jr. Tucker, in ASM Handbook, Vol. 5, Surface engineering, Vacuum and Controlled-atmosphere Coating and surface Modification processes, ASM International (2003)
5. J. G. Smeggil, N. S. Bornstein and C. O. Brown, U.S. Pat. No. 4,451,299 (1984)
6. F. Schmitz and N. Czech, U.S. Pat. No. 5,993,980 (1999)
7. M. P. Bacos and P. Josso, U.S. Pat. No. 6,695,960 (2004)
8. P. Nash, M.F. Singleton, and J.L. Murray in ASM Handbook Vol. 3, Alloy Phase Diagram, ASM International (2002)
9. S. Mercier, F. Iozelli, M. P. Bacos and P. Josso, *Materials Science Forum*, **461-464**, 949 (2004)
10. J.R. Nicholls, N.J. Simms, W.Y. Chan and H.E. Evans, *Surface and Coatings Technology*, **149**, 236 (2002)
11. M. Mori, T. Yamamoto, H. Itoh and T. Watanabe, *Journal of Materials Science*, **32**, 2423 (1997)

12. J.H. Zhu, Y. Zhang, A. Basu, Z.G. Lu, M. Paranthaman, D.F. Lee and E.A. Payzant, *Surface and Coatings Technology*, **177**, 65 (2004)
13. J.D. Carter, C.C. Appel and M. Mogensen, *Journal of Solid State Chemistry*, **122**, 407 (1996)
14. T. Yamamoto, H. Itoh, M. Mori, N. Mori, T. Watanabe, N. Imanishi, Y. Takeda and O. Yamamoto, *Journal of Power Sources*, **61**, 219 (1996)
15. H. Nishiyama, M. Aizawa, N. Sakai, H. Yokokawa, T. Kawada and M. Dokiya, *Journal of Ceramic Society of Japan*, **109**, 527 (2001)
16. C.E. Hatchwell, N.M. Sammes, G.A. Tompsett and I.W.M. Brown, *Journal of European Ceramic Society*, **19**, 1697 (1999)